“NOVEL NANOSCOPIC MOLECULAR MATERIALS AS PRECURSORS FOR METAL AND SEMICONDUCTING NANOPARTICLES”

THESIS SUBMITTED TO THE SAVITRIBAI PHULE PUNE UNIVERSITY

FOR THE DEGREE OF
DOCTOR OF PHILOSOPHY
IN
CHEMISTRY

BY
BUSUPALLI BALANAGULU

UNDER THE GUIDANCE OF
DR. B. L. V. PRASAD

PHYSICAL AND MATERIALS CHEMISTRY DIVISION
CSIR-NATIONAL CHEMICAL LABORATORY
PUNE-411008

JANUARY 2016

This thesis is dedicated

to my Parents

Declaration

I hereby declare that the work described in the thesis entitled "**NOVEL NANOSCOPIC MOLECULAR MATERIALS AS PRECURSORS FOR METAL AND SEMICONDUCTING NANOPARTICLES**" submitted for the degree of Doctor of Philosophy in Chemistry to the Savitribai Phule Pune University, has been carried out by me at the Physical and Materials Chemistry Division of CSIR-National Chemical Laboratory, Pune under the supervision of Dr. B. L. V. Prasad. Such material as has been obtained by other sources has been duly acknowledged in this thesis. The work is original and has not been submitted in part or full by me for any other degree or diploma to other University.

Date:
Place: Pune

Busupalli Balanagulu
(Research Student)

Acknowledgments

The work presented in this thesis has been made possible by the association of many people and I would like to take this opportunity to acknowledge their contributions.

Firstly, I would like to express my deep and earnest gratitude to my research supervisor Dr. B. L. V. Prasad. I started my research career under his guidance and since then he has been a great support throughout. His ideas and timely suggestions have always helped me in my research. This thesis would not have been possible without his constant inspiration and guidance. His initiation and thoughtfulness has shaped this thesis. His patience during my thesis writing is greatly appreciated. I thank him whole heartedly for all his support.

I am indebted to Dr. K. Guruswamy for introducing me to the field of light scattering. The duration of interaction with him and his group has been an interesting phase of learning for me.

I would also like to thank Dr. Vijayamohanan Pillai, Director, CSIR-NCL and Dr. P. A. Joy, HOD Physical Chemistry Division, for allowing me to carry out research at this Institute and providing with the required facilities. I am thankful to CSIR, Govt. of India, for the research fellowship. I thank the previous director of CSIR-NCL Dr. Sourav Pal. I must also thank Prof. T. Pradeep for introducing me to the field of nanoscience and nanotechnology. I also thank Prof. G. U. Kulkarni for important and useful discussions.

Substantial amount of my work has been carried out in different laboratories both in CSIR- NCL and outside of it. I would take this opportunity to thank all my collaborators. I would like to thank Dr. Suwarna Datar Ms. Kalyani for allowing us to perform force microscopy experiments on our samples in her laboratory at DRDO-DIAT, Pune. I also would like to thank Dr. Manjusha V. Shelke and Mr. Rami Reddy for providing access to their cyclic voltammetry instrument. I am highly thankful to Prof. Santosh K. Haram and Mr. Shateesh Battu for allowing us to carry out major electrochemical experiments in his laboratory at S. P. P. Univeristy, Pune. I must thank Mr. Sreenivas Kummara and Dr. Chandrababu Naidu for their unrelenting help both in experiments and personal issues.

I would like to thank Dr. Anil Kumar, Dr. Satish Ogale, Dr. C. S. Gopinath, Dr. Rahul Banerjee, Dr. R. Nandini Devi, Dr. M. Jayakannan, Dr. Arup Kumar Rath, for their valuable suggestions and help during the course of my Ph.D. I also thank Dr. R. G. Gonnade for his help in performing some single crystal XRD experiments.

I express my gratitude towards my former and current lab-mates for their constant support and encouragement. I thank Dr. Vijay, Dr. Deepti, Dr. Manasi, Dr. Priyanka, Dr. Virginia D'Britto, Dr. Sheetal, Dr. Vilas, Dr. Ravi, Dr. Anal, Mr. Ajay, Dr. Nikunj, Dr. Prakash, Dr. Puspanjali. I must thank and with a heavy heart Mr. Agnimitra who was my batch-mate and an enthusiastic good friend. I thank K. S. Hima for collaborating with me for a project. I also thank my current lab-mates Jhumur, Poulomi, Pravin, Arun, Jayesh, Sachin, Abhijit, Prabhu, Aparna, Ruchira, Hari, Smitha, Anand, Vinitha.

My stay in CSIR-NCL and GJ Hostel has become vibrant and memorable because of my friends Chandrababu, Manoj, Suneel, Rami Reddy, Sridhar Reddy, Rajender Reddy, Ramesh, Sreenivasa Rao, Swaroop, Sudhakar, Vilas, Yadagiri, Sravani, Chaithanya, Laksmiprasad, Shateesh, Devadutta, Santhi, Innaiah, Narasimha Rao, Nagendra, Narendra, Srinivas, Hanuman, Narasimha Reddy, Santosh Reddy, Venubabu, Chaithanya Kiran, Bhogesh, Suresh, Srikanth Dama, Srikanth, Tharun, Ramu, Upender, Trinadh, Singh, Satish, Kumar, Praveen, Mangesh, Lenin, Ananth, Manjunath, Majid, Pratiksh, Kanak, Anjan, Pravat.

This thesis has become possible due to the strong faith in me and constant encouragement from my family. I thank my parents Busupalli Nageswara Reddy and Busupalli Krishnaveni from the bottom of my heart for their words of wisdom, trust, blessings and unfailing love. I could not have made it through without them being there for me at all times. I thank my brother Busupalli Rupesh Kumar Reddy.

Lastly, I thank everyone who has shared a smile with me sometime.

Busupalli Balanagulu

Pune, India

Uppu Kappurambu nokka polika nundu
Chooda chooda ruchula jaada veru

ఉప్పు కప్పురంబు నొక్క పోలిక నుండు
చూడచూడ రుచుల జాడ వేరు

Meaning: Salt and camphor look similar,

but, closer observation shows their taste is different.

This was the first poem I learned in Telugu and it introduced me to 'Taste Chemistry'.

Table of Contents

Chapter 1

Introduction

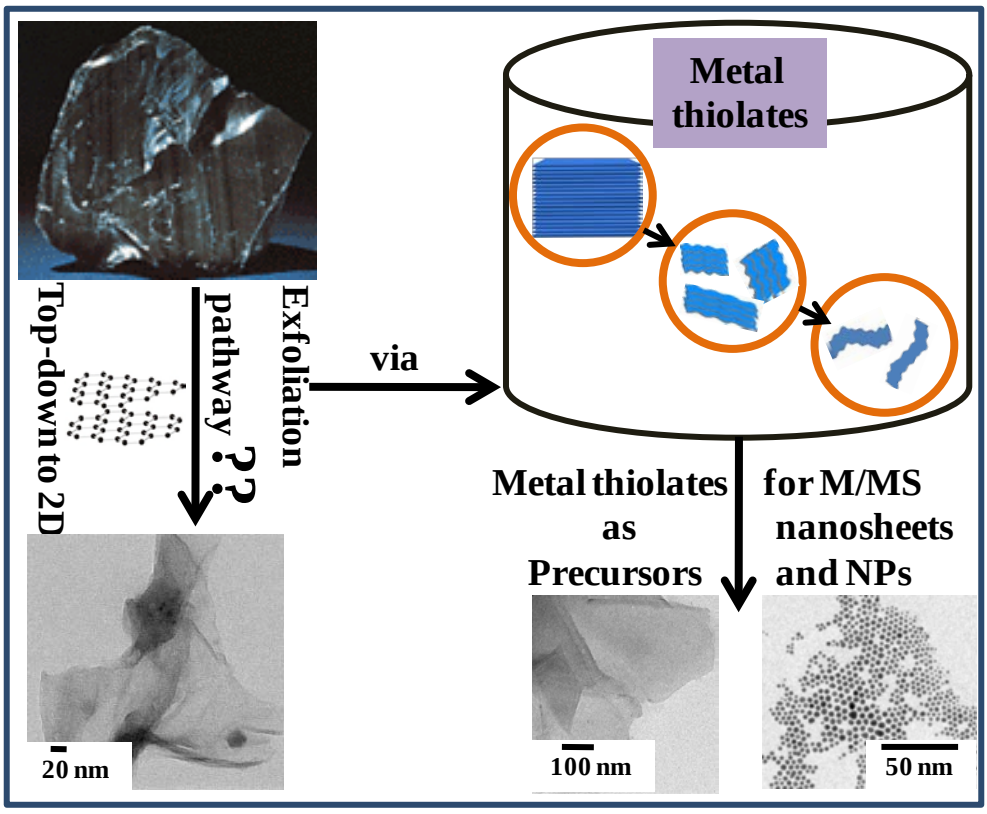

This chapter presents the background of the work carried out as part of this thesis, with a focus on layered nanomaterials, their synthetic protocols, properties and applications. This is followed by emphasizing the utility of metal thiolates as suitable candidates to study structural characteristics of the layered materials in solution and their usage as precursors to other nanoscale layered and spherical particles.

1.1 Introduction

It is well known that animals existed on earth much before human beings evolved. If we accept the old adage 'survival of the fittest' and if survival was solely based on physical strength, human beings probably would have become extinct by now. However, human beings today dominate the world and tamed the animals that are physically much stronger in comparison to them. This can be largely associated with the human beings' ingenuity and their ability to invent and utilize materials for various purposes. One can then say that materials are a direct consequence of the human being's ingenuity and urge for better living. Thus it can be said that the evolution of human beings is essentially linked to the development of materials or materials science.

1.1.1 Nanomaterials

While one of the urges of human beings is to develop materials with superior characteristics, another one is to miniaturize the devices without compromising their quality. In this context, the materials that are not visible to the human naked eye are assuming greater importance due to their promising properties that are important for research and applications. These materials normally have size range of about 10^{-9} m and are termed as nanomaterials. Nanomaterials aren't essentially new to the world but their identification specifically as a special class of materials began only very recently [1-4]. Quick developments occurred once it was realized that materials could be prepared controlling their size ranges to nanometer [5-12]. These developments included synthesis of various nanomaterials majorly through chemistry and through top down and related physical methods. Subsequent developments occurred in sophisticated synthetic procedures towards achieving nanomaterials tunable in several aspects such as size, shape etc. Nanochemistry along with other techniques such as CVD/PLD (Chemical Vapor Deposition/Pulsed Laser Deposition) [13], MBE (Molecular Beam Epitaxy) [14] etc. forms the basis for bottom up synthesis of nanomaterials enabling a control over the shape, size and orientation of the resulting nanomaterials which in turn influence their properties [15-20]. On the other hand, top-down preparation of nanomaterials occurs through various physical methods such as ball milling and lithographical etching etc.

Nanomaterials with different shapes such as spherical, triangular, cubical, hexagonal nanoparticles etc. are reported in literature. Similarly nanomaterials could be synthesized in different sizes ranging from sub nanometer spherical nanoparticles otherwise called as quantum clusters to nanomaterials that span over micrometer range in one or two dimensions such as nanorods and nanosheets. In Figure 1.1, a comparative scale of things in materials that are both natural and man-made is shown [21].

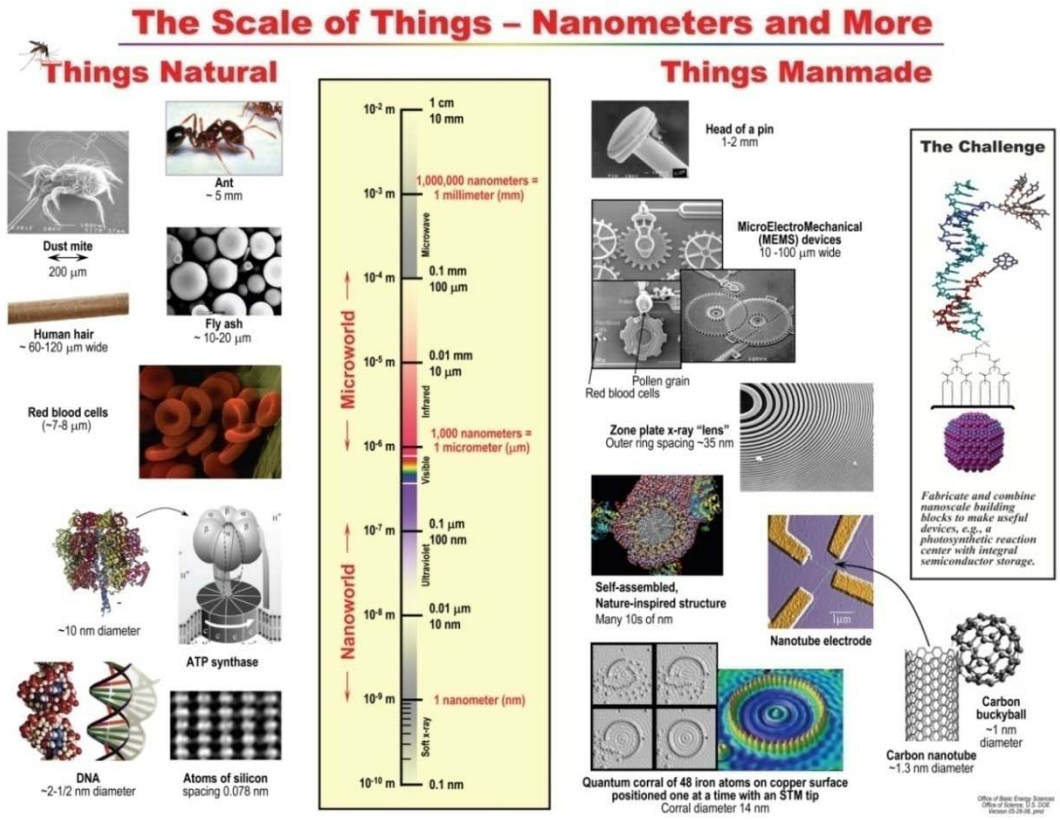

Figure 1.1: *The scale of the things, illustrating both natural and man-made materials [taken from ref. 21].*

In essence, it is quite amazing to realize that the assembly of a group of atoms/molecules at nanoscale could constitute a whole new field of science and the interest in them is ever growing as these exhibit unconventional properties [22, 23].

1.1.2 Synthetic methods for nanomaterials

The synthetic methods for preparing a variety of nanomaterials can be classified to two groups. One is bottom up synthesis and the other one is top-down synthesis. In bottom up

synthesis, monomolecular species are brought together through chemical reactions and these form self assembled structures such as in the case of supramolecular polymers, self assembled monolayers etc. [24]. In another example, nanoparticles are synthesized by surfactant stabilized assembly of metal atoms/metal ions via a reducing agent [25, 26]. In the case of top-down synthesis of nanomaterials, microfabrication techniques such as ball milling and lithography are used to etch out the bulk materials to result in nanometer sized materials [27]. Figure 1.2 shows a simple schematic representation of these two methods of synthesis.

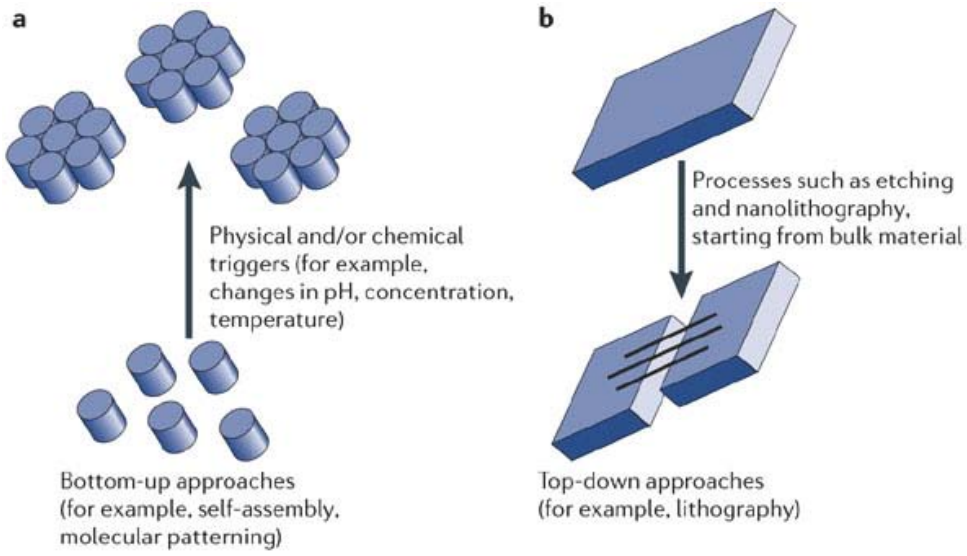

Figure 1.2: *Schematic representation of bottom up and top-down approaches for nanomaterial synthesis [taken from ref. 28].*

These two methods have both advantages and disadvantages. Table 1.3 below shows the differences between these two methods. Based on the described properties and applications of the resulting nanomaterials, one of the two different synthetic approaches is employed to synthesize a variety of nanomaterials. Especially for chemists, bottom up approach has garnered reverence because of the ability to control and tailor the as prepared nanomaterials' shapes, sizes, dimensionalities and thus the resulting properties. A chemist always tries to harness the existing vast library of chemicals to prepare novel chemical compounds or invent new chemistries towards realizing chemical compounds with enhanced activities. Combinatorial chemistry is the best example to consider in this

backdrop [29, 30]. With chemical ingenuity researchers can just alter the already existing materials to result in materials with superior properties.

Method	**Advantages**	**Disadvantages**
Bottom up synthesis Ex: Self assembly Vapor phase/liquid phase deposition techniques like CVD, MBE, sol-gel, precipitation, laser ablation, sonochemical, microwave, electodeposition etc.	• Precision control over the synthesized nanomaterials • Minimum energy loss • Cost effective • Good reproducibility • High purity products • Could produce composite materials and alloys easily • Rigorous stoichiometry control and better dispersions possible	• Defects are common in the as synthesized materials • Complex chemistry • Optimization of many parameters • Low wear resistance • Side products (undesired) • Non-homogenous distribution
Top-down Approach Ex: Lithography, Etching, Milling, Electrospinning etc.	• Better for fabricating microelectronic systems • And for micromechanical gears etc. • Thin films are usually prepared via this approach • Avoidance of undesirable products • Micron level devices and nanomaterials	• Highly costly equipment required • High energy costs • Contamination problems in the case of ball milling etc • Low surface area and highly polydisperse nanomaterials • Partially amorphous powders compared to the bottom up approach

Table 1.3: *Tabular representation of advantages and disadvantages of the bottom up and top-down synthetic methods for preparing nanomaterials.*

If we look at, for example, the carbon nanostructures, the first carbon structures discovered were fullerenes which exist in shapes like bucky balls [31, 32]. Then the preparation of carbon nanotubes followed [33]. Afterwards the discovery of graphene happened which is nothing but unrolling a single walled carbon nanotube to get a single sheet of connected carbon atoms [34, 35]. Though the actual discovery was attributed to pulling apart a single carbon layer from a graphitic stack of layers, several synthetic methods including chemical synthesis of graphene and alike materials ensued afterwards for preparing them in large scales [36-38]. Investigations of this lineage of carbon nanomaterials however enhanced the scientific understanding related to even other nanomaterials that exist in different dimensions, like 0D, 1D, 2D and also 3D materials [39, 40].

1.2 Dimensionality in nanomaterials

Apart from the shape and size variation, dimensionality of the prepared nanomaterials also influences their properties very well [41]. For instance, zero dimensional spherical nanoparticles have their carriers confined in all the three dimensions giving rise to materials called as quantum dots. Likewise, quantum wires are defined by the confinement of carriers in two dimensions thus restricting free movement of the carriers to only one dimension. Two dimensional nanosheets are the other type of nanomaterials where carriers are free to move in two dimensions but are confined only in one dimension. For instance, a flat sheet is a two dimensional material with carriers freely moving in the x- and y- directions but restricted to move along the z- direction. Even three dimensional nanomaterials such as frameworks derived from systems like polyoxometalates [42], metal organic frameworks (MOFs) [43] and other mesoporous materials such as zeolites also exist where carriers are free to move in all the three dimensions. Figure 1.4 depicted below clearly portrays the nanomaterials in different dimensions. In all these systems, it is the dimension–dependent confinement of carriers that plays a pivotal role in determining the properties that are often exotic and unprecedented.

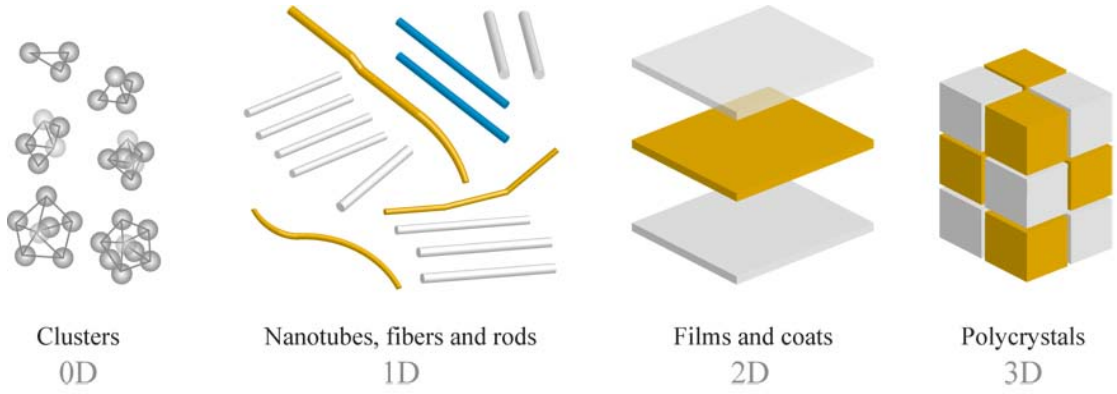

Figure 1.4: *Dimensionality in nanomaterials [taken from ref. 43].*

1.2.1 Materials in two dimensions

The discovery of graphene excited researchers, especially physicists heavily, since it was believed that such thin flat sheets were thermodynamically unstable to exist without support [44-46]. Graphene is a flat two dimensional material just consisting carbon atoms that are in SP^2 hybridization with some free electrons to move around. Experimental observation of a single layer of carbons through electron microscopy has convinced researchers of the possibility of obtaining a single sheet of a material. This was followed up by several other breakthroughs based on graphene's unprecedented properties. Of late, graphene liquid cells are also used to contain the nanomaterials and even single DNA and protein molecules for electron microscopic imaging [47-49]. While the grapheme discovery and its exciting properties are being researched intensely, there is also a sudden surge in the area of metal atom containing layered materials such as MoS_2 etc., due to their irreplaceable importance in energy conversion and storage phenomena. Also imminent was the possibility of stacking several such layers to realize heterostructures which could possess abnormal behaviors such as superconductivity and unconventional magnetism [50]. This has now lead researchers to delve into such layered materials with enhanced vigor. Enormous efforts had been devoted towards synthesis and characterization and utilization of several such layered materials. Also, reports exist on the formation and applications of heterostructures made of different single layers stacked together in 2D. Layered crystals can be obtained as nanosheets because of the strong in-plane bonding and absence of such strong bonding out-of-plane in these crystals. In-plane

bonding, in these materials usually consists of strong covalent or coordinate covalent bonds. Out of plane bonding comprises of weak van der Waals forces of interaction between the stacked layers. These bonding characteristics facilitate the exfoliation of these layered crystals into nanosheets and these nanosheets display unprecedented properties. One more important result of accessing such 2D nanosheets is that these nanosheets exhibit modified band structure which results in more propound electronic and magnetic properties. Researchers fondly call these exfoliated layered materials as LEGO bricks since these could form layered heterostructures if alternating stacks of different layers could be made which have enormous implications in several fields (Figure 1.5) [51-53].

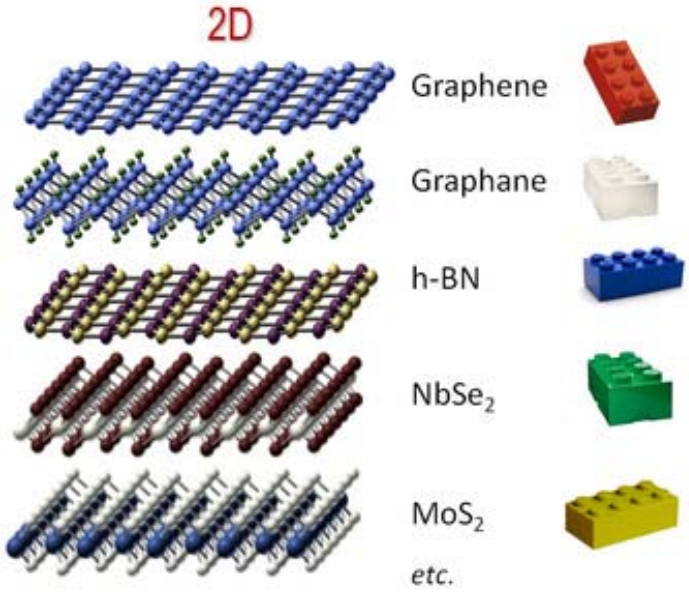

Figure 1.5: *Pictorial depiction of a variety of 2D materials and the possibility of preparing heterostructures from them. While preparing heterostructures, these are often referred to as LEGO bricks [Courtesy of Dr. Casiraghi webpage].*

1.2.2 Why are 2D materials important?

What makes the 2D materials important? As discussed in previous sections, confinement of charge carriers to just two dimensions makes these 2D materials attractive for several applications and also to study several interesting physical phenomena. Majorly, optical and electronic properties of a material get altered significantly once the material is

converted from 3-dimensional to 2-dimensional [54]. The change in properties observed in these 2D materials can be attributed to absence of interlayer interactions when these are in single layered form, along with the confinement of electrons. This absence of interlayer interactions or restricted interlayer interactions in 2D materials also influences their band structure and thus their properties. There exists rich physics in these 2D materials, for example, in graphene. Applications in semiconductor heterostructures [55-57], quantum Hall/fractional quantum Hall effect [58, 59], high temperature superconductivity, quantum mechanical tunneling are a few physics related phenomena connected to the 2D materials [57, 60-63]. Chemical modification of several 2D materials can lead to diversified applications such as in sensing, catalysis, magnetism etc. [64, 65]. Apart from all these outstanding achievements these 2D layered crystals also form composite materials with polymers even biopolymers [66-68]. The possible list of applications of such 2D materials is wide ranging which include even packaging and lubricating 2D materials. Recent advances even show water purification and desalination. Some of these 2D layered materials are even employed as model candidates to study exotic and fundamental phenomena also.

1.2.3 Various methods for preparing 2D materials

The interest in the area of 2D materials got invigorated when two physicists succeeded in obtaining graphene via manually/mechanically cleaving graphite using a scotch tape [69]. Though as of today it is the only method that results in high quality graphene crystal, it could not be used for producing large quantities of graphene. And, as the rediscovery of metal ion containing layered materials such as MoS_2 followed afterwards, various methods to prepare these layered materials were established. Several such preparatory methods exist in the literature for realizing a variety of 2D materials such as graphene, MoS_2, WS_2, TiS_2, TaS_2, $MoSe_2$ etc. [70-73]. Some of the most used methods of these are 1) solvent exfoliation techniques [74-78], 2) ultrasonication [79] and 3) ion intercalation [70, 80-83]. One of the most widely performed exfoliation method is the small cation (Li-ion) intercalated exfoliation [84-86]. Researchers had already attempted and succeeded in exfoliating layered compounds by using methods such as insertion of tiny cations into the crystal lattice of the stacked two dimensional sheets so as to de-stack them, for example,

in the case of MoS_2 and this experiment could yield single layers of two dimensional sheets out of a stack of sheets. Figure 1.6 displays a cartoon representation of the liquid exfoliation/ultrasonication and ion intercalation exfoliation methods.

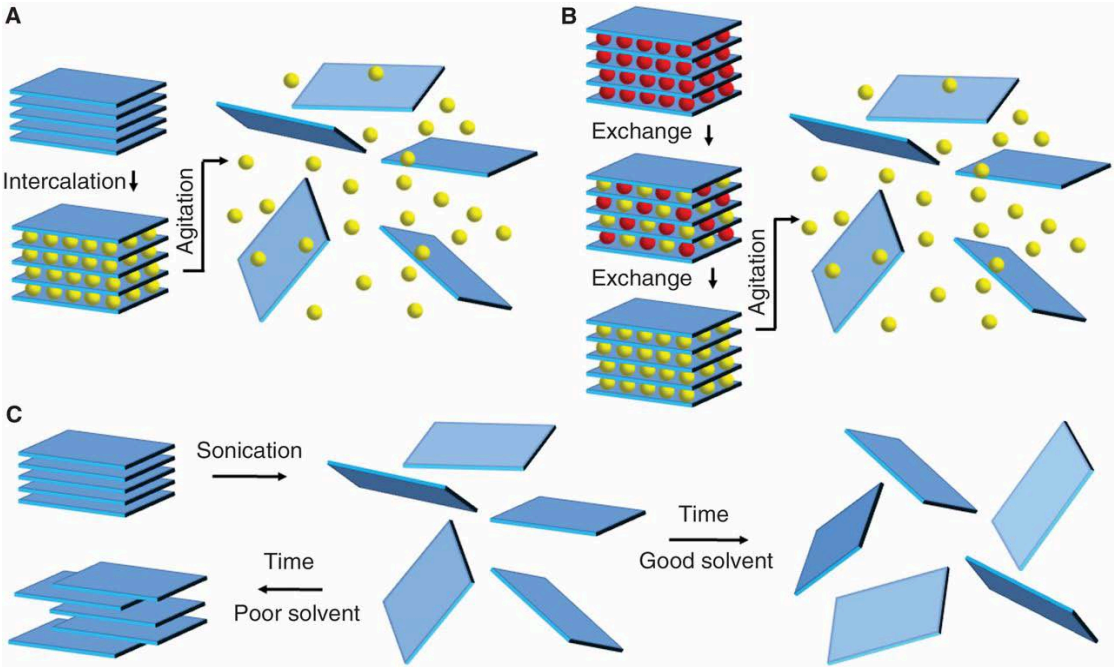

Figure 1.6: *Exfoliation methods for preparing 2D materials from the stacked sheets of these materials. A). Simple ion intercalation like Li-ion intercalation. B). Agitation followed by intercalation. C). Simple sonication [taken from ref. 75].*

Figure 1.7 shows solvent dispersions of the as prepared layered compounds like MoS_2. Reports say that these layered compounds form suspensions only in microgram/milligram scale quantities with select solvents. This posts serious drawbacks to utilization of such materials that could be obtained only in very small amounts.

Figure 1.7: *Liquid dispersion of a few example 2D layered compounds in solvents such as DMF [adapted from ref. 75].*

On more probable candidate in this layered materials category is what the researchers called a 'molecular paper' (Figure 1.8) [87, 88]. Recent studies have shown a bottom up approach for preparing the molecular papers called as peptoid nanosheets. Peptoids are brought together and self assembled from bottom up utilizing the monomolecular species. These as formed peptoid nanosheets were observed to be freely floating in solvent via confocal liquid phase microscopy. But these peptoids are devoid of any metal ion and thus cannot be used in important semiconductor applications.

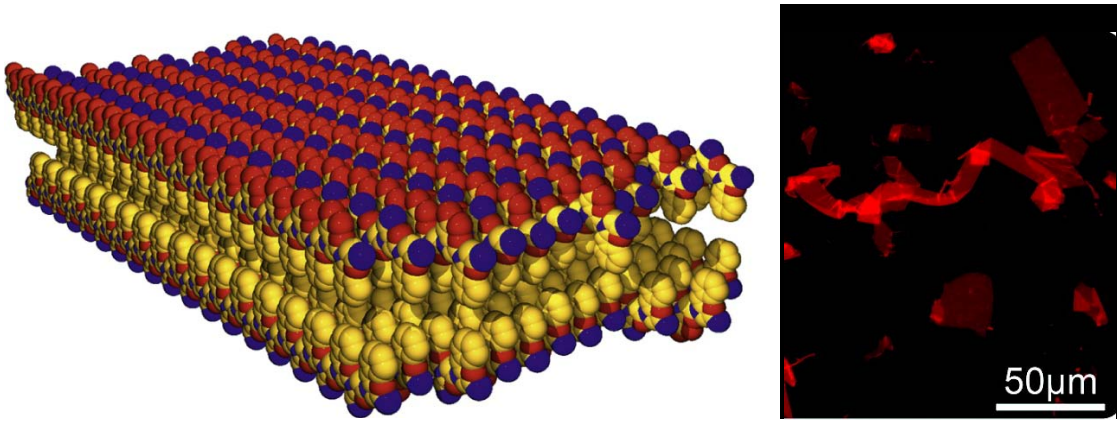

Figure 1.8: *Peptoid nanosheet. Also called as molecular paper by the authors (evident from the confocal liquid microscopy showing floating peptoid nanosheets) [adapted from ref. 87 & 88].*

Though many methods are widely used to prepare various 2D layered materials, access to huge quantities so as to utilize them in ever growing industrial needs remain a challenging task. This has led researchers to look into new pastures of research. One significant application of such 2D materials that can be thought of is developing molecular inks which can be coated on to substrates. Very recently organic inks based on all-organic layered materials that could be coated on substrates had been demonstrated [89]. Establishing such inks with inorganic metal containing compounds could have enormous scope in the backdrop of major challenges that the humankind face such as cost reduction in clean energy etc. There is thus an urge to device much more efficient methods or to discover novel classes of metal containing 2D materials that could be prepared easily in huge amounts like in gram scales. The best method that could be looked up to is the precursor based method. Again, for MoS_2 etc., precursors such as ammonium molybdate exist but again these need to be subjected to rigorous chemical synthetic protocols to finally result in 2D materials of interest and the yields of the final material is still a concern. Accessing huge amounts of materials that exist as 2D materials thus attracted us and we started searching literature for such metal containing layered materials.

1.3 Metal thiolates as a class of 2D materials

Metal thiolates are coordination compounds that could be prepared very easily [90-98]. Metal thiolates exist as lamellae or stacked sheets in the solid state. Metal thiolates can be divided majorly into two types based on the oxidation state of the coordinating metal ion in the thiolate. One type has the metal ion in the +1 oxidation state such as in silver thiolates and copper (I) thiolates. Another type comprises of examples like palladium thiolates and nickel thiolates in which the metal ion exists in +2 oxidation state. The remarkable difference between these thiolates arises from their solubility characteristics. The ones in which the metal ion is in +1 oxidation state are insoluble in any solvent whereas the metal thiolates having metal in +2 oxidation state are highly soluble in apolar organic solvents such as toluene and chloroform. This stunning difference in the solubility can be explained through bonding differences in these. Based on the literature reports on several metal thiolates such as silver thiolates and copper thiolates and

palladium thiolates etc., the bonding characteristics of these metal thiolates could be inferred as described here.

In these thiolates, there exists polar covalent bonding between the metal and the sulfur. For example, in silver thiolates, silver is bonded to sulfur through a polar covalent bond and this is same for the palladium thiolates albeit in $Pd(SR)_2$ stoichiometry. Now, in silver thiolates the character of polarity in the covalent bond is more prominent compared to the palladium system mainly due to the electronegativity differences between silver and palladium arising due to the different oxidation states that they exist in. The less polar covalent character of palladium thiolates may be contributing to the hydrophobicity of the compounds overall thereby rendering them soluble in non-polar organic solvents. But in the case of the silver thiolates, as the covalent bonding is more polar the contribution from the bonding to the hydrophobic nature of the silver thiolates is diminished. This plausibility leads to their insolubility in non-polar organic solvents at room temperature. But there are reports claiming that silver thiolates are soluble in boiling toluene which after cooling to the room temperature returns to its insoluble state very quickly [99]. This is not the case with the other (II) oxidation state containing metal thiolates such as palladium thiolates, nickel thiolates, lead thiolates and mercury thiolates. Certain as prepared metal thiolates such as palladium thiolates readily form solutions with organic non-polar solvents such as toluene and hexane and chloroform etc. Also these could be prepared in gram scale (or may be in kilogram scale quantities for industrial processing).

Though information about this class of materials (palladium thiolates) existed from as early as 1935 [90], attempts to recognize the importance of these materials have been sparse. In this 1935 report the authors had shown that these metal thiolates are inorganic complexes containing both metal ions and the ligands and that some of these metal thiolates readily get dissolved in non-polar organic solvents. After this, these materials have not been the focus of any major research activity. Their importance was recognized only recently when in 2001, in a report from G. U. Kulkarni et al. reported thermal studies on the as prepared palladium thiolates [91]. In that study the authors reported the preparation of palladium thiolates employing a series of alkanethiols as ligands and showed solid state structural transformation in them by performing thermal experiments.

Their further studies included utilizing these metal thiolates in electronics technology by coating them onto substrates and etching them to result in metal resists that are useful in semiconductor industries. G. U. Kulkarni et al., had substantially contributed to the palladium thiolates research that included detailed synthetic pathways for preparing palladium monothiolates such as PdC_{12} thiolate and PdC_{16} thiolate etc., and also they had harnessed the solubility characteristic of the thiol ligands in organic solvents to realize mixed thiolates with palladium [92]. Figure 1.9 shows STM (Scanning Tunneling Microscopy) of such mono and mixed thiolates of palladium. The Figure 1.9a clearly shows the bilayer structure that is known to be present in solid state palladium thiolates. Similarly in Figure 1.9b also it is evident that the mixed palladium thiolate is present in bilayer form and the identification of even different alkyl chains that impart different lengths in the mixed thiolate is evident from the STM microscopy.

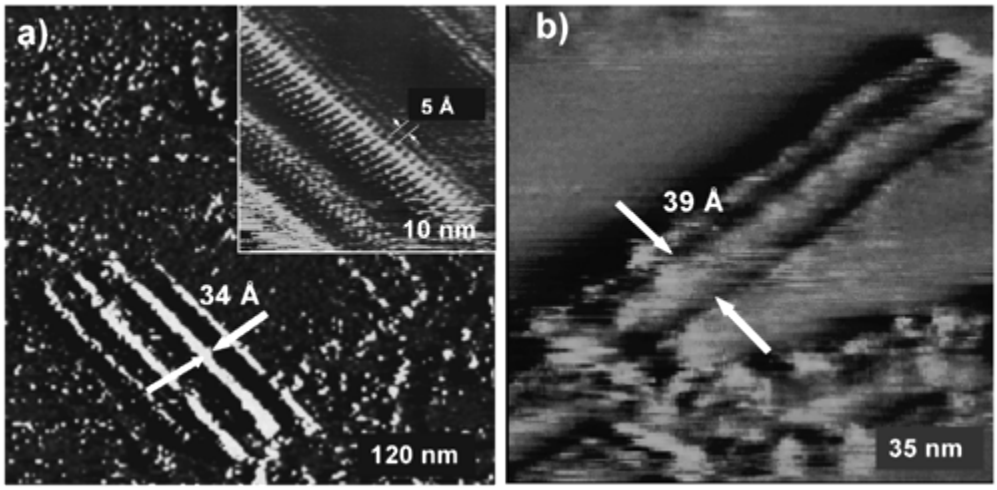

Figure 1.9: *STM image of the palladium thiolates. a) PdC_{12} thiolate, b) PdC_{12}-PdC_{16} (50:50) mixed thiolate [taken from ref. 92].*

These authors then utilized these palladium thiolates for inkjet printing which is made possible due to their solubility in certain solvents and also as electron resists due to the rich alkyl chains present in these thiolates. These electron resists were obtained as patterned palladium structures via direct-write electron beam lithography methods (Figure 1.10). This shows potential applications of such thiolates in electronics industry [100-102].

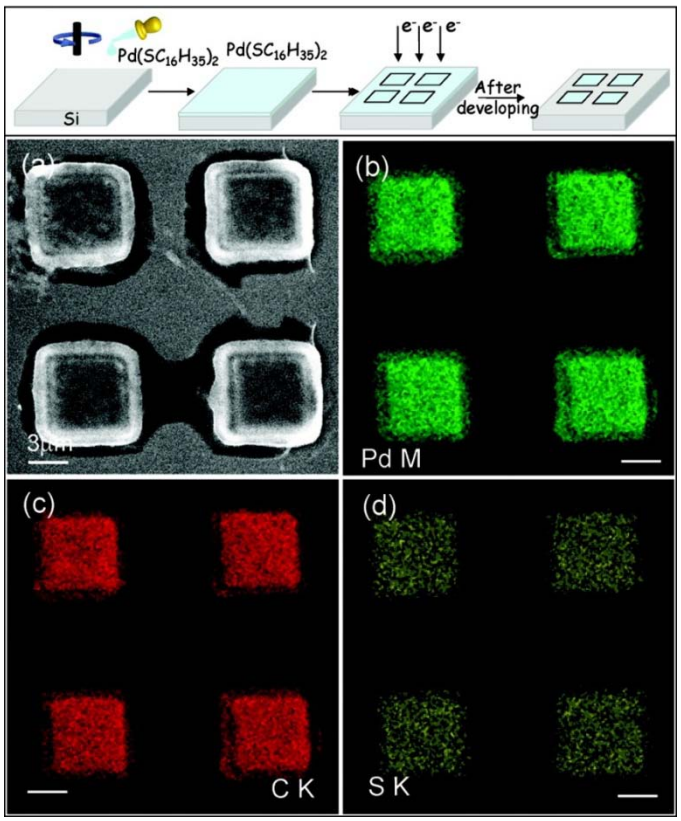

Figure 1.10: *Direct-write electron beam lithography of palladium hexanethiolate (PdC_{16} thiolate). Top portion shows the procedure employed by G. U. Kulkarni et al., to prepare patterned palladium structures through direct-write electron beam lithography. The steps involved in the procedure can be detailed as; step 1) spin-coating of the PdC_{16} thiolate on a Si (111) surface, step 2) electron beam lithographic patterning of the thiolate at 5 kV, step 3) developing the patterned surface in toluene for 10 sec. a) SEM image of the patterned material. (b-d) EDS patterns for the elements: b) Pd M, c) C K, d) S K lines [taken from ref. 101].*

Since these palladium thiolates readily form solutions with organic solvents such as toluene, one quick question that would come to mind is what is happening to the stacked lamellae of the solid state structures when they go into an organic solvent. One prospect is that they decompose into individual $Pd(SR)_2$ molecules and form a true solution. The other possibility is that upon adding a solvent the individual sheets of lamellae simply delaminate and these sheets keep floating in the solvent forming a dispersion (Figure 1.11). However, since the sheet is molecularly thin, such a dispersion would also look

like a solution. This possibility of second pathway and the ensuing existence of floating molecular sheets in solution excited us and therefore we wanted to probe the solution state structure of these thiolates in a systematic way. Since we could synthesize these palladium thiolates in gram scale quantities with ease, we resorted to follow their solubilization by studying their solution characteristics. Such studies, we thought, could shed a light on structural features of such layered materials in solution and could be generalized for other such materials. Though MoS_2 like 2D materials are known to exist as single layers in dispersions with certain solvents like DMF, their exfoliation pathway is not known even today. The detailed structural understanding or the mechanism of the exfoliation of two dimensional layered nanosheets in solution is difficult mostly because of 1) the interferences arising from the insertion of small cations such as lithium, sodium or ammonium cations cause lattice defects in the as exfoliated two dimensional crystals, 2) small amounts of these materials only could be obtained as single layers in solvents via dispersing them in such solvents and 3) the shelf life of these individual nanosheets in dispersed state in solvents is not very long. In this backdrop, we envisaged that metal thiolates could become good model candidates for such studies.

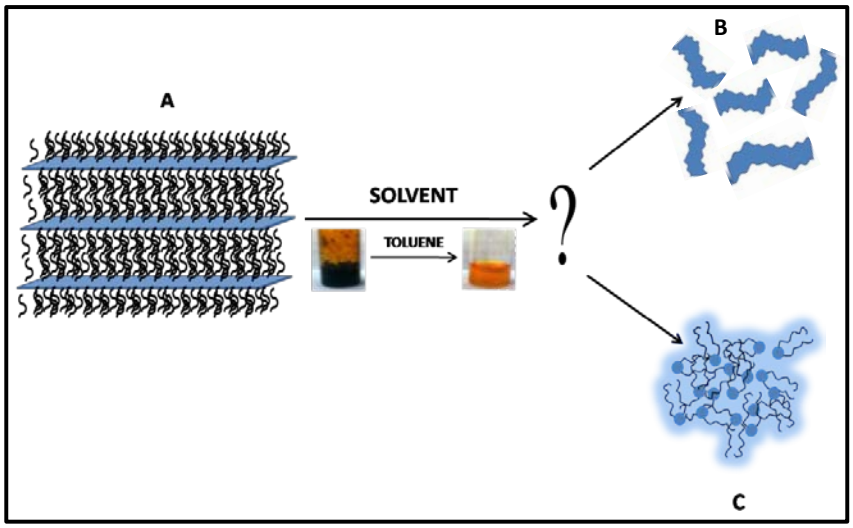

Figure 1.11: *Cartoon representation of the two different situations that can be expected from the dissolution of palladium thiolate in an organic solvent. A) Palladium thiolate in stacked lamellar form in its solid state. B) Palladium thiolate existing as freely floating nanosheets. C) Palladium thiolate (a molecular material) disintegrated into its molecular moieties.*

These metal thiolates could also be used as precursors for successor metal/metal sulfide nanosheets and nanoparticles materials (Figure 1.12) [103-120]. Thus we embarked on a detailed study of these thiolates as part of this thesis work which presents, 1) synthesis of these metal thiolates, 2) solution structural study of these metal thiolates, 3) preparation of metal/metal sulfide sheets from these precursor metal thiolates, 4) exploring the properties of the metal/metal sulfide sheets, 5) utilization of these metal thiolates as precursors for metal/metal sulfide nanoparticles and 6) also their heterostructures.

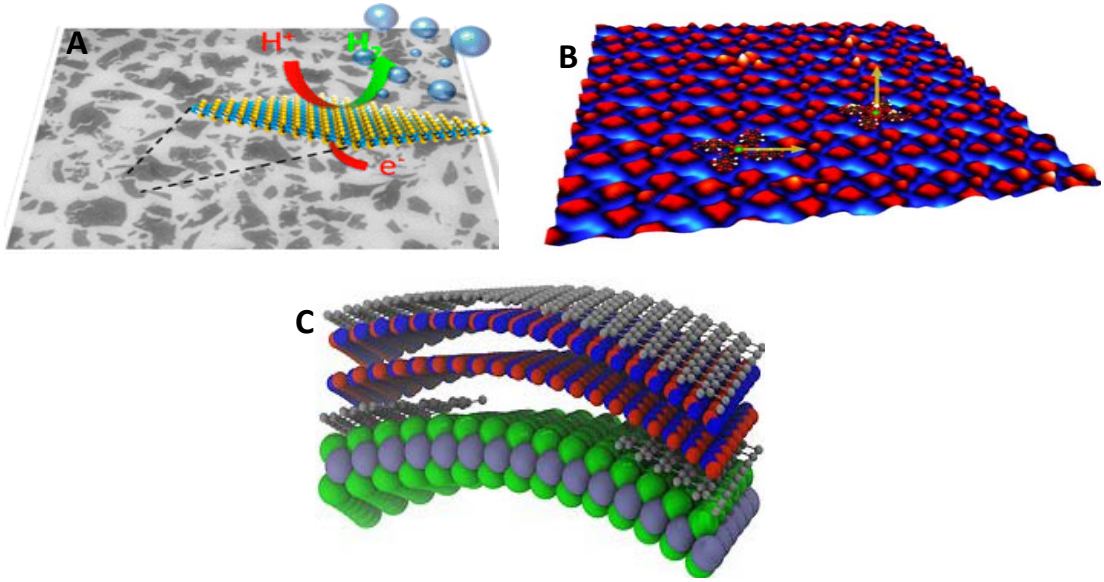

Figure 1.12: *Cartoon representations of different properties and applications of several 2D materials (relevant to the work done in this thesis).* ***A.*** *Hydrogen evolution reaction on MoS_2 nanosheets (adapted from ref. 78).* ***B.*** *Scanning Tunneling Microscope image of a 2D material self-assembled on copper surface exhibiting magnetism, the arrows indicate the preferred magnetization direction of individual iron atoms (Courtesy of Prof. Gambardella's webpage).* ***C.*** *Schematic showing of heterostructures formation from different 2D layered materials via stacking (Image credit: Argonne national Laboratory).*

Figure 1.12 gives a glimpse of the various applications of 2D materials with industrial realization of the benefits that could be reaped from these several nanosheets by cross-linking them.

1.4 Objective of this thesis

The work embedded in this thesis establishes the easy accessibility to gram scale quantities of 'soluble' metal thiolates and proves that they exist as 2D sheets in solvents. It also demonstrates the possibility of utilizing these metal thiolates for preparing metallic and semiconducting nanoscale materials such as metal and metal sulfide nanosheets and metallic or semiconductor nanoparticles and their heterostructures.

1.5 Outline of the thesis

Brief background for the work carried out in the thesis has been described in the above sections.

Chapter 2: The chapter describes the synthetic procedures for preparing metal thiolates and the solution structural studies on these thiolates. Several metal thiolates viz. palladium thiolates, nickel thiolates, mercury thiolates and lead thiolates were synthesized using a very simple solvent-less instantaneous reaction. These thiolates were found to be readily soluble in apolar organic solvents such as chloroform and toluene. A thorough solution structural characterization of these thiolates was carried out employing light and x-ray scattering techniques along with solution state FTIR which provided evidence for the exfoliation of single sheets of the metal thiolates from the pre-existing lamellar stacks of these thiolates. The scattering data were assisted by the microscopic visualization through electron microscopy. Solubility of these thiolates makes them as candid precursors for their descendent materials with novel properties.

Chapter 3: This chapter is divided into two parts.

Part I: The part I is dedicated to the description of the synthetic procedures for the synthesis of the metal and semiconducting nanosheets from their precursor metal thiolate molecular sheets. This was done through simple heating techniques. More specifically, the metal thiolate solution was first spin coated onto the suitable substrates such as quartz. These as coated quartz plates were then heated to high temperatures in tube furnaces under appropriate atmospheres like argon gas atmosphere etc. This resulted in the metallic or semiconducting metal sulfide nanosheets confirmed and thoroughly characterized by several instrumental techniques, primarily with those such as powder

XRD, electron microscopy. Some of these as prepared nanosheets viz. nickel/nickel sulfides exhibited unprecedented properties like room temperature ferromagnetism. Thorough understanding of the ferromagnetism in these nanosheets was carried out by SQUID analysis, atomic/magnetic force microscopy.

Part II: Part II of this chapter deals with an important application, hydrogen production in the nickel sulfide nanosheets. Hydrogen evolution from cheaper catalytic sources such as nickel based electro/photo catalysts assumes importance in the backdrop of ever growing energy needs of the world. The nickel/nickel sulfide nanosheets we prepared displayed efficient electrocatalytic hydrogen evolution activity. The hydrogen evolution reaction over-potentials for the nickel/nickel sulfide nanosheets were found to be comparable with the latest results on the highly studied molybdenum disulfide nanosheets.

Chapter 4: The chapter presents results arising from the reduction of the as prepared metal thiolate nanosheets into their derivative nanoparticles using a solid state route. Lead sulfide and cadmium sulfide model systems derived from lead octanethiolate and cadmium octanethiolate respectively were studied thoroughly with the help of basic and advanced instrumental techniques such as UV-visible, FTIR, fluorescence, XRD and electron microscopy. The chapter concludes with demonstrating the possibility of extending this solid state route of synthesis of metal or semiconductor nanoparticles by employing a simple 'grinding the precursor compound with sodium sulfide' to yield the respective metal or semiconducting nanoparticles. This was extended to make metal nanoparticles from insoluble metal thiolates such as gold thiolates, silver thiolates and copper thiolates. Also nanosheet–nanoparticle heterostructures were made possible by simple mixing of the colloidal nanoparticle solution with any metal thiolate solution such as a palladium thiolate in toluene and palladium nanoparticles in *tert*–butyl toluene that resulted in metallic palladium nanoparticles decorating the palladium thiolate sheets. This was extended to the other nanosheet–nanoparticle systems as well such as gold nanoparticles on palladium thiolate nanosheets.

Chapter 5: This chapter summarizes the salient features of the work done and provides a roadmap on the future prospects of the research related to the work presented in here.

1.6 References

[1]. A. P. Alivisatos. Semiconductor clusters, nanocrystals, and quantum dots. *Science,* **1996,** 271, 933.

[2]. C. J. Murphy and J. L. Coffer. Quantum dots: A primer. *Appl. Spectr.,* **2002,** 56, 16.

[3]. C. B. Murray, C. R. Kagan, and M. G. Bawendi. Synthesis and characterization of monodisperse nanocrystals and close-packed nanocrystal assemblies. *Annu. Rev. Mater. Sci.,* **2000,** 30, 545.

[4]. M. Brust, M. Walker, D. Bethell, D. J. Schiffrin, and R. Whyman. Synthesis of thiol-derivatized gold nanoparticles in a 2-phase liquid-liquid system. *J. Chem. Soc. Chem. Commun.,* **1994,** 7, 801.

[5]. K. V. Sarathy, G. U. Kulkarni, and C. N. R. Rao. A novel method of preparing thiol-derivatised nanoparticles of gold, platinum and silver forming superstructures. *Chem. Commun.,* **1997,** 6, 537.

[6]. L. Spanhel, M. Haase, H. Weller, and A. Henglein. Photochemistry of colloidal semiconductors.20. Surface modification and stability of strong luminescing CdS particles. *J. Am. Chem. Soc.,* **1987,** 109, 5649.

[7]. C. R. Martin. Nanomaterials - a membrane-based synthetic approach. *Science,* **1994,** 266, 1961.

[8]. J. H. Zhan, X. G. Yang, D. W. Wang, S. D. Li, Y. Xie, Y. Xia, and Y. Qian. Polymer-controlled growth of CdS nanowires. *Adv. Mater.,* **2000,** 12, 1348.

[9]. C. B. Mao, D. J. Solis, B. D. Reiss, S. T. Kottmann, R. Y. Sweeney, A. Hayhurst, G. Georgiou, B. Iverson, and A. M. Belcher. Virus-based toolkit for the directed synthesis of magnetic and semiconducting nanowires. *Science,* **2004,** 303, 213.

[10]. S. Mann, J. P. Hannington, and R. J. P. Williams. Phospholipid-vesicles as a model system for biomineralization. *Nature,* **1986,** 324, 565.

[11]. G. Schmid, M. Baumle, M. Geerkens, I. Helm, C. Osemann, and T. Sawitowski. Current and future applications of nanoclusters. *Chem. Soc. Rev.,* **1999,** 28, 179.

[12]. C. B. Murray, D. J. Norris, and M. G. Bawendi. Synthesis and characterization of nearly monodisperse CdE (E = S, Se, Te) semiconductor nanocrystallites. *J. Am. Chem. Soc.,* **1993,** 115, 8706.

[13]. Choy, K. L., Chemical vapour deposition of coatings. *Prog. Mater. Sci.* **2003,** 48, 57.

[14]. Vyatkin, A. F.; Farber, L. E.; Avilov, A. S.; Orekhov, S. N.; Parker, E. K. H. C., Structure of amorphous silicon layers deposited under ultrahigh vaccum at different substrate temperatures. In *Silicon Molecular Beam Epitaxy,* Elsevier: Oxford, **1989;** 357.

[15]. X. G. Peng, L. Manna,W. D. Yang, J.Wickham, E. Scher, A. Kadavanich, and A. P. Alivisatos. Shape control of CdSe nanocrystals. *Nature,* **2000,** 404, 6773.

[16]. S. M. Lee, S. N. Cho, and J. Cheon. Anisotropic shape control of colloidal inorganic nanocrystals. *Adv. Mater.,* **2003,** 15, 441.

[17]. C. J. Murphy and J. L. Coffer. Quantum dots: A primer. *Appl. Spectr.,* **2002,** 56, 16A.

[18]. N. Gaponik, D. V. Talapin, A. L. Rogach, K. Hoppe, E. V. Shevchenko, A. Kornowski, A. Eychmuller, and H. Weller. Thiol-capping of CdTe nanocrystals: An alternative to organometallic synthetic routes. *J. Phys. Chem. B,* **2002,** 106, 7177.

[19]. G. R. Patzke, F. Krumeich, and R. Nesper. Oxidic nanotubes and nanorods - anisotropic modules for a future nanotechnology. *Angew. Chem. Int. Ed.,* **2002,** 41, 2446.

[20]. C. J. Barrelet, Y. Wu, D. C. Bell, and C. M. Lieber. Synthesis of CdS and ZnS nanowires using single-source molecular precursors. *J. Am. Chem. Soc.,* **2003,** 125, 11498.

[21]. Bhushan, B., Handbook of Nanotechnology, volume 1 of Springer Handbook of Nanotechnology. *Springer-Verlag, Heidelberg,* **2004.**

[22]. Alivisatos, A. P.; Barbara, P. F.; Castleman, A. W.; Chang, J.; Dixon, D. A.; Klein, M. L.; McLendon, G. L.; Miller, J. S.; Ratner, M. A.; Rossky, P. J.; Stupp, S. I.; Thompson, M. E., From molecules to materials: current trends and future directions. *Adv. Mater.* **1998,** 10, 1297.

[23]. Whitesides, G.; Mathias, J.; Seto, C., Molecular self-assembly and nanochemistry: a chemical strategy for the synthesis of nanostructures. *Science* **1991,** 254, 1312.

[24]. Sakamoto, J.; Van Heijst, J.; Lukin, O.; Schluter, A. D., Two-dimensional polymers: just a dream of synthetic chemists? *Angew. Chem., Intl. Ed.* **2009,** 48, 1030.

[25]. Kasture, M.; Singh, S.; Patel, P.; Joy, P. A.; Prabhune, A. A.; Ramana, C. V.; Prasad, B. L. V., Multiutility sophorolipids as nanoparticle capping agents: synthesis of stable and water dispersible Co nanoparticles. *Langmuir* **2007,** 23, 11409.

[26]. Kasture, M.; Sastry, M.; Prasad, B. L. V., Halide ion controlled shape dependent gold nanoparticle synthesis with tryptophan as reducing agent: Enhanced fluorescent properties and white light emission. *Chem. Phys. Lett.* **2010,** 484, 271.

[27]. Wang, Y.; Xia, Y., Bottom-Up and Top-down approaches to the synthesis of monodispersed spherical colloids of low melting-point metals. *Nano Lett.* **2004,** 4, 2047.

[28]. Silva, G. A., Neuroscience nanotechnology: progress, opportunities and challenges. *Nat. Rev. Neurosci.* **2006,** 7, 65.

[29]. Otto, S.; Furlan, R. L. E.; Sanders, J. K. M., Recent developments in dynamic combinatorial chemistry. *Curr. Opin. Chem. Biol.* **2002,** 6, 321.

[30]. Han, Y.; Nowak, P.; Colomb-Delsuc, M.; Leal, M. P.; Otto, S., Instructable nanoparticles using dynamic combinatorial chemistry. *Langmuir* **2015,** 31, 12658.

[31]. Osawa, E., Superaromaticity. *Kagaku* **1970,** 25, 854.

[32]. Kroto, H. W.; Heath, J. R.; Obrien, S. C.; Curl, R. F.; Smalley, R. E., C_{60}: Buckminsterfullerene. *Nature* **1985,** 318, 162.

[33]. Iijima, S., Helical microtubules of graphitic carbon. *Nature* **1991,** 354, 56.

[34]. Jiao, L. Y.; Zhang, L.; Wang, X. R.; Diankov, G.; Dai, H. J., Narrow graphene nanoribbons from carbon nanotubes. *Nature* **2009,** 458, 877.

[35]. Kosynkin, D. V.; Higginbotham, A. L.; Sinitskii, A.; Lomeda, J. R.; Dimiev, A.; Price, B. K.; Tour, J. M., Longitudinal unzipping of carbon nanotubes to form graphene nanoribbons. *Nature* **2009,** 458, 872.

[36]. Viculis, L. M.; Mack, J. J.; Kaner, R. B., A chemical route to carbon nanoscrolls. *Science* **2003,** 299, 1361.

[37]. Li, X.; Wang, X.; Zhang, L.; Lee, S.; Dai, H., Chemically derived, ultrasmooth graphene nanoribbon semiconductors. *Science* **2008,** 1229, 319.

[38]. Zeng, H. B.; Zhi, C. Y.; Zhang, Z. H.; Wei, X. L.; Wang, X. B.; Guo, W. L.; Bando, Y.; Golberg, D., "White Graphenes": Boron nitride nanoribbons via boron nitride nanotube unwrapping. *Nano Lett.* **2010,** 10, 5049.

[39]. Mas-Balleste, R.; Gomez-Navarro, C.; Gomez-Herrero, J.; Zamora, F., 2D materials: to graphene and beyond. *Nanoscale* **2011,** 3, 20.

[40]. Tiwari, J. N.; Tiwari, R. N.; Kim, K. S., Zero-dimensional, one-dimensional, two-dimensional and three-dimensional nanostructured materials for advanced electrochemical energy devices. *Prog. Mater. Sci.* **2012,** 57, 724.

[41]. Cronin, L.; Müller, A., From serendipity to design of polyoxometalates at the nanoscale, aesthetic beauty and applications. *Chem. Soc. Rev.* **2012,** 41, 7333.

[42]. Zhou, H.-C.; Long, J. R.; O. M. Yaghi, Introduction to Metal-Organic Frameworks. *Chem. Rev.* **2012,** 112, 673.

[43]. Gusev, A. I.; Rempel, A. A., Nanocrystalline Materials. *Cambridge International Science Publishing* **2004**.

[44]. Peierls, R. E., Quelques proprietes typiques des corpses solides. *Ann. I. H. Poincare* **1935,** 5, 177.

[45]. Landau, L. D., Zur Theorie der phasenumwandlungen II. *Phys. Z. Sowjetunion* **1937,** 11, 26.

[46]. Mermin, N. D., Crystalline order in two dimensions. **1968,** 176, 250.

[47]. Chen, Q.; Smith, J. M.; Park, J.; Kim, K.; Ho, D.; Rasool, H. I.; Zettl, A.; Alivisatos, A. P., 3D Motion of DNA-Au nanoconjugates in graphene liquid cell Electron microscopy. *Nano Letters* **2013,** 13, 4556.

[48]. Park, J.; Park, H.; Ercius, P.; Pegoraro, A. F.; Xu, C.; Kim, J. W.; Han, S. H.; Weitz, D. A., Direct observation of wet biological samples by graphene liquid cell transmission electron microscopy. *Nano Letters* **2015,** 15, 4737.

[49]. Wang, C.; Qiao, Q.; Shokuhfar, T.; Klie, R. F., High-resolution electron microscopy and spectroscopy of ferritin in biocompatible graphene liquid cells and graphene sandwiches. *Advanced Materials* **2014,** 26, 3410.

[50]. Ponomarenko, L. A.; Geim, A. K.; Zhukov, A. A.; Jalil, R.; Morozov, S. V.; Novoselov, K. S.; Grigorieva, I. V.; Hill, E. H.; Cheianov, V. V.; Fal'ko, V. I.; Watanabe, K.; Taniguchi, T.; Gorbachev, R. V., Tunable metal-insulator transition in double-layer graphene heterostructures. *Nat. Phys.* **2011,** 7, 958.

[51]. Geim, A. K.; Grigorieva, I. V., Van der Waals heterostructures. *Nature* **2013,** 499, 419.

[52]. Georgiou, T.; Jalil, R.; Belle, B. D.; Britnell, L.; Gorbachev, R. V.; Morozov, S. V.; Kim, Y. J.; Gholinia, A.; Haigh, S. J.; Makarovsky, O.; Eaves, L.; Ponomarenko, L. A.; Geim, A. K.; Novoselov, K. S.; Mishchenko, A., Vertical field-effect transistor based on graphene–WS_2 heterostructures for flexible and transparent electronics. *Nat. Nanotechnol.* **2013,** 8, 100.

[53]. Zhang, Z.; Zou, X.; Crespi, V. H.; Yakobson, B. I., Intrinsic magnetism of grain boundaries in two-dimensional metal dichalcogenides. *ACS Nano* **2013,** 7, 10475.

[54]. Azizi, A.; Eichfeld, S.; Geschwind, G.; Zhang, K.; Jiang, B.; Mukherjee, D.; Hossain, L.; Piasecki, A. F.; Kabius, B.; Robinson, J. A.; Alem, N., Freestanding van der Waals Heterostructures of Graphene and Transition Metal Dichalcogenides. *ACS Nano* ***2015,*** 9, 4882.

[55]. Tan, Y. W.; Zhang, Y.; Stormer, H. L.; Kim, P., Temperature dependent electron transport in graphene. *Euro. Phys. Jour.-Special Topics* **2007,** 148, 15.

[56]. Zhang, Y. B.; Tan, Y. W.; Stormer, H. L.; Kim, P., Experimental observation of the quantum Hall effect and Berry's phase in graphene. *Nature* **2005,** 438, 201.

[57]. Bunch, J. S.; Yaish, Y.; Brink, M.; Bolotin, K.; McEuen, P. L., Coulomb oscillations and Hall effect in quasi-2D graphite quantum dots. *Nano Lett.* **2005,** 5, 287.

[58]. Algara-Siller, G.; Lehtinen, O.; Wang, F. C.; Nair, R. R.; Kaiser, U.; Wu, H. A.; Geim, A. K.; Grigorieva, I. V., Square ice in graphene nanocapillaries. *Nature* **2015,** 519, 443.

[59]. Andersen, K.; Latini, S.; Thygesen, K. S., Dielectric genome of van der Waals heterostructures. *Nano Lett.* **2015,** 15, 4616.

[60]. Novoselov, K. S.; Geim, A. K.; Morozov, S. V.; Jiang, D.; Katsnelson, M. I.; Grigorieva, I. V.; Dubonos, S. V.; Firsov, A. A., Two-dimensional gas of massless Dirac fermions in graphene. *Nature* **2005,** 438, 197.

[61]. Lee, C.; Yan, H.; Brus, L. E.; Heinz, T. F.; Hone, J.; Ryu, S., Anomalous lattice vibrations of single- and few-layer MoS_2. *ACS Nano* **2010,** 4, 2695.

[62]. Chianelli, R. R.; Siadati, M. H.; De la Rosa, M. P.; Berhault, G.; Wilcoxon, J. P.; Bearden, R.; Abrams, B. L., Catalytic properties of single layers of transition metal sulfide catalytic materials. *Catal. Rev.-Sci. .Engg.* **2006,** 48, 1.

[63]. Ayari, A.; Cobas, E.; Ogundadegbe, O.; Fuhrer, M. S., Realization and electrical characterization of ultrathin crystals of layered transition-metal dichalcogenides. *J. Appl. Phys.* **2007,** 101, 014507.

[64]. Huang, X.; Qi, X. Y.; Boey, F.; Zhang, H., Graphene-based composites. *Chem. Soc. Rev.* **2012,** 41, 666.

[65]. Lemmon, J. P.; Wu, J. H.; Oriakhi, C.; Lerner, M. M., Preparation of nanocomposites containing poly(ethylene oxide) and layered solids. *Electrochim. Acta* **1995,** 40, 2245.

[66]. Fu, X.; Qutubuddin, S., Polymer-clay nanocomposites: exfoliation of organophilic montmorillonite nanolayers in polystyrene. *Polymer* **2001,** 42, 807.

[67]. Novoselov, K. S.; Geim, A. K.; Morozov, S. V.; Jiang, D.; Zhang, Y.; Dubonos, S. V.; Grigorieva, I. V.; Firsov , A. A., Electric field effect in atomically thin carbon films. *Science* **2004,** 306, 666.

[68]. Joensen, P.; Frindt, R. F.; Morrison, S. R., Single-layer MoS_2. *Mat. Res. Bull.* **1986,** 21, 457.

[69]. Novoselov, K. S.; Jiang, D.; Schedin, F.; Booth, T. J.; Khotkevich, V. V.; Morozov, S. V.; Geim, A. K., Two-dimensional atomic crystals. *Proc. Natl. Acad. Sci. U. S. A.* **2005,** 102, 10451.

[70]. Matte, H. S. S. R.; Gomathi, A.; Manna, A. K.; Late, D. J.; Datta, R.; Pati, S. K.; Rao, C. N. R., MoS_2 and WS_2 analogues of graphene. *Angew. Chem. Intl. Ed.* **2010,** 122, 4153.

[71]. Liu, H.; Hsu, C.-H.; Lin, Z.; Shan, W.; Wang, J.; Jiang, J.; Huang, M.; Lotz, B.; Yu, X.; Zhang, W.-B.; Yue, K.; Cheng, S. Z. D., Two-dimensional nanocrystals of molecular janus particles. *J. Am. Chem. Soc.* **2014,** 136, 10691.

[72]. Sasaki, T.; Watanabe, M., Osmotic swelling to exfoliation. exceptionally high degrees of hydration of a layered titanate. *J. Am. Chem. Soc.* **1998,** 120, 4682.

[73]. Nicolosi, V.; Chowalla, M.; Kanatzidis, M., G.; Strano, M., S.; Coleman, J., N., Liquid exfoliation of layered materials. *Science* **2013,** 340, 1420.

[74]. Hernandez, Y.; Nicolosi, V.; Lotya, M.; Blighe, F. M.; Sun, Z.; De, S.; McGovern, I. T.; Holland, B.; Byrne, M.; Gun'Ko, Y. K.; Boland, J. J.; Niraj, P.; Duesberg, G.; Krishnamurthy, K.; Goodhue, R.; Hutchison, J.; Scardaci, V.; Ferrari, A. C.; Coleman, J., N., High-yield production of graphene by liquid-phase exfoliation of graphite. *Nat. Nanotechnol.* **2008,** 3, 563.

[75]. Coleman, J. N.; Lotya, M.; O'Neill, A.; Bergin, S. D.; King, P. J.; Khan, U.; Young, K.; Gaucher, A.; De, S.; Smith, R. J.; Shvets, I. V.; Arora, S. K.; Stanton, G.; Kim, H. Y.; Lee, K.; Kim, G. T.; Duesberg, G. S.; Hallam, T.; Boland, J. J.; Wang, J. J.; Donegan, J. F.; Grunlan, J. C.; Moriarty, G.; Shmeliov, A.; Nicholls, R. J.; Perkins, J. M.; Grieveson, E. M.; Theuwissen, K.; McComb, D. W.; Nellist, P. D.; Nicolosi, V., Two-dimensional nanosheets produced by liquid exfoliation of layered materials. *Science* **2011,** 331, 568.

[76]. Osada, M.; Sasaki, T., Exfoliated oxide nanosheets: new solution to nanoelectronics. *J. Mater. Chem.* **2009,** 19, 2503.

[77]. Pokroy, B.; Aichmayer, B.; Schenk, A. S.; Haimov, B.; Kang, S. H.; Fratzl, P.; Aizenberg, J., Sonication-assisted synthesis of large, high-quality mercury thiolate single crystals directly from liquid mercury. *J. Am. Chem. Soc.* **2010,** 132, 14355.

[78]. Chalasani, R.; Gupta, A.; Vasudevan, S., Engineering new layered solids from exfoliated inorganics: a periodically alternating hydrotalcite – montmorillonite layered hybrid. *Nat. Sci. Rep.* **2013,** 3, 3498.

[79]. Gopakumar, T. G.; Lee, J. A.; Kontopoulou, M.; Parent, J. S., Influence of clay exfoliation on the physical properties of montmorillonite/polyethylene composites. *Polymer* **2002,** 43, 5483.

[80]. Dines, M. B., Intercalation in layered compounds. *J. chem. edu.* **1971,** 51, 221.

[81]. Benavente, E.; Santa Ana, M. A.; Mendizabal, F.; Gonzalez, G., Intercalation chemistry of molybdenum disulfide. *Coord. Chem. Rev.* **2002,** 224, 87.

[82]. Yang, D.; Frindt, R. F., Li-intercalation and exfoliation of WS_2. *J. Phys. Chem. Solids* **1996,** 57, 1113.

[83]. Wang, L.; Kanatzidis, M. G., Laminated TaS_2/polymer nanocomposites through encapsulative precipitation of exfoliated layers. *Chem. Mater.* **2001,** 13, 3717.

[84]. Miremadi, B. K.; Morrison, S. R., The intercalation and exfoliation of tungsten disulfide. *J. Appl. Phys.* **1988,** 63, 4970.

[85]. Dines, M. B., Lithium intercalation via - Butyllithium of the layered transition metal dichalcogenides. *Mater. Res. Bull.* **1975,** 10, 287.

[86]. Chrissafis, K.; Zamani, M.; Kambas, K.; Stoemenos, J.; Economou, N. A.; Samaras, I.; Julien, C., Structural studies of MoS_2 intercalated by lithium. *Mater. Sci. and Engg. B-Solid State Mater. Adv. Technol.* **1989,** 3, 145.

[87]. Nam, K. T.; Shelby, S. A.; Choi, P. H.; Marciel, A. B.; Chen, R.; Tan, L.; Chu, T. K.; Mesch, R. A.; Lee, B. C.; Connolly, M. D.; Kisielowski, C.; Zuckermann, R. N., Free-floating ultrathin two-dimensional crystals from sequence-specific peptoid polymers. *Nat Mater.* **2010,** 9, 454.

[88]. Sanii, B.; Kudirka, R.; Cho, A.; Venkateswaran, N.; Olivier, G. K.; Olson, A. M.; Tran, H.; Harada, R. M.; Tan, L.; Zuckermann, R. N., Shaken, not stirred: collapsing a peptoid monolayer to produce free-floating, stable nanosheets. *J. Am. Chem. Soc.* **2011,** 133, 20808.

[89]. Hughes, J. M.; Hernandez, Y.; Aherne, D.; Doessel, L.; Müllen, K.; Moreton, B.; White, T. W.; Partridge, C.; Costantini, G.; Shmeliov, A.; Shannon, M.; Nicolosi, V.; Coleman, J., N., High quality dispersions of hexabenzocoronene in organic solvents. *J. Am. Chem. Soc* **2012,** 134, 12168.

[90]. Mann, F. G.; Purdie, D., The constitution of complex metallic salts. Part III. The para-chors of palladium and mercury in simple and complex compounds. *J. Chem. Soc.* **1935**, 1549.

[91]. Thomas, P. J.; Lavanya, A.; Sabareesh, S.; Kulkarni, G. U., Self-assembling bilayers of palladiumthiolates in organic media. *Proc. Indian Acad. Sci. (Chem. Sci.).* **2001,** 113, 611.

[92]. John, N. S.; Thomas, P. J.; Kulkarni, G. U., Self-assembled hybrid bilayers of palladium alkanethiolates. *J. Phys. Chem. B* **2003,** 107, 11376.

[93]. Wertheim, E., Derivatives for the identification of mercaptans. *J. Am. Chem. Soc* **1929,** 51, 3661.

[94]. Shaw, R. A.; Woods, M., Preparation and some properties of lead thiolates. *J. Chem. Soc. A* **1971**, 1569.

[95]. Dance, I. G.; Fisher, K. J.; Banda, R. M. H.; Scudder, M. L., Layered structure of crystalline compounds AgSR. *Inorg. Chem.* **1991,** 30, 183.

[96]. Pokroy, B.; Aichmayer, B.; Schenk, A. S.; Haimov, B.; Kang, S. H.; Fratzl, P.; Aizenberg, J., Sonication-assisted synthesis of large, high-quality mercury thiolate single crystals directly from liquid mercury. *J. Am. Chem. Soc.* **2010,** 132, 14355.

[97]. Sandhyarani, N.; Pradeep, T., An investigation of the structure and properties of layered copper thiolates. *J. Mater. Chem.* **2001,** 11, 1294.

[98]. Hu, L.; de la Rama, L. P.; Efremov, M. Y.; Anahory, Y.; Schiettekatte, F.; Allen, L. H., Synthesis and characterization of single-layer silver-decanethiolate lamellar crystals. *J. Am. Chem. Soc.* **2011,** 133, 4367.

[99]. Rosemary, M. J.; Pradeep, T., Solvothermal synthesis of silver nanoparticles from thiolates. J. Colloid Interface Sci. 2003, 268, 81.

[100]. Bhuvana, T.; Boley, W.; Radha, B.; Dolash, B. D.; Chiu, G.; Bergstrom, D.; Reifenberger, R.; Fisher, T. S.; Kulkarni, G. U., Inkjet printing of palladium alkanethiolates for facile fabrication of metal interconnects and surface-enhanced Raman scattering substrates. *Micro & Nano Lett.* **2010,** 5, 296.

[101]. Bhuvana, T.; Gregoratti, L.; Heun, S.; Dalmiglio, M.; Kulkarni, G. U., Electron resist behavior of Pd hexadecanethiolate examined using X-ray photoelectron spectroscopy with nanometric lateral resolution. *Langmuir* **2009,** 25, 1259.

[102]. Bhuvana, T.; Kulkarni, G. U., A SERS-active nanocrystalline Pd substrate and its nanopatterning leading to biochip fabrication. *Small* **2008,** 4, 670.

[103]. Voiry, D.; Salehi, M.; Silva, R.; Fujita, T.; Chen, M.; Asefa, T.; Shenoy, V. B.; Eda, G.; Chhowalla, M., Conducting MoS_2 Nanosheets as Catalysts for Hydrogen Evolution Reaction. *Nano Lett.* **2013,** 13, 6222.

[104]. Busupalli, B.; Date, K.; Datar, S.; Prasad, B. L. V., Preparation of Ni_3S_2 and Ni_3S_2-Ni Nanosheets via Solution Based Processes. *Cryst. Growth & Des.* **2015,** 15, 2584.

[105]. Fan, Z.; Huang, X.; Tan, C.; Zhang, H., Thin metal nanostructures: synthesis, properties and applications. *Chem. Sci.* **2015,** 6, 95.

[106]. Huang, X.; Tang, S.; Mu, X.; Dai, Y.; Chen, G.; Zhou, Z.; Ruan, F.; Yang, Z.; Zheng, N., Freestanding palladium nanosheets with plasmonic and catalytic properties. *Nat Nanotechnol.* **2011,** 6, 28.

[107]. Zhang, N.; Ma, W.; Wu, T.; Wang, H.; Han, D.; Niu, L., Edge-rich MoS_2 Naonosheets Rooting into Polyaniline Nanofibers as Effective Catalyst for Electrochemical Hydrogen Evolution. *Electrochim. Acta* **2015,** 180, 155.

[108]. Xia, B.; An, L.; Gao, D.; Shi, S.; Xi, P.; Xue, D., Hierarchical ultrathin $Mo(S_xSe_{1-x})_2$ nanosheets with tunable ferromagnetism and efficient hydrogen evolution reaction activity: towards defect site effect. *Cryst. Eng. Chem.* **2015,** 17, 6420.

[109]. Zhang, L.; Wu, H.; Yan, Y.; Wang, X.; Lou, D. X.-W., Hierarchical MoS_2 microboxes constructed by nanosheets with enhanced electrochemical properties for lithium storage and water splitting. *Energy Environ. Sci.* **2014,** 7, 3302.

[110]. Zhao, X.; Zhu, H.; Yang, X., Amorphous carbon supported MoS_2 nanosheets as effective catalysts for electrocatalytic hydrogen evolution. *Nanoscale* **2014,** 6, 10680.

[111]. Mao, X.; Xu, Y.; Xue, Q.; Wang, W.; Gao, D., Ferromagnetism in exfoliated tungsten disulfide nanosheets. *Nanoscale Res. Lett.* **2013,** 8, 1.

[112]. Ma, R.; Sasaki, T., Nanosheets of oxides and hydroxides: ultimate 2D charge-bearing functional crystallites. *Advanced Materials* **2010,** 22, 5082.

[113]. Durst, J.; Simon, C.; Hasché, F.; Gasteiger, H. A., Hydrogen oxidation and evolution reaction kinetics on carbon supported Pt, Ir, Rh, and Pd electrocatalysts in acidic media. *J. Electrochem. Soc.* **2015,** 162, 190.

[114]. Zheng, Z.; Zhang, X.; Neumann, C.; Emmrich, D.; Winter, A.; Vieker, H.; Liu, W.; Lensen, M.; Golzhauser, A.; Turchanin, A., Hybrid van der Waals heterostructures of zero-dimensional and two-dimensional materials. *Nanoscale* **2015,** 7, 13393.

[115]. Gao, D.; Xue, Q.; Mao, X.; Wang, W.; Xu, Q.; Xue, D., Ferromagnetism in ultrathin VS_2 nanosheets. *J. Mat. Chem. C.* **2013,** 1, 5909.

[116]. Han, Y.; Hu, T.; Li, R.; Zhou, J.; Dong, J., Stabilities and electronic properties of monolayer MoS_2 with one or two sulfur line vacancy defects. *Phys. Chem. Chem.Phys* **2014,** 17, 3813.

[117]. John, N. S.; Kulkarni, G. U.; Datta, A.; Pati, S. K.; Komori, F.; Kavitha, G.; Narayana, C.; Sanyal, M. K., Magnetic interactions in layered nickel alkanethiolates. *J. Phys. Chem. C.* **2007,** 111, 1868.

[118]. Colson, A. C.; Chen, C.-W.; Morosan, E.; Whitmire, K. H., Synthesis of phase-pure ferromagnetic Fe_3P films from single-source molecular precursors. *Adv. Funct. Mater.* **2012,** 22, 1850.

[119]. Falkowski, J. M.; Concannon, N. M.; Yan, B.; Surendranath, Y., Heazlewoodite, Ni_3S_2: A potent catalyst for oxygen reduction to water under benign conditions. *J. Am. Chem. Soc* **2015,** 137, 7978.

[120]. Shinde, D. V.; Patil, S. A.; Cho, K.; Ahn, D. Y.; Shrestha, N. K.; Mane, R. S.; Lee, J. K.; Han, S.-H., Revisiting metal sulfide semiconductors: a solution-based general protocol for thin film formation, hall effect measurement, and application prospects. *Adv. Funct. Mater.* **2015,** 25, 5739.

Chapter 2

Solution state structural evaluation of self assembling molecularly thin metal thiolate nanosheets

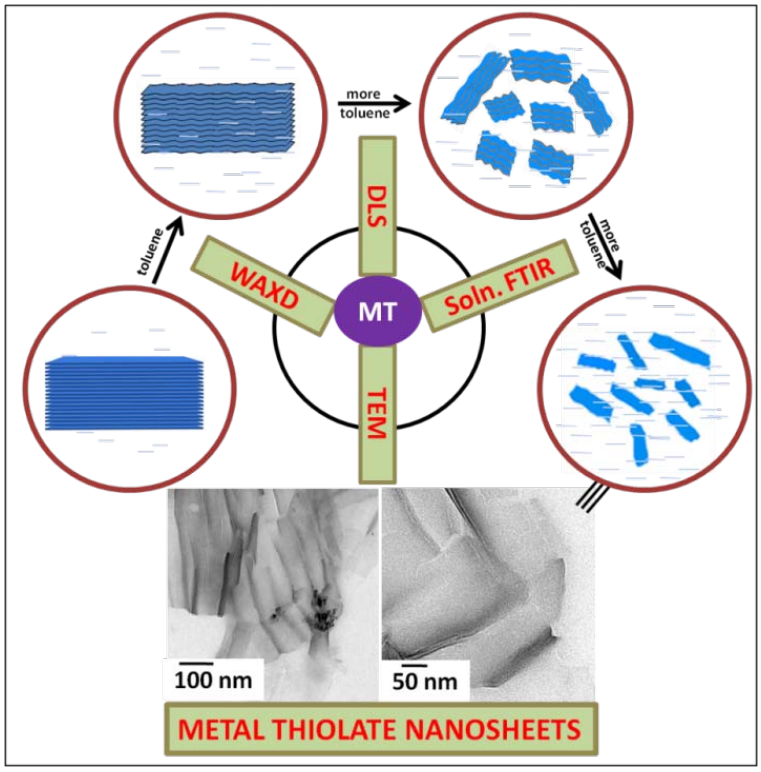

This chapter is dedicated to the studies undertaken on the synthesis and the solution state structural evaluation of novel two dimensional organic-inorganic hybrid molecular materials, namely the metal thiolates. The solution state structure of the metal thiolates was thoroughly elucidated using several solution state techniques. This work serves as foundation to the work carried out further in this thesis.

Part of the work described in this chapter has been published in:

Busupalli, B.; Kummara, S.; Kumaraswamy, G.; Prasad, B. L. V., Ultrathin sheets of metal or metal sulfide from molecularly thin sheets of metal thiolates in solution. *Chem. Mater.*, **2014,** 26, 3436.

2.1 Introduction

Metal thiolates are emerging as an important class of layered materials due to their complete solubility in several organic solvents, which could allow accessing them as soluble precursors for ultrathin metal/metal sulfide sheets. As described in the previous chapter, metal thiolates can be divided majorly into two types based on the oxidation state of the coordinating metal ion in the thiolate. In the first type, such as in silver thiolates [1, 2] and copper (I) thiolates [3], the metal ion is in the (+1) oxidation state. Another type comprises of examples like palladium [4], nickel, copper (II) thiolates etc. wherein the metal ion is in (+2) oxidation state [5-7]. Such a change in oxidation state imparts great differences as far as the solubility of these thiolates in non-polar organic solvents is concerned [8-31]. The amphiphilic characteristics arise due to the presence of hydrophilic metal-sulfur coordination on one end and hydrophobic long alkyl chains on the other end as shown in the Figure 2.1 below. The solubility parameters, however, are mainly influenced by the strength of the bonding between the metal and sulfurs of the alkyl chains.

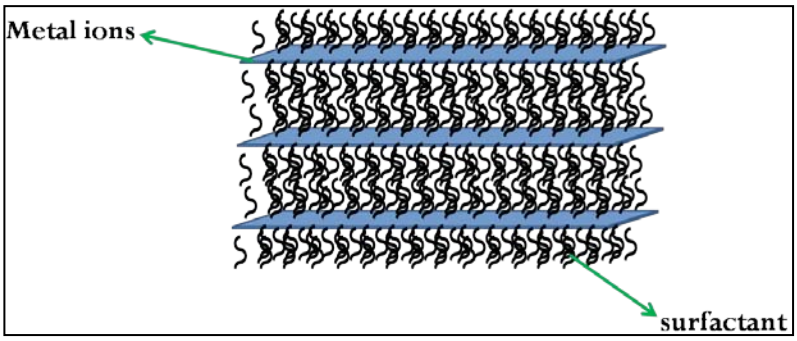

Figure 2.1: *Schematic representation of the layered metal thiolate model.*

In any case, the highly soluble nature of the palladium and nickel thiolates attracted us and we proceeded towards establishing the solution structure of the layered metal thiolate compounds by exfoliating them in non-polar organic solvents as shown schematically in Figure 2.2 below. This allowed us to harness these materials as precursors for different types of nanoscale materials as becomes evident by our work included in the later

chapters of this thesis. In this chapter we discuss the results of a comprehensive solution state analysis of the structural features of these thiolates.

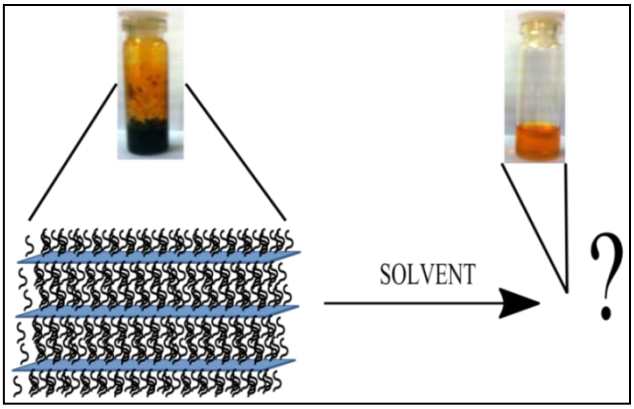

Figure 2.2: *Schematic representation of the layered metal thiolate during its exfoliation process.*

2.2 Synthesis of the model metal thiolate-palladium octanethiolate

Palladium octanethiolate was initially synthesized as per the reported general procedure [4]. However, for the type of thorough solution state structural analysis that we wanted to carryout, the quantities of metal thiolates resulting from the reported procedures were not sufficient. Therefore, initially we resorted to synthesize them in several small batches. Accordingly, 3 mg of Palladium acetate was dissolved in 1.5 mL of distilled toluene in an eppendorf centrifuge tube (2 mL capacity) and 2.3 µL of octanethiol was added to it. The mixture was shaken vigorously till it turned to orange-red. This process of forming lamellae simply by shaking the reaction mixture is interesting in itself. Many such tubes were used to synthesize the material as shown in the Figure 2.3 below, and the material in all the tubes was later added into a round-bottom flask.

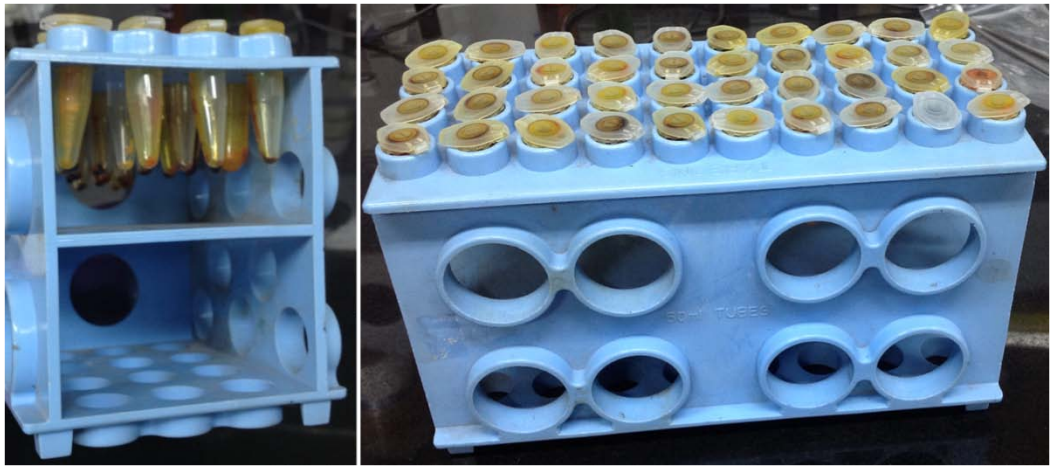

Figure 2.3: *The synthesis of palladium octanethiolate in eppendorf tubes. The materials had to be synthesized in many batches to access reasonably large quantities for different analyses.*

The sample in the flask was washed thoroughly with methanol and the solvent was removed to result in a highly viscous waxy material. Then, the products from different reaction tubes were mixed together. Obviously, this will raise a question about the confirmation of the product in these different batches and also this repetitive preparation is quite cumbersome.

Subsequently, we found an easy and convenient method for preparing large quantities of this material by modifying the reported procedures slightly. Accordingly, palladium, nickel, mercury and lead thiolates were prepared using this modified procedure. This modified procedure is as follows.

500 mg palladium of acetate was taken in a glass tube of 5 mL capacity. To this, 900 µL of octanethiol was added and the glass tube was shaken vigorously. The reaction mixture turned orange-red instantaneously as shown in the Figure 2.4 below, in which a series of photographs represented the actual experiment for preparing large quantities of the palladium octanethiolate. The mixture was washed thoroughly (5–6 times) using ethanol, and the orange-red product was air-dried at room temperature. The obtained orange-red

sticky substance is readily soluble in organic solvents such as chloroform, toluene, CCl_4, etc. The similarity of this product with that prepared using reported procedure was estimated using PXRD and UV-visible spectra.

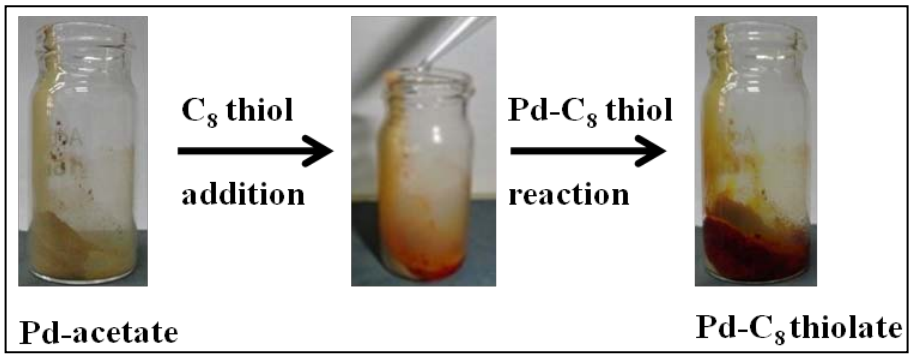

Figure 2.4: *Illustration of the synthesis of palladium octanethiolate in large quantities.*

We wish to mention that this modified procedure worked equally well with other metal thiolates, as described in the following section, and furnished gram quantities of the respective metal thiolate materials.

2.3 Synthesis of the other metal thiolate materials

The synthetic procedures for preparing the other metal thiolates are described below. To test the same synthetic procedure for other thiol ligands in place of octanethiol, palladium dodecanethiolate was also synthesized by the same procedure.

2.3.1. Synthesis of nickel octanethiolate

To 500 mg nickel acetylacetonate taken in a glass tube of 5 mL capacity, 900 µL of octanethiol was added and the tube was shaken vigorously. The reaction mixture turned black instantaneously. The mixture was washed thoroughly with 1 mL ethanol for 5-6 times and the black product was air-dried at room temperature. The obtained black powder goes readily into organic solvents such as chloroform, toluene, CCl_4 etc. and the powder was characterized using PXRD, TEM, UV-visible spectroscopy.

2.3.2. Synthesis of mercury octanethiolate

To 500 mg mercuric nitrate taken in a glass tube of 5 mL capacity, 900 µL of octanethiol was added and the tube was shaken vigorously. Caution should be maintained while shaking the reaction mixture as the reaction is highly exothermic. The reaction mixture turned colorless instantaneously. The mixture was washed thoroughly with 1 mL ethanol for 5-6 times and the white product thus obtained was air-dried at room temperature. The white powder goes readily into organic solvents such as chloroform, toluene, CCl_4 etc. and the powder was characterized using PXRD, TEM.

2.3.3. Synthesis of lead octanethiolate

To 500 mg lead acetate (II) trihydrate taken in a glass tube of 5 mL capacity, 900 µL of octanethiol was added and the tube was shaken vigorously. The reaction mixture turned yellow in color instantaneously. The mixture was washed thoroughly with 1 mL ethanol for 5-6 times and the yellow product was air-dried at room temperature. The obtained yellow powder goes readily into organic solvents such as chloroform, toluene, CCl_4 etc. and the powder was characterized using PXRD, TEM.

2.3.4. Synthesis of palladium dodecanethiolate

To 500 mg palladium acetate taken in a glass tube of 5 mL capacity, 900 µL of dodecanethiol was added and the tube was shaken vigorously. The reaction mixture turned yellowish-red instantaneously. The mixture was washed thoroughly with 1 mL ethanol for 5-6 times and the yellowish-red product was air-dried at room temperature. The obtained yellowish-red powder goes readily into organic solvents such as chloroform, toluene, CCl_4 etc. and the powder was characterized using PXRD, TEM.

2.3.5. Synthesis of palladium dodecanethiolate hexamer

In order to establish the layered nature of dissolved palladium octanethiolate remaining intact in solution, we needed to compare its characteristics with some model small molecular materials. Accordingly, we prepared palladium dodecanethiolate hexamer as

per literature reports [32]. Accordingly, to 0.588 g of Na_2PdCl_4 taken into 10 mL 4-*tert*-butyl toluene in a round bottom flask, 0.98 mL of dodecanethiol was added and the reaction mixture was refluxed in an oil bath under argon atmosphere at 192 °C for 1 hour. The flask was then removed and cooled and the mixture was poured into 100 mL ethanol taken in another round bottom flask. This mixture was stirred overnight resulting in orange precipitate. The product was centrifuged, washed with ethanol and dried.

2.4 Results and Discussion

2.4.1 Basic characterization of palladium octanethiolate

Before proceeding to the solution state structural evaluation of palladium octanethiolate, a basic structural characterization of this material was performed via the following spectroscopic techniques.

2.4.1. (a) UV-visible spectroscopy

The UV-visible spectrum of palladium octanethiolate dissolved in toluene is displayed in the Figure 2.5 below and it can be noticed clearly that this material does not show any absorbance above 520 nm.

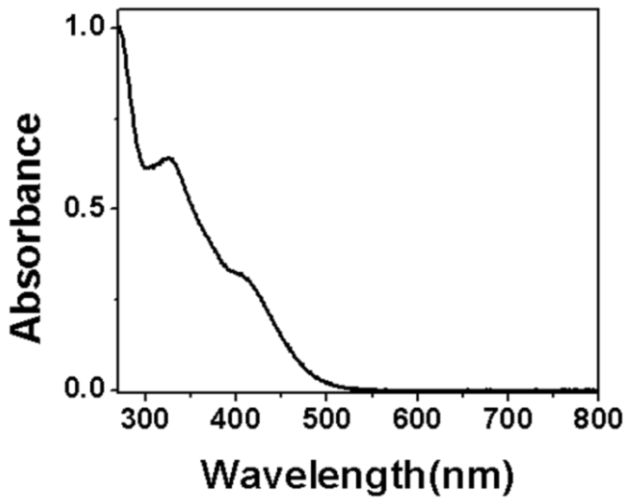

Figure 2.5: *UV-visible spectrum of palladium octanethiolate in toluene.*

2.4.1. (b) Energy dispersive analysis of X-rays (EDAX) spectroscopy

Energy dispersive analysis of X-rays (EDAX) spectroscopy of the palladium octanethiolate shown in the Figure 2.6 below registers the molecular stoichiometry of the palladium coordinated to two sulfurs.

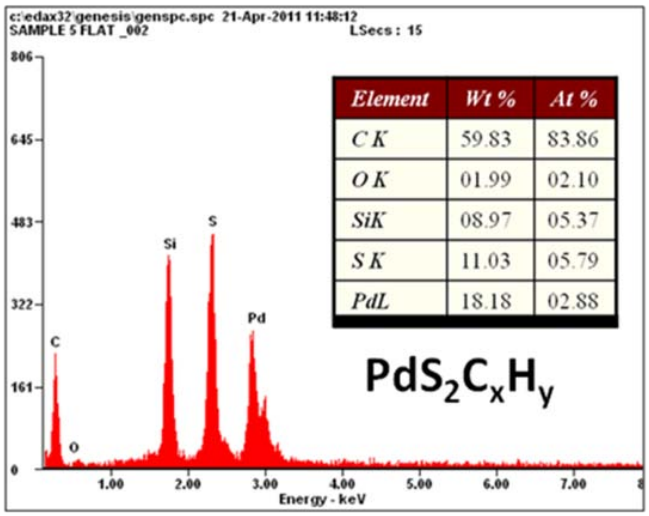

Figure 2.6: *Energy dispersive X-ray analysis of palladium octanethiolate. From this, the stoichiometry of the material could be analyzed.*

2.4.2 Basic characterization of palladium dodecanethiolate hexamer

Basic characterization of the hexameric palladium dodecanethiolate was performed by employing UV-visible spectroscopy and powder XRD. These results are displayed in Figure 2.7 below. The single crystal structure of the compound has already been solved and reported by Klabunde et al. The same is depicted in Figure 2.8 [32].

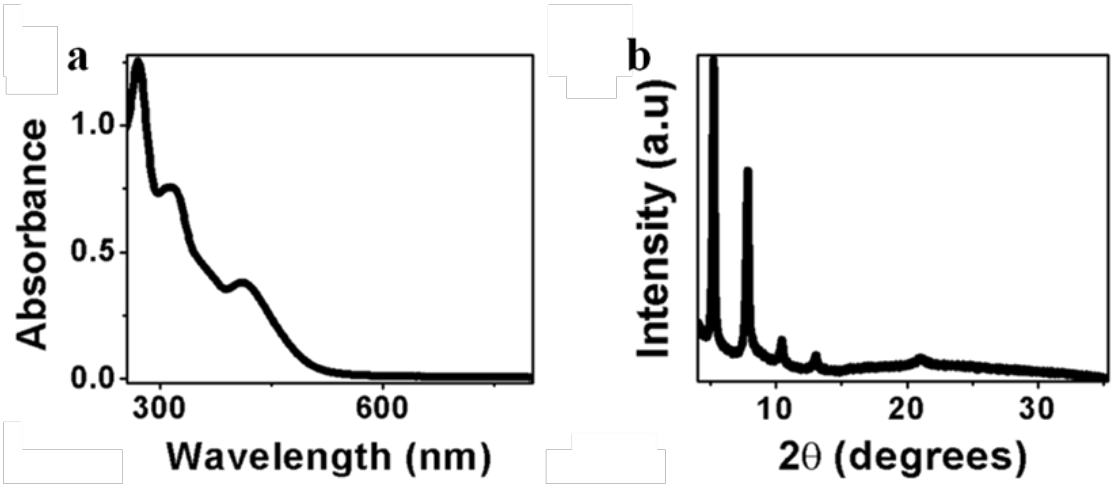

Figure 2.7: *a) UV-visible spectra of the palladium dodecanethiolate hexamer. b). PowderXRD pattern of the same.*

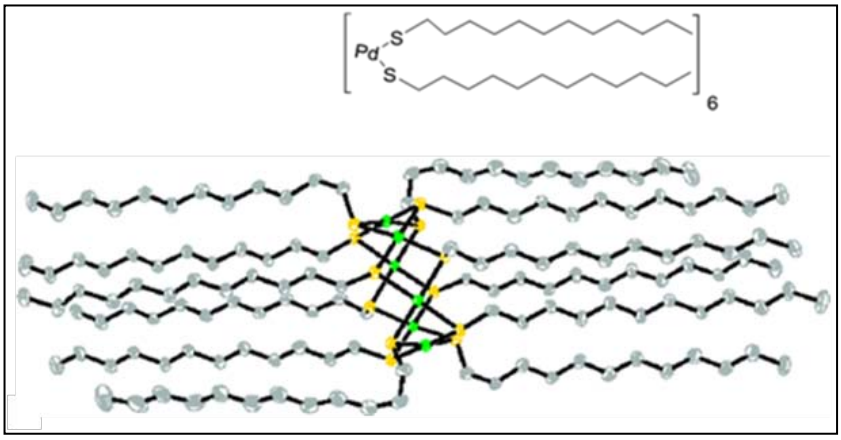

Figure 2.8: *Crystal structure of the palladium dodecanethiolate hexamer [adapted from ref.15].*

2.4.3 Solution state structural characterization of the palladium octanethiolate

After obtaining gram scale quantities of the palladium octanethiolate, we proceeded to thoroughly characterize the solution state structural features of the same employing the following solution state characterization techniques.

2.4.3. (a) Wide angle x-ray diffraction (WAXD)

After confirming the lamellar registry in solid film of palladium octanethiolate characterized via Powder XRD (Figure 2.9a) with the 2• values of 3.9, 7.8, and 11.7°, (in the Figure 2.9b the proposed solid state structure of the laminated sheets is presented), it was apparent that a sequential delamination of the palladium octanethiolate lamellae could be performed by simply adding a non-polar solvent such as toluene or chloroform to it in particular volumes to further investigate its solution state structure through WAXD. Hence the solid was diluted to 500% w/v, 300% w/v, 100% w/v and 90% w/v. The as diluted samples were packed into very narrow quartz tubes and the tubes were sealed without a trace of gap in order to avoid evaporation of the solvent from the as prepared samples. A Rigaku rotating anode diffractometer having CuK• (• = 1.54Å) as the source radiation consisting R-axis IV image plate was utilized for obtaining the WAX diffraction data. The scanning time was set at one minute. Rotating anode oscillations were set at +/- 0.5° per minute. 80 mm distance was maintained between the rotational anode with the sample mounted on it and the detector. A reference high density polyethylene film (HDPE film) was kept at constant position for all the samples between the sample and the beam stop.

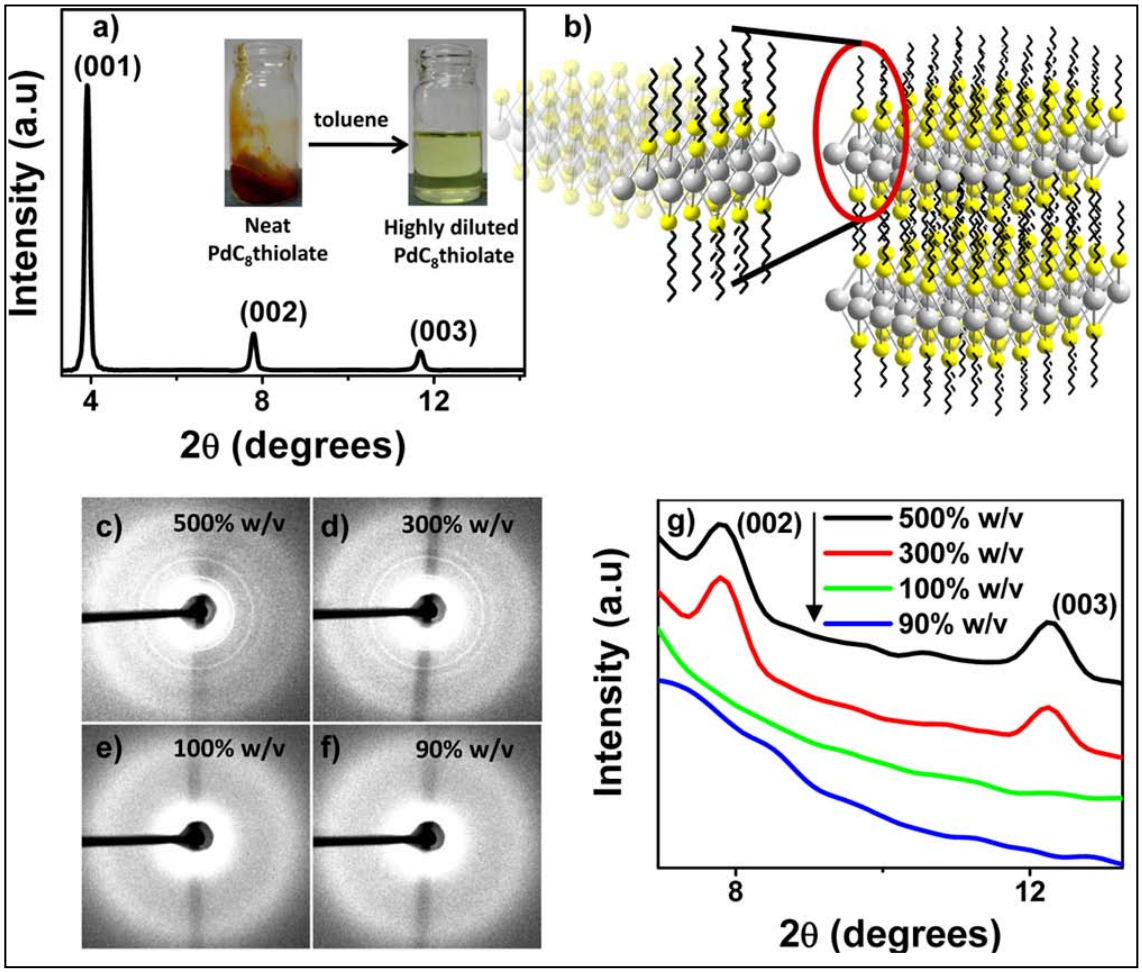

Figure 2.9: *a) Powder XRD pattern of Pd-octanethiolate showing lamellar (00l) reflections (inset shows photographs of Pd-octanethiolate in a solvent-free state (1 g material) and after solvent addition (50 mg in 5 mL of toluene)). (b) Plausible structure of the palladium thiolate lamellae. (c, d, e, and f) 2D WAXD patterns for the samples at 500% w/v, 300% w/v, 100% w/v, and 90% w/v. (g) The corresponding 1D plots of the WAXD for the same samples.*

The as obtained WAXD data were in 2D images format as represented in the Figures 2.9 c-f. 1D plots were deduced from these 2D images through Image J free software from NIH. The 1D plots obtained by this procedure are presented in Figure 2.9g.

At 500% w/v, the WAXD pattern displays multiple concentric rings, indicating orientational isotropy [33-38] over the diffracting sample volume. The rings correspond to diffraction peaks at the same 2• values as for the "powder" XRD from the neat Pd-

octanethiolate (Figure 2.9a). However, there is a decrease in the diffracted intensity and an increase in peak width relative to the neat sample (Figure 2.9g). Similarly, peak width or full width at half maximum (FWHM) increased from 0.54 degrees for 500% w/v sample to 0.63 degrees for 300% w/v sample (Figure 2.10). The regular spacing of the diffraction rings indicates that lamellar order is preserved in the solution state, at this concentration also. Interestingly, there is no swelling of the lamellar phase, viz. no change in the 2• values for the lamellar diffraction peaks on dilution with toluene to 500% w/v. Thus, the X-ray data indicates that, on dilution of the Pd-octanethiolate to 500% w/v in toluene, the average spacing between the thiolate lamellae is unchanged—however, there is a decrease in the coherence length of the diffracting lamellar stacks and increased disorder within the stacks [39]. Samples diluted further (up to 300% w/v) showed similar WAXD patterns as that of the 500% w/v sample (as is evident from the corresponding 1D plots, Figure 2.9g). Increasing the dilution to 100% w/v and 90% w/v of the Pd-octanethiolate in toluene resulted in complete disappearance of the diffraction rings (Figure 2.9e and 2.9f), indicating a loss of lamellar order. This suggests the initiation of the disintegration/delamination of the palladium octanethiolate lamellae at 100 % w/v concentration.

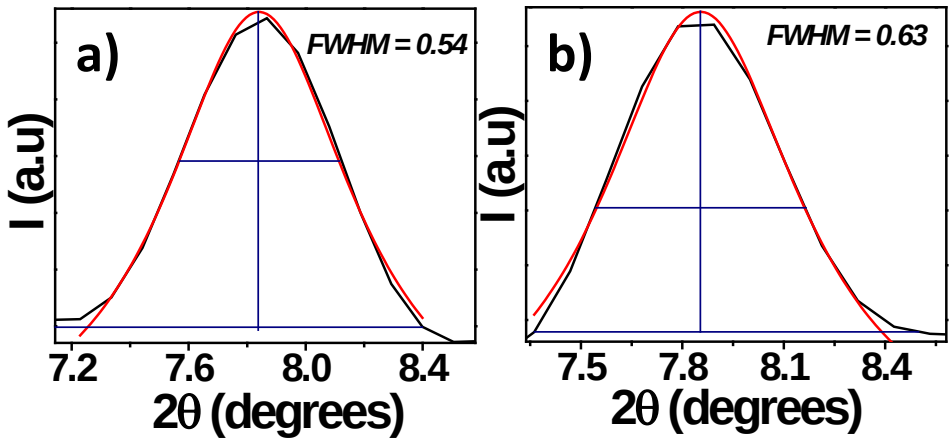

Figure 2.10: *FWHM calculation. FWHM (Full Width at Half Maximum) of the second lamellar peak for the (a) (b) 500% w/v sample and for (c) 300% w/v sample from the WAXD experiments.*

2.4.3. (b) Light scattering

As WAXD experiments predicted lost of lamellar registry in palladium octanethiolate at 100% w/v, light scattering was employed to further investigate the fate of the lamellae below the 100% w/v concentration. Both static and dynamic light scattering data were collected on at least three different batches of the palladium octanethiolate samples. The samples were scrupulously filtered into cylindrical glass cuvettes of 1 cm diameter and 10 cm height, using a 0.2 µm PTFE hydrophobic filter that would restrict any impurities by filtering them out, and immersed into a vat pre-filled with dust free toluene (viscosity of toluene = 1.496 Cp) kept constant at 25 °C. The samples studied with the light scattering experiments were prepared starting from 100% w/v to 1.67% w/v through 60% w/v, 50% w/v, 40% w/v, 30% w/v, 20% w/v, 10% w/v, 5% w/v. 1000 mg of the sample was dissolved in 1 mL of toluene (analytical reagent grade) to get 100% w/v of the sample in solution and then this 100% w/v sample was diluted carefully by filtering toluene (analytical reagent grade) into it. Light scattering was then performed using a 3D-DLS equipment (LS instruments) employing a He-Ne laser (Uniphase) of wavelength 632.8 nm with an inbuilt auto-correlator. Samples at higher concentrations (above 100% w/v), could not be filtered using a 0.2 µm filter, precluding light scattering measurements for this sample. DLS was repeated at least twice for independently prepared samples at each concentration and was observed to be quantitatively reproducible. Multi angle DLS was performed on Pd-octanethiolate sample at 50% w/v, 40% w/v, 30% w/v, 20% w/v and 10% w/v. The data were collected at angles 45-60-75-90-105-120 degrees. This was repeated for at least three times and the results were consistent. Static light scattering was performed on palladium octanethiolate starting from 50% w/v and then subsequently up to 1.667% w/v by dilution through 40% w/v, 30% w/v, 20% w/v, 10% w/v and 5% w/v. Intensity versus q was plotted in log-linear scale.

Palladium octanethiolate is a yellow colored material–however, it does not absorb in the visible above a wavelength of 520 nm (as shown in Figure 2.5), thus making it possible to perform light scattering experiments on the sample using red He-Ne laser light (• = 632.8 nm).

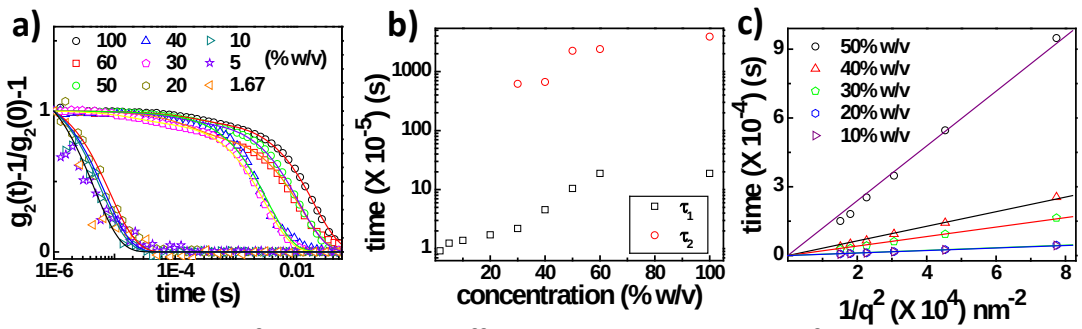

Figure 2.11: *a) DLS for samples at different concentrations viz. from 100% w/v to 1.67% w/v in toluene. The solid lines represent fitting curves obtained using equation 2. b) Plot showing relation between relaxation times and the concentration. Concentrations from 30% w/v to 100% w/v show two distinct decay times (τ_1 and τ_2) whereas samples at 20% w/v and below show single relaxation (τ_1). c) Fast relaxation time scales from multi angle DLS of palladium octanethiolate at different concentrations from 50% w/v to 10% w/v through 40% w/v, 30% w/v and 20% w/v plotted as a function of $1/q^2$ show linear dependence.*

The intensity-intensity time correlation function, $g_{(2)}(q,t)$, was obtained at 90°.

$$g_{(2)}(q,t) = < I(q,t)I(q,0) > / < I(q,0)^2 > .....[1]$$

For concentrations ≤ 20% w/v, the correlation function shows a single stage decay. At concentrations between 20% and 30% w/v, there is an abrupt qualitative change in the relaxation behaviour. Concentrations • 30% w/v, show a two-stage decay (Figure 2.11a). Correlation function was fitted with an empirical expression of the form:

$$g_{(2)}(q,t) - 1 = A[xe^{-\frac{t}{\tau_1}} + (1-x)e^{-\frac{t}{\tau_2}}]^2 .....[2]$$

where, τ_1 and τ_2 are time scales that characterize a fast and slow relaxation process, respectively; 'x' is the contribution of the fast relaxation process to the correlation decay and *A* is an instrumental constant. Attempts to fit the correlation function for sample concentrations ≥ 30% w/v with a single relaxation time, or with a stretched exponential yielded poor fits (Figure 2.12). A linear combination of two simple exponentials was observed to fit our data well, and employing stretched exponentials did not significantly

improve the goodness of fit. This is in contrast to dynamic light scattering for caged systems where the slow relaxation process associated with cage reorganization is typically fitted with a stretched exponential [40]. In the present case, for concentrations ≤ 20% w/v, we set x = 1, viz. the correlation function is fitted with only one relaxation time, τ_1. Please note that τ_1 increases with sample concentration from the lowest concentration measured, up to about 50% w/v (Figure 2.11b). For concentrations above 30% w/v, the time scales for the slow and fast processes are different from each other by one to two orders of magnitude. Above a concentration of 50% w/v, τ_1 ($\approx 2 \times 10^{-4}$ s) and τ_2 ($\approx 10^{-2}$ s) are not strongly concentration dependent.

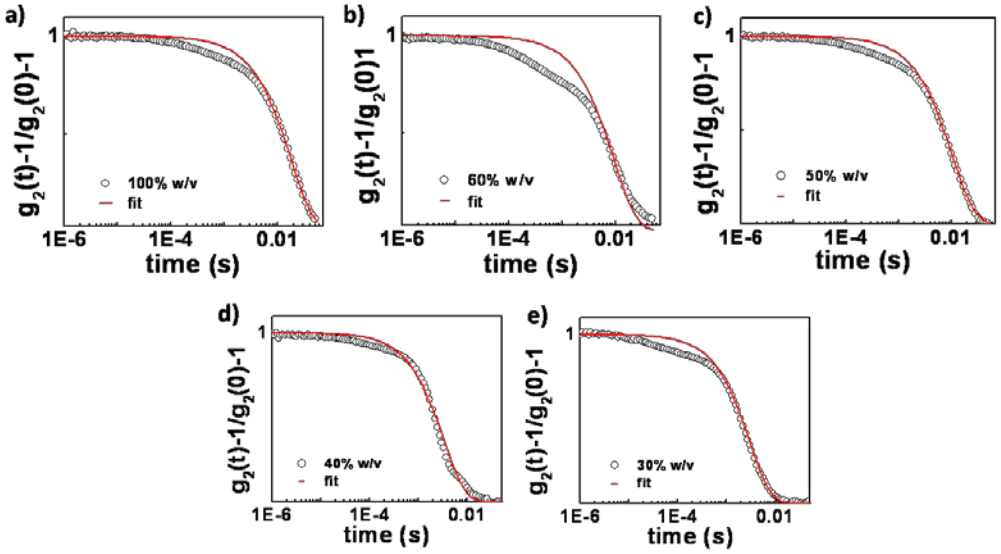

Figure 2.12: *Force fitting the DLS data of palladium octanethiolate for higher concentrations using single exponential fitting. Dynamic light scattering data of palladium octanethiolate at higher concentrations viz. 100% w/v, 60% w/v, 50% w/v, 30% w/v with just single exponential fitting yielded poor fits showing that the data demand more than just single exponential fit for better fits.*

Multi angle DLS data were recorded for Pd-octanethiolate samples at concentrations of 50%, 40%, 30%, 20% and 10% w/v (Figure 2.13) and the correlation functions, $g_{(2)}(q,t)$, were fitted using equation 2. For all concentrations, above and below 30% w/v, the fast relaxation time, τ_1, scales with q^{-2} (Figure 2.11c). Literature reports [40-42] indicate that

hydrodynamic undulation modes observed in DLS from dilute lamellar systems show relaxation times that scale with q^{-2}. It is plausible that the fast relaxation time observed in our DLS experiments arises from such hydrodynamic undulation modes of sheet-like Pd-octanethiolate structures. Please note that τ_1 is strongly concentration dependent below 30% w/v, suggesting that even at these low concentrations, weak sheet-sheet interactions influence the single sheet undulation modes. τ_1 is approximately constant for higher concentrations between 50 and 100% w/v, suggesting that the undulation modes persist at higher concentrations. The contribution of these undulation modes, x, is in the range 0.01 to 0.08 at Pd-thiolate concentrations above 30% w/v (Table 2.14). The slow time scale, τ_2, was interpreted as resulting from the cooperative relaxation of the associated Pd-octanethiolate sheets. The q^{-2} scaling is not observed to hold for τ_2, the slow relaxation time.

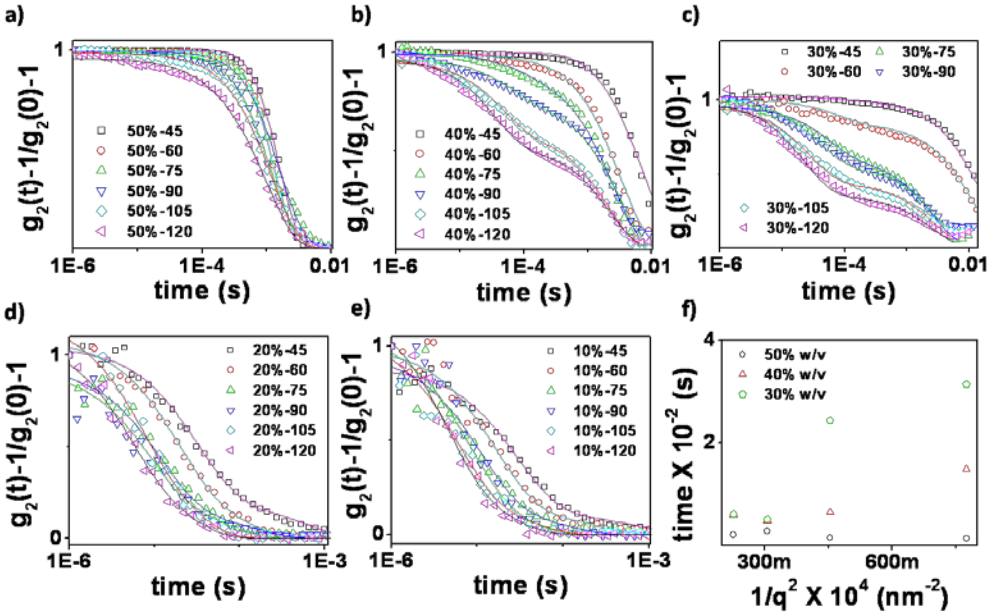

Figure 2.13: *Multi-angle DLS of palladium octanethiolate from 50% w/v to 10% w/v. Multi angle DLS of palladium octanethiolate at a) 50% w/v, b) 40% w/v, c) 30% w/v, d) 20% w/v and e) 10% w/v between (angle between the auto-correlator and the detector) 45 degrees to 120 degree angles. f) Slow relaxation time scales from multi angle DLS of palladium octanethiolate sample at different concentrations 50% w/v, 40% w/v, 30% w/v plotted as a function of $1/q^2$ do not show linear dependence.*

Concentration (% w/v)	Fast relaxation time (τ_1) (sec)	Slow relaxation time (τ_2) (sec)	x (contribution of τ_1 to the correlation decay)
100	1.8779×10^{-4}	3.89×10^{-2}	0.034
60	1.8774×10^{-4}	2.39×10^{-2}	0.083
50	1.04×10^{-4}	2.24×10^{-2}	0.032
40	4.56×10^{-5}	6.63×10^{-3}	0.015
30	2.19×10^{-5}	6.18×10^{-3}	0.043
20	1.71×10^{-5}	--	1
10	1.38×10^{-5}	--	1
5	1.23×10^{-5}	--	1
1.67	9.17×10^{-6}	--	1

Table 2.14: *DLS relaxation time scales. Relaxation times from dynamic light scattering of palladium octanethiolate and contribution of fast relaxation time to the correlation decay.*

Static light scattering on toluene solutions of Pd-octanethiolate (Figure 2.15) are in qualitative accord with DLS data, indicating a structural transition at a concentration

around 30% w/v. At concentrations ≤20% (w/v), the scattered intensity of the Pd - octanethiolate is approximately q-independent over a q-range 0.01 to 0.07 nm^{-1}. At concentrations ≥30% w/v, there is a qualitative change in the q-dependence of the scattered intensity, with enhanced scattering at low q, indicating the formation of large length scale structures.

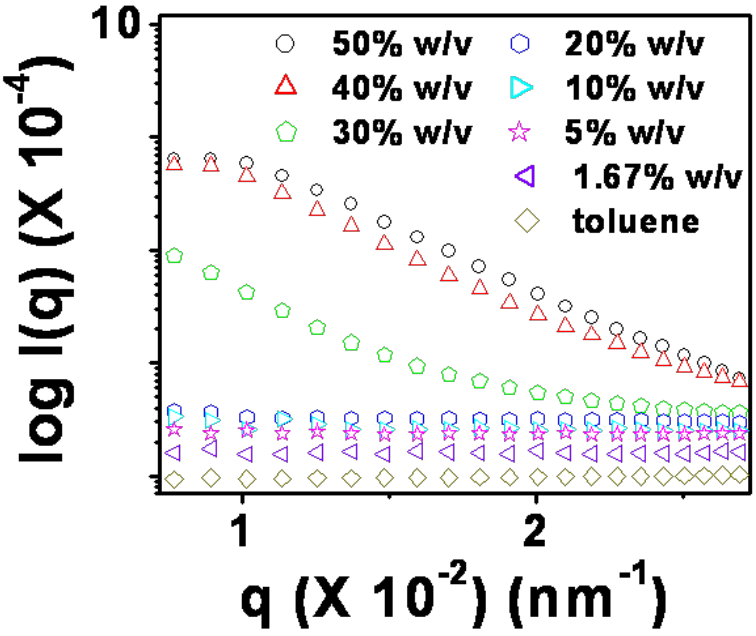

Figure 2.15: *Static light scattering data of palladium octanethiolate. Log-linear plot of the static light scattering raw-data of palladium octanethiolate in toluene at different concentrations, viz. 50% w/v, 40% w/v, 30% w/v, 20% w/v, 10% w/v, 5% w/v, 1.67% w/v and toluene.*

2.4.3. (c) Comparative light scattering studies with two model monomeric molecular systems

To rule out any ambiguity and confirm that the faster relaxation time scales are indeed due to the sheets existing in solution at the lowest possible concentration and not from the individual disintegrated molecular entities, two different monomeric molecular systems were subjected to light scattering experiments and analyzed the as obtained data was

analyzed. The two monomeric molecular systems studied were 1) Octanethiol, 2) Palladium dodecanethiolate hexamer.

Dynamic light scattering on these samples was performed in a similar fashion as was done on the palladium octanethiolate solutions. The results are shown in Figure 2.16 below. From the light scattering data on these two model monomolecular compounds it is clearly evident that the relaxation time scales for both the samples show decay times that are very low when compared to the lowest concentration sample of palladium octanethiolate. The decay times for these two samples are less than at least an order of magnitude to that of the palladium octanethiolate. Thus it is clear that the 1.67 wt% palladium octanethiolate sample still retains sheet like structures and not disintegrated into monomolecular units.

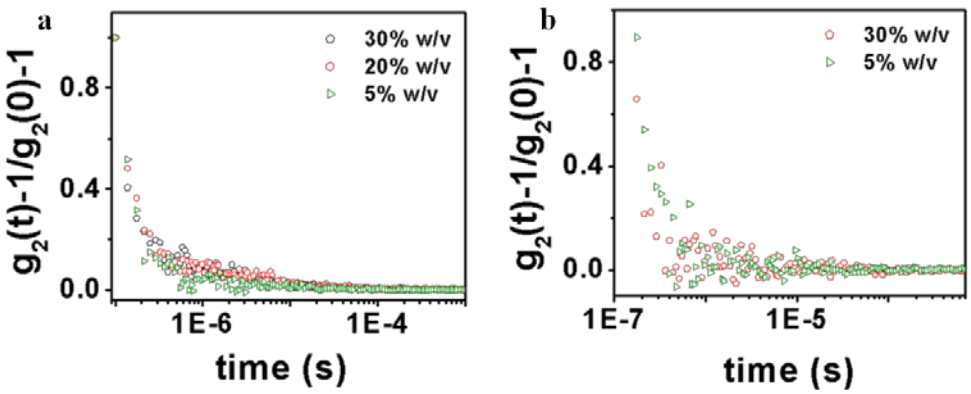

Figure 2.16: *a). Dynamic light scattering data for the palladium dodecanethiolate hexamer at different concentrations. b) Dynamic light scattering data for octanethiol at 30% w/v and 5% w/v concentrations.*

2.4.3. (d) Solution state FTIR

To probe the molecular implications of the changes in τ_1 and τ_2 on dilution, and to understand the emergence of lamellar order in Pd-octanethiolate, we used solution state FTIR to interrogate changes in the C-H stretching progressions of the CH_3 end group of the octanethiol moiety. Analysis of data obtained for dilution with toluene is complicated due to interference from toluene vibrations. Therefore, Pd-octanethiolate was serially

diluted using CCl_4. In the Figure 2.17a the solution state FTIR spectra of palladium octanethiolate at various concentrations in CCl_4 were presented after normalization with respect to intensity at 3027.3 cm^{-1}. Qualitatively similar data were obtained for dilution with toluene (Figure 2.19). We observe a gradual decrease in the relative intensity of the stretching bands on serial dilution of the sample with CCl_4. The ratio of the intensities of the C-H symmetric stretching band (at 2852 cm^{-1}) to the C-H anti-symmetric stretching band (at 2922 cm^{-1}) of the C-H stretching progressions of the end CH_3 group, systematically increases with Pd-octanethiolate concentration (Figure 2.17b). In accordance with literature reports [43], our data suggest that on increasing sample dilution, there is a decrease in the intermolecular interactions between the alkyl chains and enhanced conformational disorder due to an increased number of gauche conformers (g+, g-) with respect to the trans (t+, t-) conformers. Our data also reveals that the increase in I(2852 cm^{-1}) / I(2920 cm^{-1}) with concentration is steeper as the concentration increases to 30% w/v, and shows a more gradual increase from 30% w/v to 500% w/v. This change in slope around the concentration of 30% w/v is also observed for the rocking band at 725 cm^{-1} (Figure 2.19).

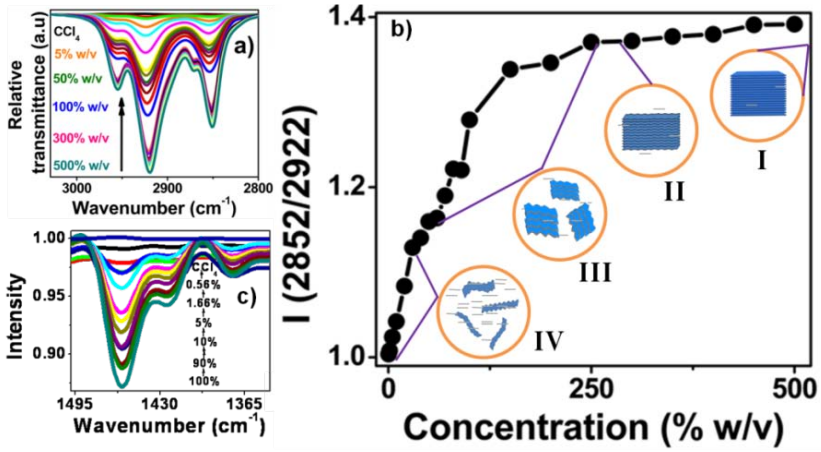

Figure 2.17: *a) Solution state FTIR plot highlighting the C-H stretching progressions of the end CH_3 for different concentrations of the sample in CCl_4. b) The corresponding graph for ratio of the C-H symmetric to anti-symmetric stretching bands of the end CH_3. c) Solution state FTIR plot highlighting the CH_3 umbrella deformation bands. The encircled portions (I), (II), (III) and (IV) are cartoon representations of the events.*

Moreover, other prominent IR bands corresponding to CH_2 scissoring at 1438 cm^{-1} and umbrella motions of CH_3 at 1365 cm^{-1} follow the same trend as the C-H stretching progressions of the end CH_3 group (Figure 2.18).

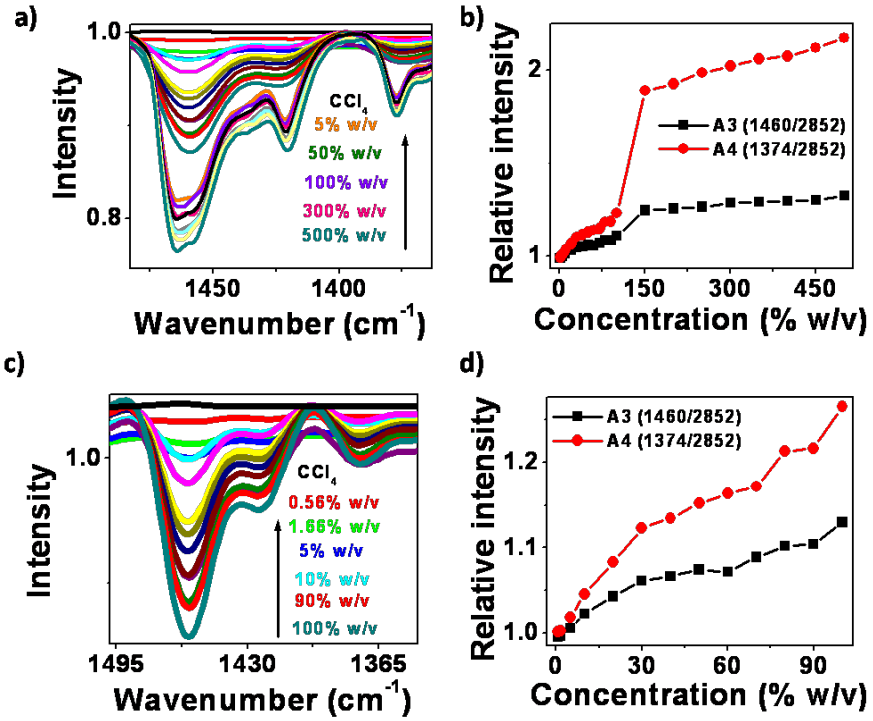

Figure 2.18: *FTIR of palladium octanethiolate umbrella and scissoring modes of end CH_3 group. a) Solution state FTIR spectra for palladium octanethiolate in CCl_4 highlighting CH_2 scissoring and CH_3 umbrella deformation bands around 1460 cm^{-1} and 1374 cm^{-1} respectively from 500 % w/v to 0.56 % w/v. b) Plot for the ratios of scissoring and umbrella progressions to the C-H symmetric stretching progressions of the end CH_3 group following the similar trend as that of the C-H stretching progressions. c) Solution state FTIR spectra for palladium octanethiolate in CCl_4 highlighting the CH_2 scissoring and CH_3umbrella deformation bands around 1460 cm^{-1} and 1374 cm^{-1} respectively from 100% w/v to 0.56% w/v and d) the corresponding graph for clarity from b).*

The FTIR for determining the rocking progressions were performed in dry toluene itself (note that, toluene was the actual solvent in which all the other characterizations were done) since at 725 cm^{-1}, there could be no interference from the toluene bands on the palladium octanethiolate bands. The head band of the rocking progressions at 725 cm^{-1} increases in intensity as the sample gets diluted (Figure 2.19), in contrast to the decrease in intensity observed for the C-H stretching bands. This is consistent with the proposed reduction in the inter chain attractive interactions on diluting with solvent.

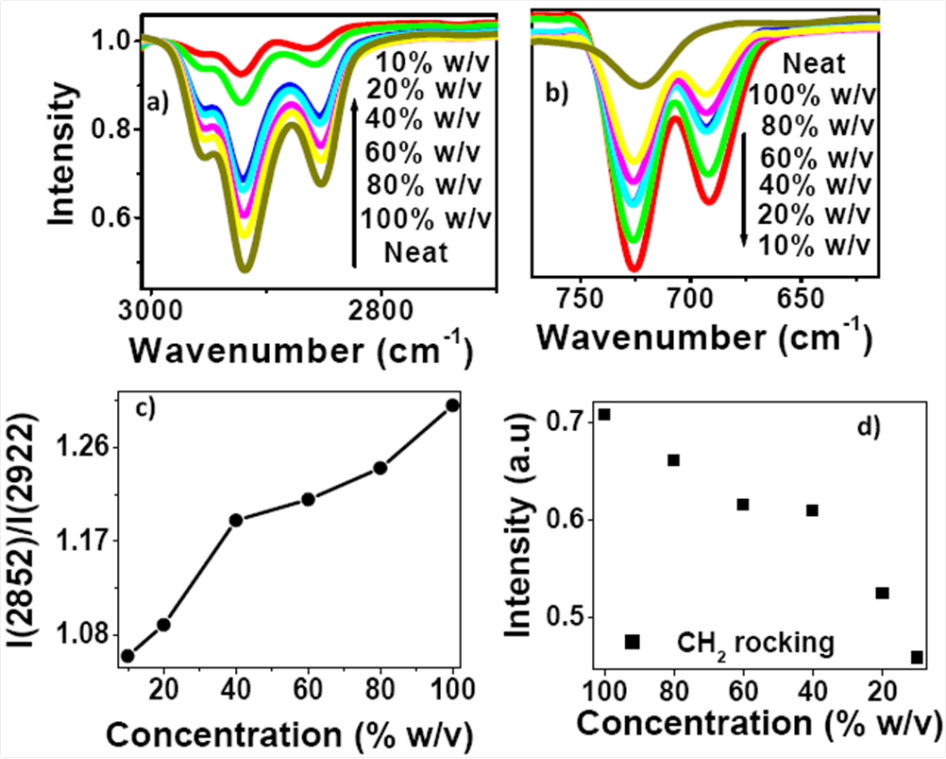

Figure 2.19: *FTIR of palladium octanethiolate in toluene. Solution state FTIR of palladium octanethiolate samples with dry toluene as the solvent. a) C-H stretching progressions of the end CH_3 group in the thiolate. b) Rocking progressions of the CH_2 groups in the thiolate.* ***c)*** *The ratio of the C-H symmetric to anti-symmetric stretching bands of the end CH_3. d) Plot of rocking progressions from 100 % w/v to 10 % w/v versus concentration.*

As the closely packed alkyl chains move away from each other on higher dilutions, the CH_2 groups become free and disengaged with the adjacent alkyl chains. This enhances

the CH_2 rocking progressions. On the other hand, closely packed alkyl chains are necessary to intensify the C-H stretching bands. Thus giving rise to the contrast in intensities of the stretching and rocking progressions.

2.4.3. (e) TEM of palladium octanethiolate

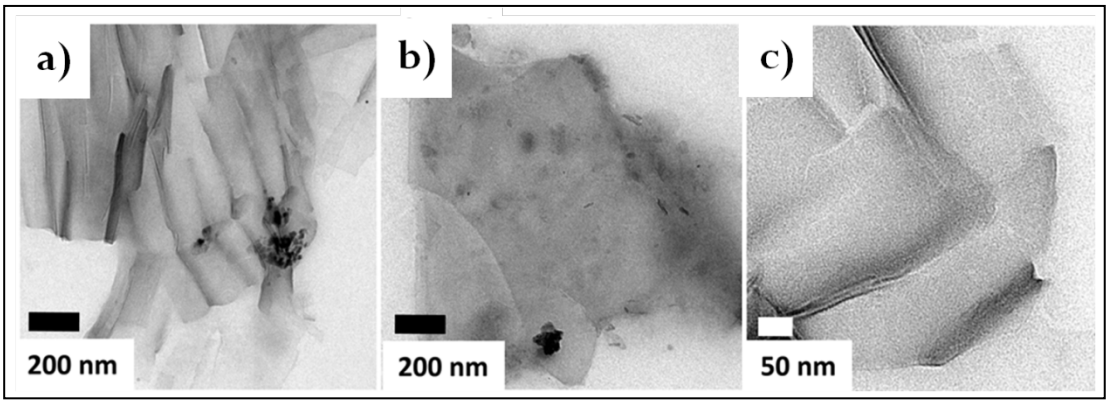

Figure 2.20: *TEM of palladium octanethiolate at 1.67 wt% concentration. Electron microscopy on the lowest concentrated sample of palladium octanethiolate at 1.67 wt% in toluene drop casted onto a carbon coated copper TEM grid. Just one drop of the solution was coated onto the grid and the grid was then air dried at room temperature.*

Electron microscopy on palladium octanethiolate was performed at its diluted concentration of 1.67 wt%. Several concentrations of palladium octanethiolate solutions were prepared in toluene for experimentation with the TEM. The attempted concentrations for electron microscopy were 20 wt%, 10 wt%, 5 wt% and 2.5 wt%. However, samples prepared at higher concentrations did not allow electrons to pass through them thus not resulting in any image under the transmission electron microscopy. Plausible deduction from these failed experiments lead to a conclusion that the samples might have existed as well spread out thick layers on the grid.

But at 1.67 wt% concentration ultrathin nanosheets of palladium octanethiolate indeed could be observed (Figure 2.20). These palladium octanethiolate nanosheets extended laterally up to hundreds of nanometer length scales or up to even micrometer length scales. In the Figure 2.20c it could be noticed that the palladium octanethiolate nanosheet

exists as single layered. Thus at some places in the TEM grid single layers of palladium octanethiolate could be observed. If careful optimization of coating the palladium octanethiolate single layers on any suitable substrate is realized, then it could have many implications for the ensuing research on metal based single layers for technological applications.

2.4.3. (f) Summary of the techniques used for the solution structure determination of palladium octanethiolate

Schematic summary of the techniques used for the solution structure determination of palladium octanethiolate could be depicted as in Figure 2.21 shown below.

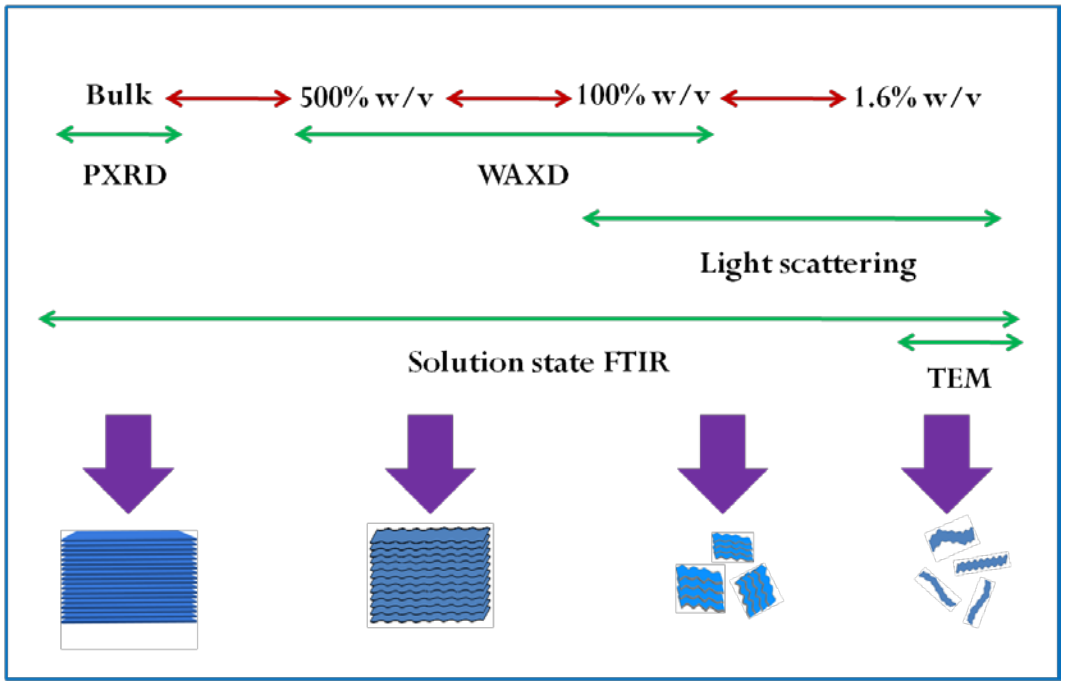

Figure 2.21: *Schematic summary of the deductions from various solution state techniques employed for structural evaluation.*

The Figure 2.21 above depicts a clear overview of the solution state instrumental techniques employed to determine the course of delamination of the palladium octanethiolate when dissolved in non-polar organic solvents. As represented in the schematic, the bulk solid palladium octanethiolate is characterized by a strict registry of

lamellar sheets. The WAXD characterization performed on the 500 wt% up to 100 wt% samples provided evidence for initiation of losing lamellar registry in the samples at lesser concentrations viz. at 100 wt%. From 100 wt% to 1.67 wt% light scattering yielded strong proofs of transitioning of the lamellae from stack-stack interactions to undulating individual nanosheets. The individual nanosheets at 1.67 wt% were imaged through electron microscopy. Solution state FTIR was performed over all the samples from bulk to 1.67 wt% offering an overall perspective on the delamination process of palladium octanethiolate.

2.4.3. (g) Solution structure of other metal octanethiolates

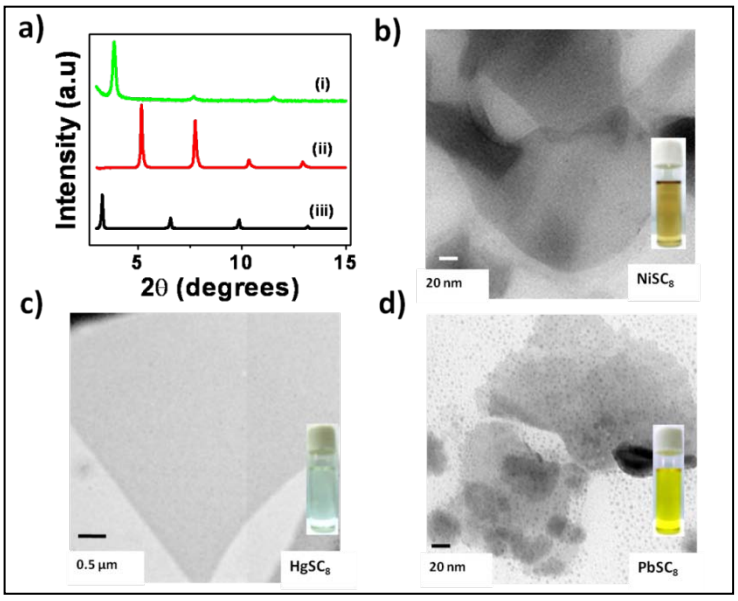

Figure 2.22: *(a) PXRD plots of (i) nickel octanethiolate, (ii) mercury octanethiolate, and (iii) lead octanethiolate; and TEM images of (b) nickel octanethiolate, (c) mercury octanethiolate, and (d) lead octanethioalte. Insets of parts b, c, and d, are photographs of the clear solutions of nickel octanethiolate, mercury octanethiolate, and lead octanethiolate, respectively, in chloroform.*

Octanethiolates of other metal ions primarily nickel, lead and mercury were also synthesized as defined in the section 2.3. Quite gratifyingly, these also were found to be highly soluble in non-polar organic solvents as evident from the inset glass tube pictures in the Figure 2.22 above. No rigorous scattering experiments were executed on these

other metal octanethiolates. Nonetheless, electron microscopy on the most dilute samples of these thiolates revealed ultrathin nanosheets. Figure 2.22a shows powder XRD patterns of these metal octanethiolates drop casted and dried on silicate glass demonstrating lamellar order in all these thiolates. Figures 2.22b-d display the TEM images of these metal thiolates at their lowest concentrations. The lowest concentrations differed for each of the octanethiolate. For nickel octanethiolate it was 0.23 wt%, for lead octanethiolate it was 0.1 wt% and for the mercury octanethiolate it was 2.5 wt%.

2.4.3. (h) Solution structure of palladium dodecanethiolate

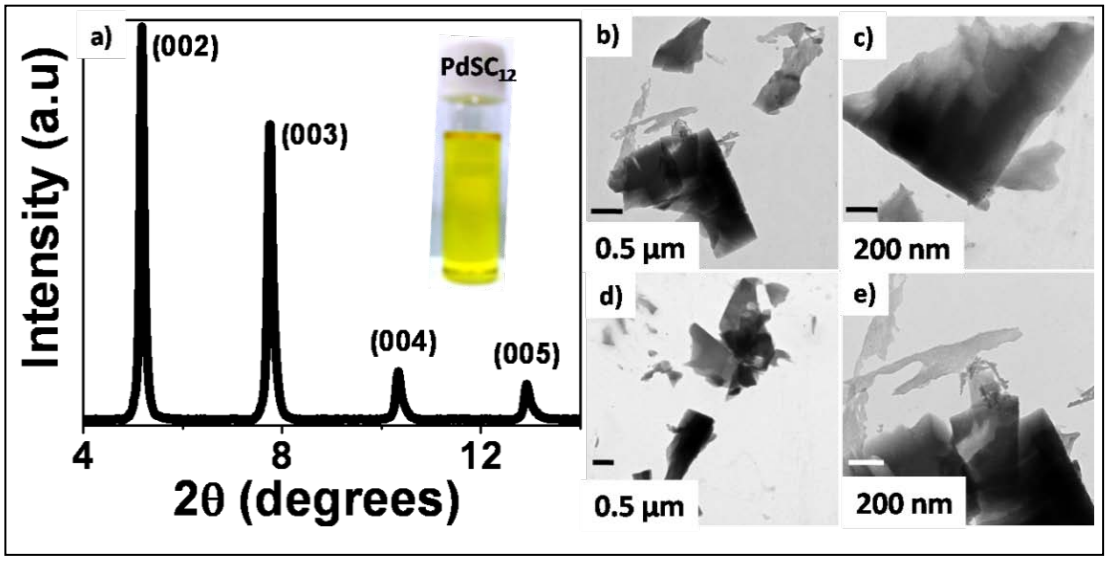

***Figure 2.23**: Palladium dodecanethiolate. **a)** PXRD of palladium dodecanethiolate showing the lamellar structure. **(b-e)** Representative TEM images of palladium dodecanethiolate.*

To show that not just octanethiolates but other thiolates could also be solubilized in non-polar organic solvents, dodecanethiol was employed as the ligand and it was reacted with palladium acetate as described in section 2.3. The formation and existence of the palladium dodecanethiolate was confirmed through powder XRD, as indicated by the (*00l*) lamellar reflections (Figure 2.23a). The solubility of palladium dodecanethiolate in

non-polar solvents such as toluene or chloroform is again confirmed by the formation of clear solution on adding non-polar solvents to the neat sample. Figures 2.23b-e illustrate ultrathin nanosheets from the electron microscopy results on the diluted sample of palladium dodecanethiolate. The dilution was at 1.67 wt% as in the case of the palladium octanethiolate.

2.4 Conclusions

In this chapter, step-by-step delamination of the novel two dimensional materials, namely, metal thiolates was studied in great detail using palladium octanethiolate as the model system. A variety of instrumentation techniques viz. light scattering, x-ray diffraction (powder XRD and wide angle XRD), solution state FTIR, electron microscopy were employed to thoroughly understand the exfoliation process of the palladium octanethiolate lamellae into ultrathin single sheets at high dilutions in an organic solvent such as toluene. Clear monitoring of the exfoliation process was done through dynamic light scattering. Wide angle XRD was utilized to characterize the higher concentration samples' diffracting behavior. Solution state FTIR data acted as a connecting link between the two data sets obtained from light scattering and WAXD. Electron microscopy was finally used as a tool to image the ultrathin palladium octanethiolate layers on a TEM grid. This was extended to other palladium thiolates such as palladium dodecanethiolate and also to other metal thiolates such as nickel octanethiolate, lead octanethiolate and mercuric octanethiolate. The comprehensive study of the solution state structures of the metal thiolates performed here comprises an important piece of work and entices further work in this area of solution state nanosheet dynamics in the backdrop of growing interest in two dimensional layered materials.

2.5 References

[1]. Dance, I. G.; Fisher, K. J.; Banda, R. M. H.; Scudder, M. L., Layered structure of crystalline compounds AgSR. *Inorg. Chem.* **1991,** 30, 183.

[2]. Hu, L.; de la Rama, L. P.; Efremov, M. Y.; Anahory, Y.; Schiettekatte, F.; Allen, L. H., Synthesis and characterization of single-layer silver-decanethiolate lamellar crystals. *J. Am. Chem. Soc.* **2011,** 133, 4367.

[3]. Sandhyarani, N.; Pradeep, T., An investigation of the structure and properties of layered copper thiolates. *J. Mater. Chem.* **2001,** 11, 1294.

[4]. Thomas, P. J.; Lavanya, A.; Sabareesh, S.; Kulkarni, G. U., Self-assembling bilayers of palladiumthiolates in organic media. *Proc. Indian Acad. Sci. (Chem. Sci.).* **2001,** 113, 611.

[5]. Shaw, R. A.; Woods, M., Preparation and some properties of lead thiolates. *J. Chem. Soc. A* **1971**, 1569.

[6]. Pokroy, B.; Aichmayer, B.; Schenk, A. S.; Haimov, B.; Kang, S. H.; Fratzl, P.; Aizenberg, J., Sonication-assisted synthesis of large, high-quality mercury thiolate single crystals directly from liquid mercury. *J. Am. Chem. Soc.* **2010,** 132, 14355.

[7]. Wertheim, E., Derivatives for the identification of mercaptans. *J. Am. Chem. Soc* **1929,** 51, 3661.

[8]. Bhuvana, T.; Gregoratti, L.; Heun, S.; Dalmiglio, M.; Kulkarni, G. U., Electron resist behavior of Pd hexadecanethiolate examined using X-ray photoelectron spectroscopy with nanometric lateral resolution. *Langmuir* **2009,** 25, 1259.

[9]. Bhuvana, T.; Boley, W.; Radha, B.; Dolash, B. D.; Chiu, G.; Bergstrom, D.; Reifenberger, R.; Fisher, T. S.; Kulkarni, G. U., Inkjet printing of palladium alkanethiolates for facile fabrication of metal interconnects and surface-enhanced Raman scattering substrates. *Micro & Nano Lett.* **2010,** 5, 296.

[10]. Bhuvana, T.; Kulkarni, G. U., A SERS-active nanocrystalline Pd substrate and its nanopatterning leading to biochip fabrication. *Small* **2008,** 4, 670.

[11]. Larsen, T. H.; Sigman, M.; Ghezelbash, A.; Doty, R. C.; Korgel, B. A., Solventless synthesis of copper sulfide nanorods by thermolysis of a single source thiolate-derived precursor. *J. Am. Chem. Soc.* **2003,** 125, 5638.

[12]. Geim, A. K.; Grigorieva, I. V., Van der Waals heterostructures. *Nature* **2013,** 499, 419.

[13]. Georgiou, T.; Jalil, R.; Belle, B. D.; Britnell, L.; Gorbachev, R. V.; Morozov, S. V.; Kim, Y. J.; Gholinia, A.; Haigh, S. J.; Makarovsky, O.; Eaves, L.; Ponomarenko, L. A.;

Geim, A. K.; Novoselov, K. S.; Mishchenko, A., Vertical field-effect transistor based on graphene– WS_2 heterostructures for flexible and transparent electronics. *Nat. Nanotechnol.* **2013,** 8, 100.

[14]. Lee, C.-H.; Lee, G.-H.; van der Zande, A. M.; Chen, W.; Li, Y.; Han, M.; Cui, X.; Arefe, G.; Nuckolls, C.; Heinz, T. F.; Guo, J.; Hone, J.; Kim, P., Atomically thin p-n junctions with van der Waals heterointerfaces. *Nat. Nanotechnol.* **2014,** 9, 676.

[15]. Woods, C. R.; Britnell, L.; Eckmann, A.; Ma, R. S.; Lu, J. C.; Guo, H. M.; Lin, X.; Yu, G. L.; Cao, Y.; Gorbachev, R. V.; Kretinin, A. V.; Park, J.; Ponomarenko, L. A.; Katsnelson, M. I.; Gornostyrev, Y. N.; Watanabe, K.; Taniguchi, T.; Casiraghi, C.; Gao, H. J.; Geim, A. K.; Novoselov, K. S., Commensurate-incommensurate transition in graphene on hexagonal boron nitride. *Nat. Phys.* **2010,** 10, 451.

[16]. Andersen, K.; Latini, S.; Thygesen, K. S., Dielectric genome of van der Waals heterostructures. *Nano Lett.* **2015,** 15, 4616.

[17]. Azizi, A.; Eichfeld, S.; Geschwind, G.; Zhang, K.; Jiang, B.; Mukherjee, D.; Hossain, L.; Piasecki, A. F.; Kabius, B.; Robinson, J. A.; Alem, N., Freestanding van der Waals heterostructures of graphene and transition metal dichalcogenides. *ACS Nano* **2015,** 9, 4882.

[18]. Zheng, Z.; Zhang, X.; Neumann, C.; Emmrich, D.; Winter, A.; Vieker, H.; Liu, W.; Lensen, M.; Golzhauser, A.; Turchanin, A., Hybrid van der Waals heterostructures of zero-dimensional and two-dimensional materials. *Nanoscale* **2015,** 7, 13393.

[19]. Wang, B.; Eichfield, S. M.; Wang, D.; Robinson, J. A.; Haque, M. A., In situ degradation studies of two-dimensional WSe_2-graphene heterostructures. *Nanoscale* **2015,** 7, 14489.

[20]. Xu, X.; Yao, W.; Xiao, D.; Heinz, T. F., Spin and pseudospins in layered transition metal dichalcogenides. *Nat. Phys.* **2014,** 10, 343.

[21]. Fang, H.; Battaglia, C.; Carraro, C.; Nemsak, S.; Ozdol, B.; Kang, J. S.; Bechtel, H. A.; Desai, S. B.; Kronast, F.; Unal, A. A.; Conti, G.; Conlon, C.; Palsson, G. K.; Martin, M. C.; Minor, A. M.; Fadley, C. S.; Yablonovitch, E.; Maboudian, R.; Javey, A., Strong interlayer coupling in van der Waals heterostructures built from single-layer chalcogenides. *Proc. Nat. Acad. Sci. U.S.A.* **2014,** 111, 6198.

[22]. Hong, X.; Kim, J.; Shi, S.-F.; Zhang, Y.; Jin, C.; Sun, Y.; Tongay, S.; Wu, J.; Zhang, Y.; Wang, F., Ultrafast charge transfer in atomically thin MoS_2/WS_2 heterostructures. *Nat. Nanotechnol.* **2014,** 9, 682.

[23]. Li, X.; Basile, L.; Huang, B.; Ma, C.; Lee, J.; Vlassiouk, I. V.; Puretzky, A. A.; Lin, M.-W.; Yoon, M.; Chi, M.; Idrobo, J. C.; Rouleau, C. M.; Sumpter, B. G.; Geohegan, D. B.; Xiao, K., Van der Waals epitaxial growth of two-dimensional single-crystalline GaSe domains on graphene. *ACS Nano* **2015,** 9, 8078.

[24]. Geim, A. K.; Grigorieva, I. V., Van der Waals heterostructures. *Nature* **2013,** 499, 419.

[25]. Gong, Y.; Lin, J.; Wang, X.; Shi, G.; Lei, S.; Lin, Z.; Zou, X.; Ye, G.; Vajtai, R.; Yakobson, B. I.; Terrones, H.; Terrones, M.; Tay, BengÂ K.; Lou, J.; Pantelides, S. T.; Liu, Z.; Zhou, W.; Ajayan, P. M., Vertical and in-plane heterostructures from WS_2/MoS_2 monolayers. *Nat. Mater.* **2014,** 13, 1135.

[26]. John, N. S.; Thomas, P. J.; Kulkarni, G. U., Self-assembled hybrid bilayers of palladium alkanethiolates. *J. Phys. Chem. B* **2003,** 107, 11376.

[27]. Israelachvili, J. N., Chapter 3 - Strong intermolecular forces: covalent and coulomb interactions. In *Intermolecular and Surface Forces (Third Edition)*, Academic Press: Boston, **2011,** 53.

[28]. Israelachvili, J. N., 6 - Van der Waals forces. In *Intermolecular and Surface Forces (Third Edition)*, Academic Press: Boston, **2011,** 107.

[29]. Israelachvili, J. N., 8 - Special interactions: hydrogen-bonding and hydrophobic and hydrophilic interactions. In *Intermolecular and Surface Forces (Third Edition)*, Academic Press: Boston, **2011,** 151.

[30]. Israelachvili, J. N., 10 - Unifying concepts in intermolecular and interparticle forces. In *Intermolecular and Surface Forces (Third Edition)*, Academic Press: Boston, **2011,** 191.

[31]. Rosemary, M. J.; Pradeep, T., Solvothermal synthesis of silver nanoparticles from thiolates. *J. Colloid Interface Sci.* **2003,** 268, 81.

[32]. Yang, Z.; Smetana, A. B.; Sorensen, C. M.; Klabunde, K. J., Synthesis and characterization of a new tiara Pd(II) thiolate complex, $[Pd(SC_{12}H_{25})_2]_6$, and Its solution-phase thermolysis to prepare nearly monodisperse palladium sulfide nanoparticles. *Inorg. Chem.* **2007,** 46, 2427.

[33]. Gururajan, G.; Ogale, A. A., Real-time crystalline orientation measurements during low-density polyethylene blown film extrusion using wide-angle X-ray diffraction. *Polymer Engg. & Sci.* **2012,** 52, 1532.

[34]. Lin, M.-C.; Wang, Y.-C.; Chen, H.-L.; Muller, A. J.; Su, C.-J.; Jeng, U. S., Critical analysis of the crystal orientation behavior in polyethylene-based crystalline-amorphous diblock copolymer. *J. Phys. Chem. B.* **2011,** 115, 2494.

[35]. Chen, Z.; Liu, Y.; Yao, C.; Yang, G., Crystallization behavior and morphology of double crystalline poly(trimethylene terephthalate)/poly(ethylene oxide terephthalate) copolymers. *Polymer Intl.* **2013,** 62, 219.

[36]. Liu, C.-L.; Lin, M.-C.; Chen, H.-L.; Muller, A. J., Evolution of crystal orientation in one-dimensionally confined space templated by lamellae-forming block copolymers. *Macromolecules* **2015,** 48, 4451.

[37]. Dong, X.-H.; Van Horn, R.; Chen, Z.; Ni, B.; Yu, X.; Wurm, A.; Schick, C.; Lotz, B.; Zhang, W.-B.; Cheng, S. Z. D., Exactly defined half-stemmed polymer lamellar crystals with precisely controlled defects' locations. *J. Phys. Chem. Lett.* **2013,** 4, 2356.

[38]. Lin, M.-C.; Wang, Y.-C.; Chen, J.-H.; Chen, H.-L.; Muller, A. J.; Su, C.-J.; Jeng, U. S., Orthogonal crystal orientation in double-crystalline block copolymer. *Macromolecules* **2011,** 44, 6875.

[39]. Sasaki, T.; Watanabe, M., Osmotic swelling to exfoliation. exceptionally high degrees of hydration of a layered titanate. *J. Am. Chem. Soc.* **1998,** 120, 4682.

[40]. Nallet, F.; Roux, D.; Prost, J., Dynamic light scattering study of dilute lamellar phases. *Phys. Rev. Lett.* **1989,** 62, 276.

[41]. Lipowsky, R.; Leibler, S., Unbinding transitions of interacting membranes. *Phys. Rev. Lett.* **1986,** 56, 2541.

[42]. Richetti, P.; Kékicheff, P.; Parker, J. L.; Ninham, B. W., Measurement of the interactions between membranes in a stack. *Nature* **1990,** 346, 252.

[43]. Snyder, R. G.; Strauss, H. L.; Elliger, C. A., C-H stretching modes and the structure of n-alkyl chains. 1. long, disordered chains. *J. Phys. Chem.* **1982,** 86, 5145.

Chapter 3

Ultrathin sheets of metal and metal sulfides from metal thiolate molecular sheets

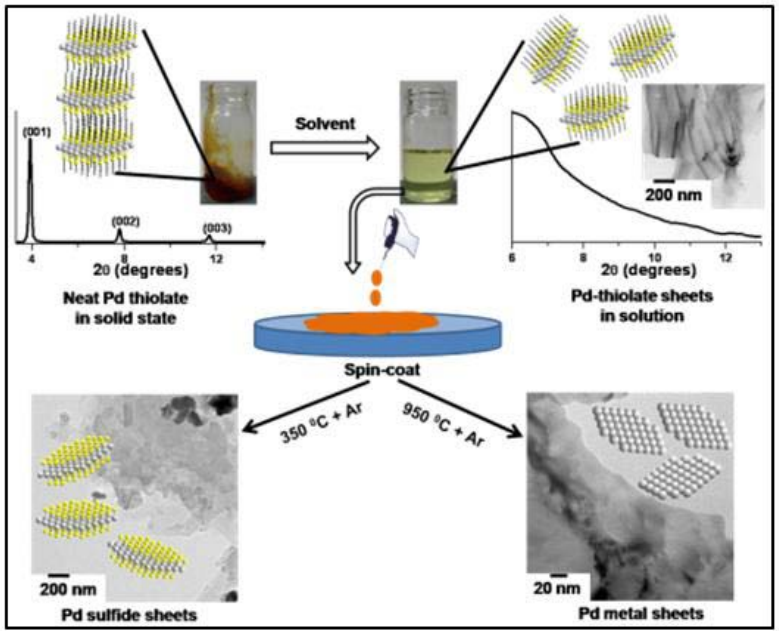

This chapter discusses preparation of ultrathin metal and metal sulfide nanosheets from metal thiolate precursors. A simple heat treatment of the soluble metal thiolate precursors coated onto quartz like substrates yielded ultrathin metal or metal sulfide sheets. Detailed magnetic property measurements were carried out on nickel sulfides which revealed unprecedented magnetization values in them. These metal/metal sulfide sheets were also found to be good electrochemical catalysts for hydrogen generation.

Parts of this work had been published in:

1) Busupalli, B.; Kummara, S.; Kumaraswamy, G.; Prasad, B. L. V., Ultrathin sheets of metal or metal sulfide from molecularly thin sheets of metal thiolates in solution. *Chem. Mater.*, **2014,** 26, 3436.

2) Busupalli, B.; Date, K. S.; Datar, S.; Prasad, B. L. V., Preparation of Ni_3S_2 and Ni_3S_2-Ni nanosheets via solution based processes. *Cryst. Growth Des.*, **2015**, 15, 2584.

3.1 Introduction

In the backdrop of renewed interest in two dimensional nanosheets following the epic discovery of graphene [1] and re-discovery of numerous other atomically or molecularly flat two dimensional materials [2-8], demand for other two dimensional nanosheets that could be technologically important emerged in a great way. This provoked the exploration of various synthetic methods for preparing many materials in nanosheet forms [9]. We realized that very few reports exist on the preparation of nanoscale thick sheets of metal/metal sulfide materials. For example, many synthetic procedures have been described to prepare the 2D sheets of metal/metal sulfides which require sophisticated deposition techniques like atomic layer deposition, chemical/physical vapor deposition and pulsed laser deposition etc. [10-13]. One of the most elegant ways of synthesizing these nanosheets is through heat treatment of their precursor compounds. Very few reports exist on realizing such metal/metal sulfide nanosheets through easy methods such as heat treating the precursor compounds [14]. In recent times, access to huge amounts of nickel sulfides that are regarded as potentially important cathode systems for the electrocatalytic hydrogen generation is becoming prominent in the hydrogen energy research arena. After finding methods that could provide access to gram scale quantities of metal thiolates and after realizing that these could act as soluble precursors, we believed that subjecting these precursor compounds to simple heat-treatment could possibly lead to the formation of metal/metal sulfide nanosheets which are otherwise very difficult to access or need sophisticated preparation techniques listed above.

One intriguing thought that could follow, if these two dimensional metal/metal sulfide nanosheets are realized, is that whether they possess multiple properties like semiconducting, magnetic and catalytic properties etc. Materials that possess such multiple properties are immensely studied by both academic researchers and industries. A few such materials exist in the literature such as dilute magnetic semiconductors (DMS), ferromagnetic semiconductors (FMS), electro/magnetochromatic materials, electro/photocatalytic materials etc. [15-25]. In this chapter the synthesis, characteristics,

properties and applications displayed by a few metal/metal sulfide nanosheets obtained from their precursor compounds through heat treatment are presented and discussed. Heat treatment was first performed on palladium octanethiolate as a test method. Then the synthetic experiments were extended to nickel thiolates. Further, a detailed study on the magnetic and semiconducting properties of the resulting nickel sulfide nanosheets was carried out. Then these nickel sulfide nanosheets were probed for their interesting energy related applications in hydrogen generation.

3.2 Preparation of M/MS nanosheets from the metal thiolate precursors

In order to find the heating conditions required for the heat treatment for the preparation of metal/metal sulfide sheets, detailed thermogravimetric analyses (TGA) of the palladium octanethiolate and nickel octanethiolate were carried out. As depicted in Figure 3.1a, palladium octanethiolate exhibited large weight loss (about 75%) around 300 ^{o}C due to the high carbon content present in the octanethiol chains. Two small kinks in the TGA spectra at lower than 300 ^{o}C were presumably due to the solvent loss from the compound. Around 800 ^{o}C, the compound still exhibited small but effective weight loss which apparently was due to the loss of sulfur content from the compound. Thus the final material left after the heat treatment could be pure palladium metal.

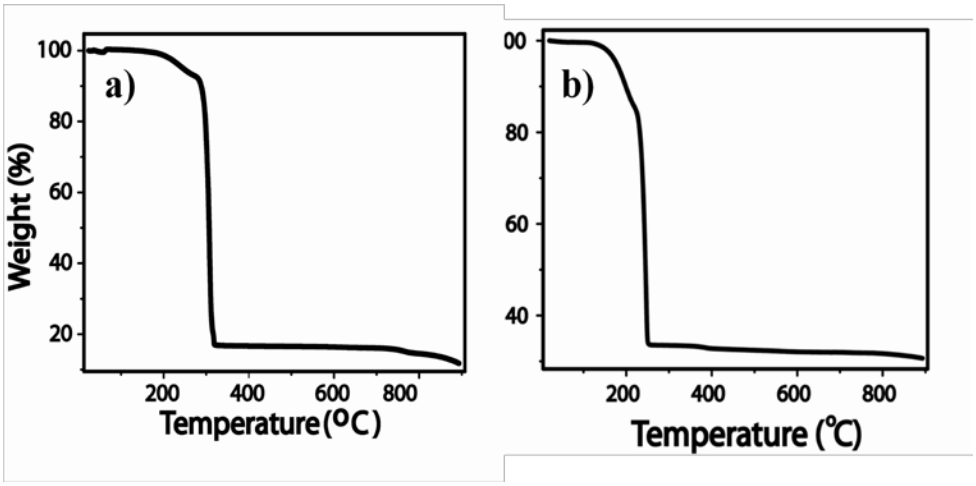

Figure 3.1*: a) Thermogravimetric analysis (TGA) of Pd-octanethiolate and b) Ni-octanethiolate.*

Nickel octanethiolate also exhibited thermal behavior in a similar fashion (Figure 3.1b). A marked decomposition around 240 ^{o}C temperature was seen due to the loss of the carbon content from the octanethiol chains in the compound. Around 700 ^{o}C temperature there is another small weight loss. This difference in the thermal behavior of nickel octanethiolate from palladium octanethiolate is probably due to lower loss of sulfur content from nickel thiolates that clearly indicated that the products that are yielded from these two metal thiolates could be different from each other.

3.2.1 Preparation of palladium sulfide nanosheets and metallic palladium nanosheets from palladium octanethiolate precursor

Based on these studies the synthetic procedure for the heat treatment conditions was devised and a basic sketch depicting the synthetic procedure for preparing palladium metal nanosheets and palladium sulfide nanosheets is presented in Figure 3.2. A thin film of the soluble palladium octanethiolate precursor in toluene solution was coated onto quartz substrates through spin coating method and the as coated quartz plates were heated at different conditions. Heating conditions executed on the palladium octanethiolate were 1) 350 ^{o}C in argon gas atmosphere that resulted in palladium sulfide nanosheets and 2) 950 ^{o}C in argon gas atmosphere resulting in pure metallic palladium nanosheets. To access large amounts of the samples, heat treatment experiments were performed on the bulk solid samples kept in ceramic boats in a tube furnace under the same conditions described above.

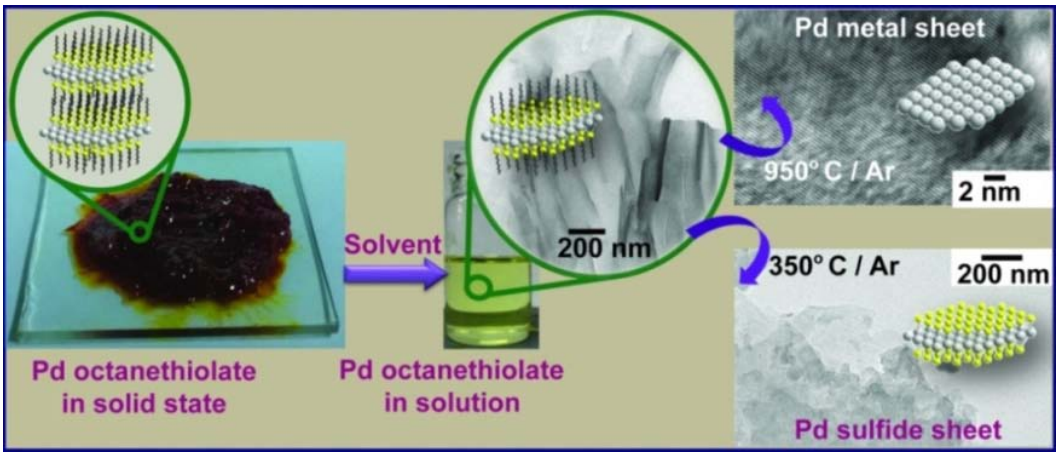

Figure 3.2: *Heat treatment of the as coated palladium octanethiolate on quartz substrates under two different conditions resulting in two different descendent nanosheets namely palladium sulfide and metallic palladium nanosheets.*

3.2.2 Preparation of nickel sulfide nanosheets from nickel octanethiolate precursor

Similar heat treatment experiments were performed on the nickel octanethiolate. These experiments resulted in two different nickel sulfide nanosheets. The conditions adopted for preparing nickel sulfide nanosheets were 1) 750 ^{o}C under argon+hydrogen atmosphere (both gases taken in 1:1 ratio) resulting in Ni_3S_2-Ni sheets and 2) 750 ^{o}C under argon atmosphere resulting in Ni_3S_2 sheets. Figure 3.3 presents these conditions in a schematic. The thermal treatment of the nickel octanethiolate was based upon the thermogravimetric analysis (TGA) experiment performed on it (Figure 3.3). Pure metallic nickel nanosheets were expected based on the previous experiment in which formation of pure metallic palladium nanosheets was observed (Figure 3.2). Unfortunately pure metallic nickel nanosheets could not be obtained under the same conditions as used for palladium thiolates. Instead only Ni_3S_2 was obtained by heating the precursor nickel octanethiolate in just argon gas atmosphere.

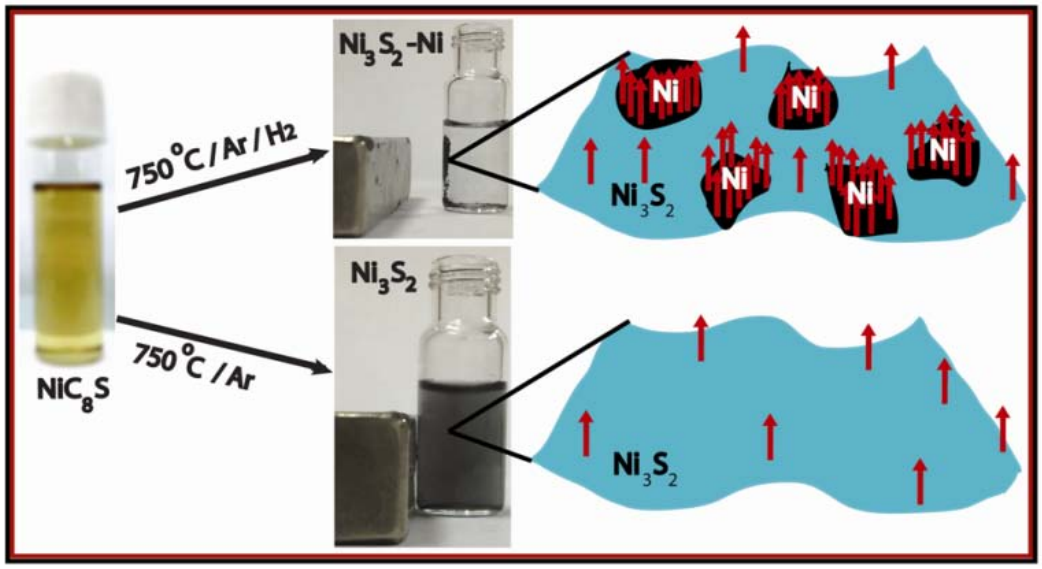

Figure 3.3: *Heat treatment of nickel octanethiolate under two different conditions resulted in two different nickel sulfides namely Ni_3S_2-Ni and Ni_3S_2. The final products were quickly checked for any visual magnetization effect and the Ni_3S_2-Ni showed instant magnetization under a bar magnet as shown above indicating a robust saturation magnetization in this system (thoroughly dealt in this chapter in the later part).*

This prompted us to use reducing hydrogen gas atmosphere in combination with argon gas expecting pure metallic Ni phase nanosheets. The heating was even carried out through varied heating conditions such as heat treating the nickel octanethiolate at elevated temperatures of about 950 ^{o}C-1000 ^{o}C under Ar+H_2 flow.

But these experiments again did not result in metallic nickel. But, quite gratifyingly Ni_3S_2-Ni composite was achieved, which is more important because it is a combination of metal and semiconductor which has implications for energy related research such as electrochemical fuel production due to the electronic interactions between metallic nickel and the semiconducting Ni_3S_2 component that could help turn the material into a more efficient catalyst.

3.3 Results and Discussion

3.3.1 Characterization of the metal and metal sulfide nanosheets

3.3.1.1 Characterization of palladium sulfide nanosheets

The resulting nanosheets were thoroughly characterized using powder XRD and electron microscopy to reveal the layered sheet like nature of the palladium sulfide, metallic palladium, Ni_3S_2 and Ni_3S_2-Ni. Powder XRD pattern for the palladium sulfide nanosheets is comparable to that existing in the literature according to the JCPDS card no. 25-1234 (Figure 3.4a). Figure 3.4b indicates the atomic percentages of the palladium and sulfur in the palladium sulfide nanosheets which confirms the stoichiometry of the sample as PdS. The presence of high amount of carbon is attributed to the carbon film on the TEM grid. Electron microscopic imaging revealed sheet like nature of the palladium sulfide nanosheets (Figure 3.4c), that these sheets consist of palladium sulfide was confirmed by the lattice fringes and electron diffraction displayed in Figure 3.4d and Figure 3.4e respectively.

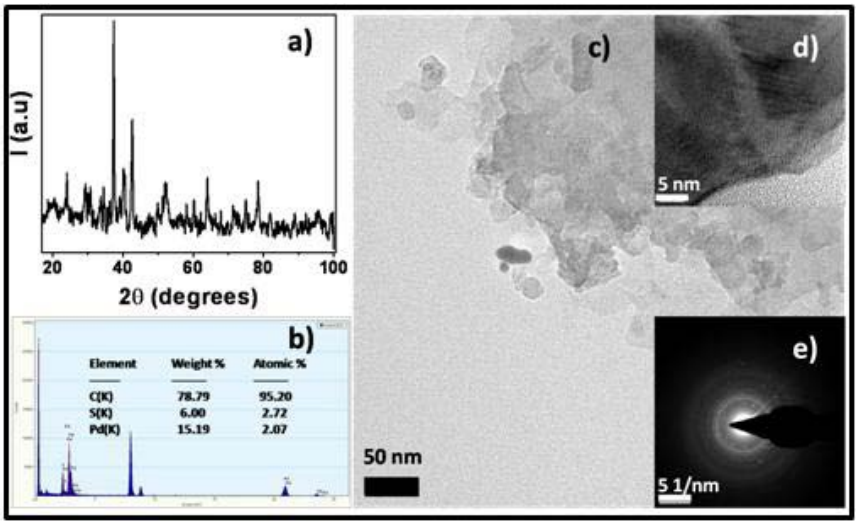

Figure 3.4: a) *PXRD pattern of PdS sheets (comparable to JCPDS card no. 25-1234);* ***b)*** *EDAX analysis of PdS sheets, notice that the atomic percentage of sulfur peak is almost as much as palladium peak.* ***c)*** *HRTEM image of PdS (insets-****(d)*** *shows enlarged HRTEM image revealing the lattice fringes corresponding to PdS sheets and* ***(e)*** *shows FFT view for these PdS sheets).*

3.3.1.2 Characterization of metallic palladium nanosheets

Similar characterizations were performed on the palladium metallic nanosheets and the data are presented in Figure 3.5. The presence of metallic palladium was confirmed by comparing the PXRD data of the heat treated material with the existing literature JCPDS card no. 05-0681. (111) and (222) peaks evident from the PXRD plot indicate sheet like orientation of the palladium metal (Figure 3.5a). Furthermore, the HRTEM image revealed lattice fringes that correspond to the (111) planes (Figure 3.5b) of Pd(0). The low magnification TEM image revealed a sheet like morphology with lateral dimensions of several micrometers (inset of Figure 3.5b).

Clearly, these Pd(0) films are sufficiently thin to allow transmission of electrons through them. The selected area electron diffraction also matched with that of Pd(0) (Figure 3.5c). EDS analysis of the heat treated sample on a quartz substrate revealed that the sample contains only Pd(0) and that the sulfur content is negligible (Figure 3.6).

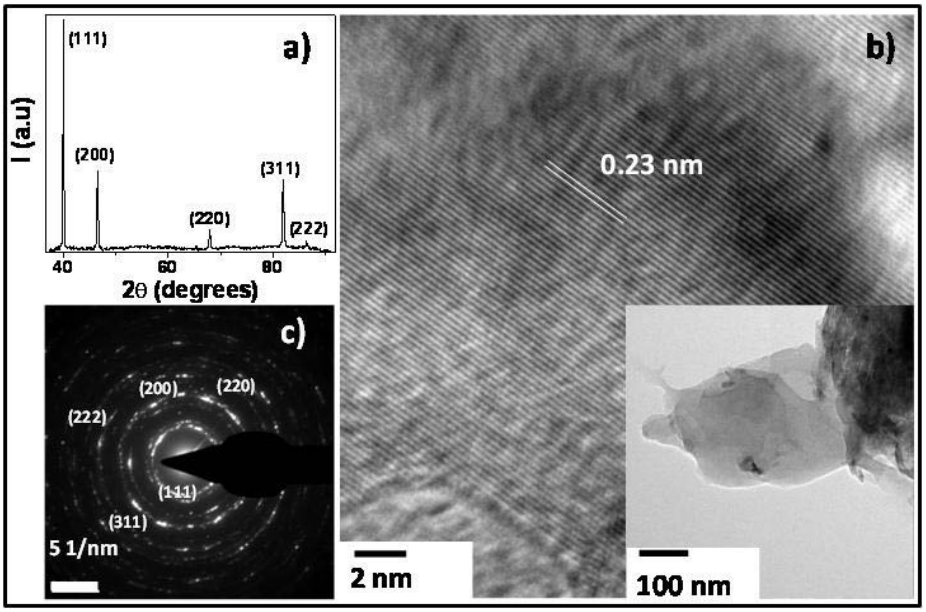

Figure 3.5: a) *PXRD pattern of Pd(0) sheets indexed as per JCPDS card no. 05-0681;* ***b)*** *Enlarged HRTEM image of the Pd(0) sheets showing lattice fringes with separation of 0.23 nm between the fringes.* ***c)*** *FFT image for the Pd(0) sheets showing indexing for the Pd(0) sheets.* ***d)*** *HRTEM image of Pd(0) crystals showing sheet like morphology.*

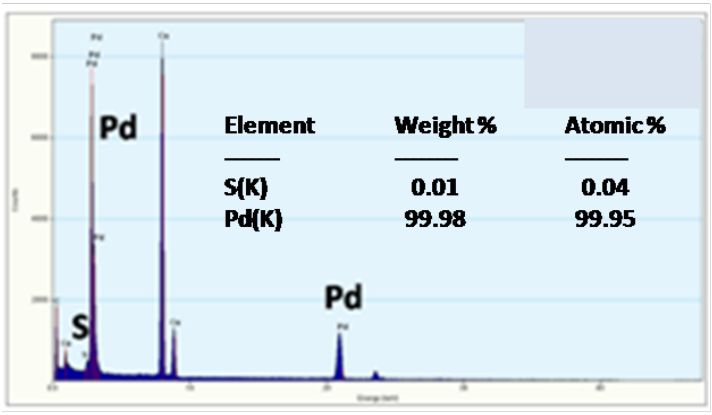

Figure 3.6: *EDAX for the Pd(0) crystals showing negligible sulfur content (almost no sulfur).*

3.3.1.3 Characterization of nickel sulfide nanosheet materials

Characterizations of both the nickel sulfide nanosheet materials viz., Ni_3S_2 and Ni_3S_2-Ni are summarized in Figure 3.7. Figure 3.7a shows the powder XRD pattern for the nickel sulfide (Ni_3S_2) and the nickel sulfide-nickel (Ni_3S_2-Ni) materials. The data obtained for the Ni_3S_2 sample were indexed according to the JCPDS card number (851802). Indexing for the sample Ni_3S_2–Ni was done following the JCPDS card number (851802) for the Ni_3S_2 component and card number (040850) for the metallic nickel existing in its face centered cubic phase. In the powder XRD pattern of the sample Ni_3S_2–Ni, there is marked evidence for the existence of metallic nickel phase as confirmed by the peaks at 2• values 44.5°, 51.8°, and 76.3°(indicated by stars in the graph shown in Figure 3.7a). Figure 3.7b shows HRTEM image with its SAED pattern in the inset and Figure 3.7c shows the lattice fringes of Ni_3S_2 sample where the value of 0.28 nm matches well with that reported in the literature for Ni_3S_2. HRTEM images with the SAED pattern in the inset and the lattice fringes for Ni_3S_2–Ni sample are depicted in Figure 3.7d and 3.7e. The two lattice fringes observed in the Ni_3S_2–Ni sample with the values 0.28 and 0.23 nm correspond to the two different species, namely, Ni_3S_2 and Ni present in the sample. Here, 0.28 nm corresponds to the nickel sulfide part of the sample and 0.23 nm corresponds to the metallic nickel present in the sample. The amounts of nickel and sulfur present in the Ni_3S_2 and Ni_3S_2–Ni samples were determined by using EDAX data. The

two samples show almost similar atomic ratios for Ni:S. In Ni_3S_2 it is approximately 64.5:35.5 (Figure 3.8) and in Ni_3S_2-Ni it is 64.3:35.7 (Figure 3.9).

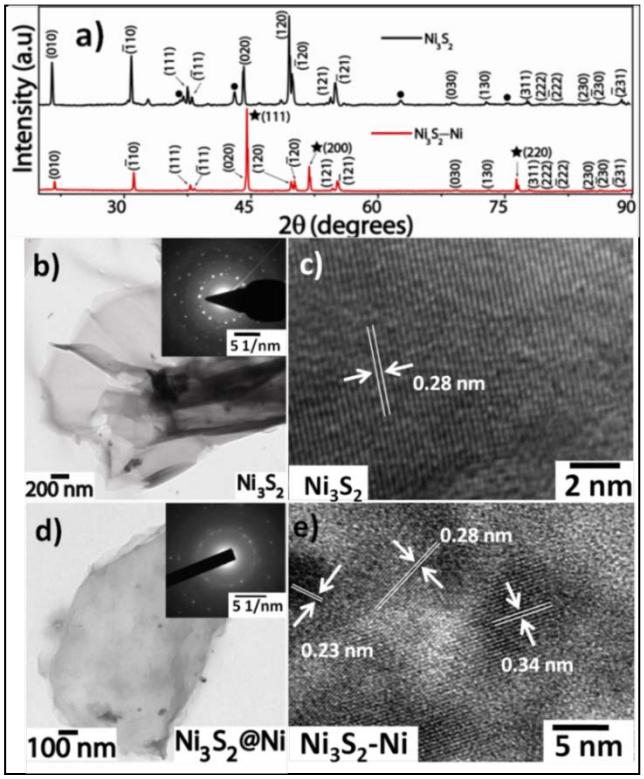

Figure 3.7: a) *Powder XRD patterns for Ni_3S_2 and Ni_3S_2-Ni samples. Note the peaks for pure nickel metal phase as indicated by dark stars in the trace, the (111) peak at 2• ~ 44.5^o corresponds to nickel metal along with the (200) and (220) at 2• ~ 51.8^o and 2• ~ 76.3^o respectively. Dark circles in the trace for Ni_3S_2 indicate NiO impurities. Ni_3S_2 component was indexed according to JCPDS card: 851802.* ***b)*** *TEM image for the sample Ni_3S_2 showing laterally extended micrometer level ultrathin sheet, relevant SAED pattern is shown in the inset.* ***c)*** *HRTEM image showing lattice fringes pertinent to the sample Ni_3S_2 with a fringe gap of 0.28 nm.* ***d)*** *TEM image of Ni_3S_2-Ni sample depicts ultrathin sheets laterally lengthened to micrometer level, with its SAED pattern shown in the inset.* ***e)*** *HRTEM micrograph of Ni_3S_2-Ni shows lattice fringes that correlate to the literature reports, for nickel metal phase the fringe gap comes around 0.23 nm and the nickel sulphide phase lattice fringe gap is around 0.28 nm. 0.34 nm lattice spacing is for carbon on the TEM grid.*

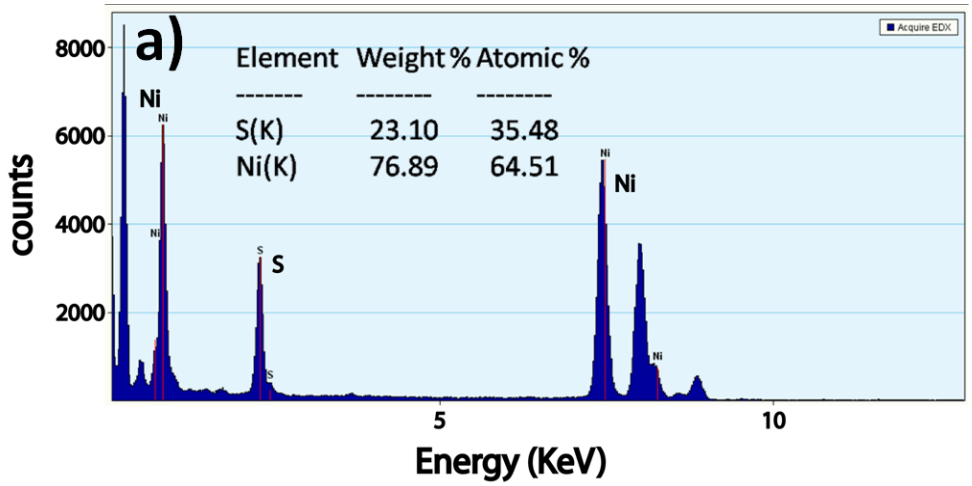

Figure 3.8: *EDAX of the Ni_3S_2 shows the atomic and weight percentages of nickel and sulfur.*

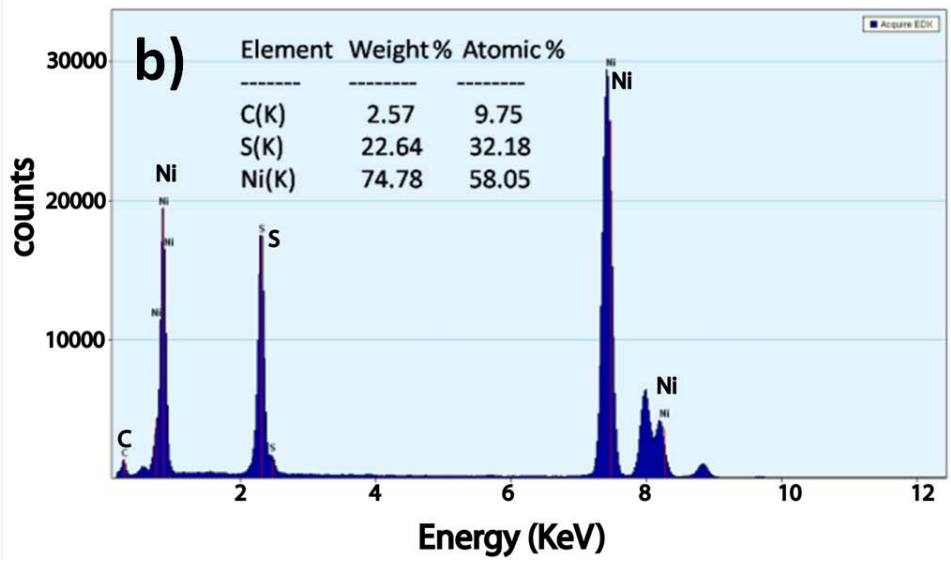

Figure 3.9: *EDAX of the Ni_3S_2-Ni sample shows the atomic and weight percentages of nickel and sulfur revealing the excess of amount of nickel present in the sample.*

3.3.2 Properties of the nickel sulfide nanosheets

3.3.2.1 Magnetic properties

The magnetization results of the nickel/nickel sulfide nanosheets are summarized in the Figure 3.10. Field dependent and temperature dependent magnetization measurements (Squid measurements) were performed on a Quantum Design MPMS 7T SQUID VSM. Field was set in the 3T to -3T range and room temperature was maintained during the field dependent magnetization measurements. Temperature dependent magnetization values were extracted from 5K to 300K while the applied magnetic field was set at 500 Oe.

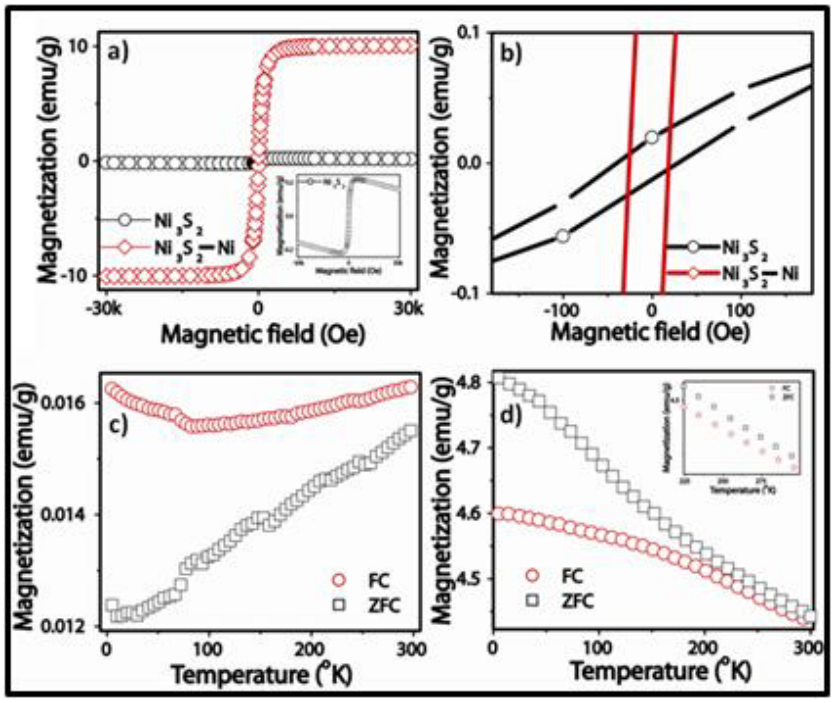

Figure 3.10: *SQUID measurements.* ***a)*** *Room temperature magnetization plotted with magnetic field for the samples Ni_3S_2 and Ni_3S_2-Ni show ferromagnetism in both the samples. Inset in the Figure a) is expanded for clarity.* ***b)*** *Fully magnified trace from the Figure a) reveals coercivity values of about 50 Oe for both the samples Ni_3S_2 and Ni_3S_2-Ni.* ***c)*** *Plot of magnetization with temperature i.e. FC-ZFC curves for the sample Ni_3S_2 displays bifurcation curves indicating higher than room temperature Curie temperature.* ***d)*** *Similar FC-ZFC curves for the Ni_3S_2-Ni sample also indicate higher than room temperature Curie temperature (inset of the Figure d).*

Interestingly M_S of Ni_3S_2-Ni sample was determined to be 10 emu g^{-1}. The other nickel sulfide Ni_3S_2 also showed a ferromagnetic M_S value of 0.2 emu g^{-1}. In the pure Ni_3S_2 sample an inherent diamagnetic contribution (in the inset of the Figure 3.10a) along with a reasonable ferromagnetism could be noticed clearly. Such diamagnetic contribution could come from the Ni^{2+} cations or any organic remnants. The coercivity value (H_C) for both the samples was deduced to be 50 Oe. Corresponding magnetization data with respect to temperature were obtained in the zero-field cooling (ZFC) and field cooling (FC) modes in the temperature range 5 ^oK to 300 ^oK and with an applied magnetic field of 500 Oe. The ZFC-FC measurements showed bifurcation curves providing evidence for higher than room temperature Curie temperatures in both these samples (Figure 3.10c for the Ni_3S_2 sample and Figure 3.10d for the Ni_3S_2-Ni sample). The curves for Ni_3S_2-Ni sample are smooth and are devoid of any step like features, indicating the absence of any blocking temperature. This shows that the metallic nickel phase present in the biphasic Ni_3S_2-Ni composite is not super-paramagnetic but is ferromagnetic in nature and the Ni_3S_2 part is strongly interacting with the metallic Ni phase.

AFM/MFM was carried out under ambient conditions using commercially available Si cantilevers coated with a cobalt/chromium film with the normal resonance frequency of 78 kHz and spring constant of 3 N/m (BudgetSensor). AFM topography and MFM images were taken in NAP mode which is a two pass technique where the first pass is typically used to measure (and collect) topography and the second pass is used to measure magnetic signal due to stray fields created by magnetic tip. The MFM images were taken in NAP mode at a distance of more than 50 nanometers for both the samples to avoid the influence of topography image on the MFM data. MFM being a powerful technique augmented the results obtained from the SQUID magnetometer. The images obtained from bulk samples revealed presence of stacked layers (Figure 3.11). However, no meaningful deductions could be made from these images except an observation that the edges display enhanced magnetic characteristics (Figure 3.12). Interestingly, a simple Bronsted acid mediated exfoliation of the bulk layered samples converted big sheets into circular disks. This was actually performed on the samples during testing for their

electrochemical activity towards the hydrogen generation, which is thoroughly dealt with in the next section on the electrocatalytic activity of these samples. As for now, it can be concluded that there occurred a structural transformation in the nanosheets of both the samples upon simple acid treatment leading to a morphology change from thick layered samples to nanodisks. These were coated on mica wafers facilitating the magnetic force microscopic imaging very well. The results from the imaging are presented in Figure 3.13. Figure 3.13a provides the morphological features of the Ni_3S_2-Ni sample and the corresponding magnetic force microscopic image is depicted in Figure 3.13b. The average height of the disc (Figure 3.13e) is about 60 nm. Figure 3.13f shows the magnetic phase shifts observed in this sample, analyzed from four particles (red line in the Figure 3.13b).

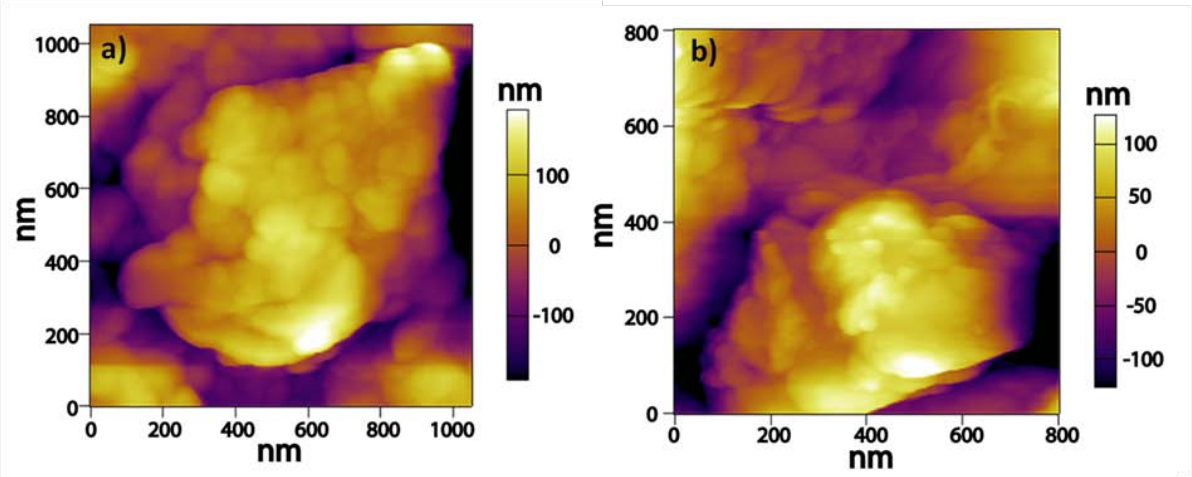

Figure 3.11: *a), b) Contact tapping mode atomic force microscopic images of the two samples Ni_3S_2-Ni and Ni_3S_2 respectively reveal morphological features of the samples with thickness of measured the samples being around 100 nm.*

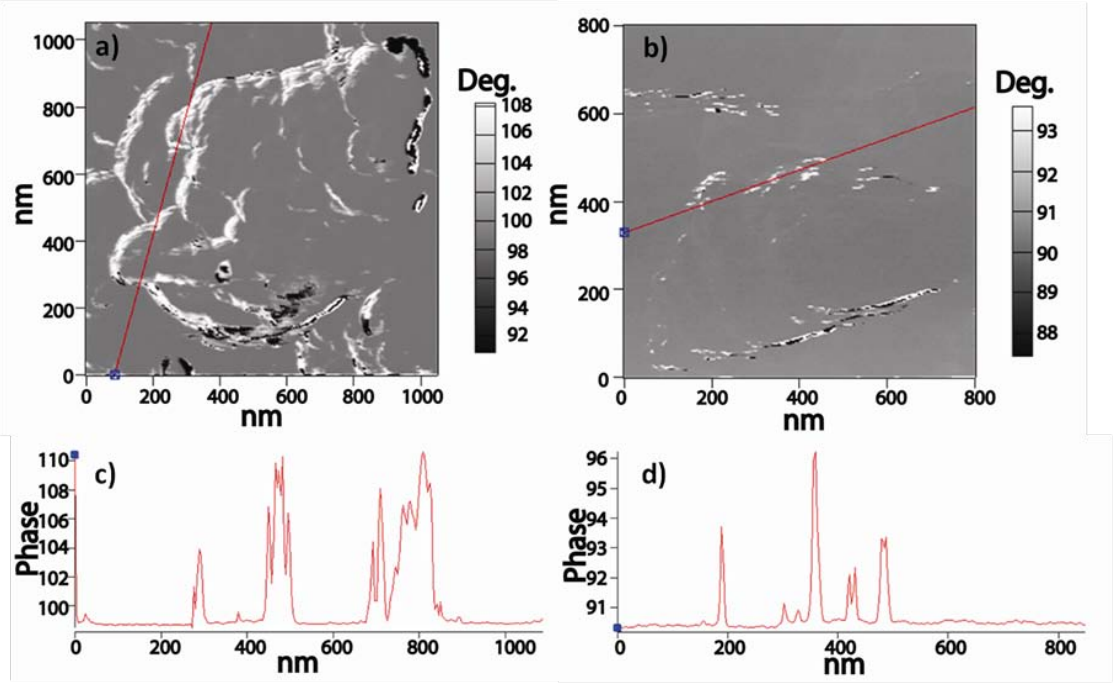

Figure 3.12: *a), b) Magnetic force microscopic micrographs of the samples Ni_3S_2-Ni and Ni_3S_2 respectively obtained by employing a magnetic tip with a tip lift height 30 nm from above the sample in contact tapping mode display positive phase shift in the magnetic field emanating just from the edges of the samples in both the samples but not from the bulk of the samples. c), d) Spectra presenting the magnetic phase shift existing in the samples Ni_3S_2-Ni and Ni_3S_2 respectively. A positive phase shift in the magnetic property can be observed.*

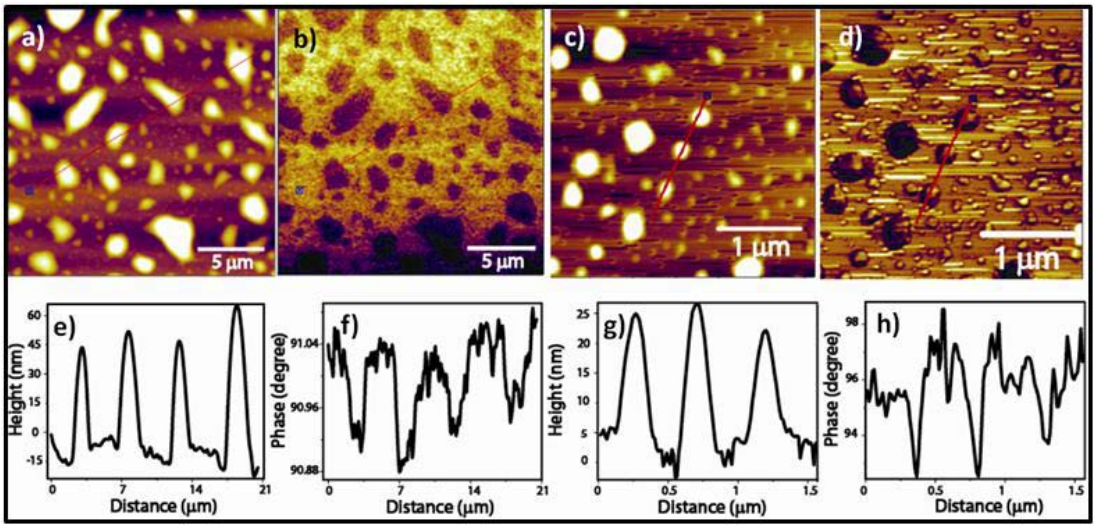

Figure 3.13: *Images obtained using magnetic force microscopy.* ***a)*** *Topographical image from the magnetic force microscopy experiment on the Ni_3S_2-Ni sample. Four particles were analyzed (red line) for their height profiling as is shown in* ***e)****. The trace* ***b)*** *shows magnetic force microscopic image for the sample Ni_3S_2-Ni and its corresponding phase measurement was depicted in Figure* ***f)****. A clear negative phase shift was observed as can be seen from the Figure* ***f)****. Figure* ***c)*** *shows the topological imaging data on the particles analyzed (red line) for the sample Ni_3S_2. The corresponding graph depicting height profile of the sample Ni_3S_2 was shown in* ***g)****. The Figure* ***d)*** *presents the magnetic force microscopic image for the sample Ni_3S_2 taking the same particle analyzed for topographical features. Figure* ***h)*** *shows the graph representing the phase measurement for the sample Ni_3S_2 for the particles analyzed for the magnetic features in* ***d)****.*

A negative phase shift could be clearly seen which are common for ferromagnetic samples and are attributed to the attractive forces existing between the samples and the magnetic tip. Similarly, for the Ni_3S_2 sample, Figure 3.13c gives the topographical image and Figure 3.13d depicts the magnetic force microscopic image. Here again disc like objects with an average height of 25 nm (Figure 3.13g) which display negative phase shifts in MFM mode (Figure 3.13h) are seen.

All the above features strongly suggest that both the samples are featured with room temperature ferromagnetism. According to Stoner's criterion, strong exchange interactions and presence of higher density of states in the Fermi energy level favor ferromagnetic behavior in magnetic materials. And as dimensions of the magnetic materials decrease, for example, from three dimensional materials to 2D sheet like structures, density of states increases at the Fermi energy level due to narrowing of the band width at these dimensions. Furthermore, the coordination number of the surface atoms decreases in low dimensional materials facilitating increased count of free electrons and thus resulting in enhanced magnetic expression as observed for the 2D circular disks here. A low magnification image of the Ni_3S_2-Ni sample gives details about the disk shape formed in the sample after the Bronsted acid treatment (Figure 3.14). Figure 3.14c is the 3D imaging in the force microscopy that shows 3D view of the disk of the sample.

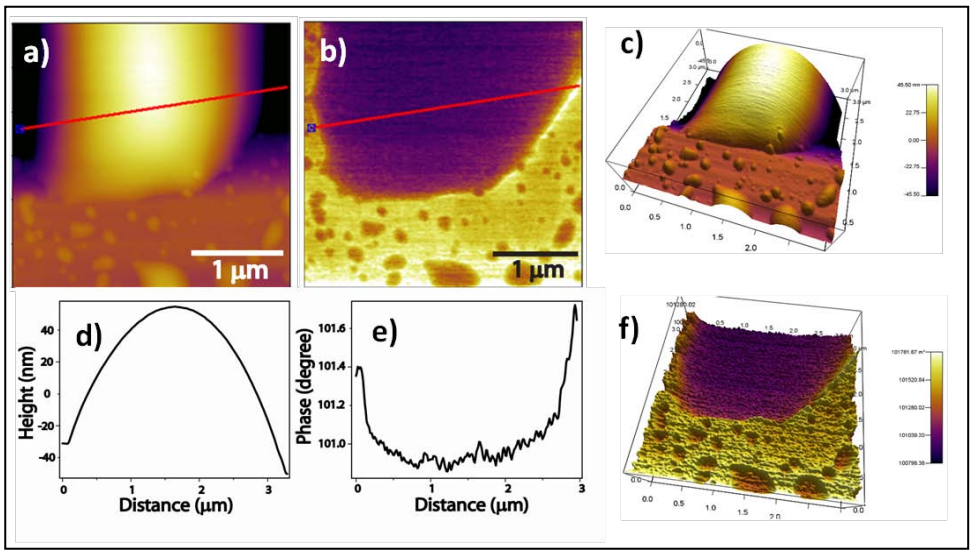

Figure 3.14: *Topographical image and* ***b)*** *magnetic force microscopic image for the sample Ni_3S_2-Ni.* ***c)*** *3D view of the topographical image.* ***d)*** *Graph representing the height profile for the topological image depicted in* ***a)****.* ***e)*** *Gives a glimpse of the magnetic force microscopic phase measurement for the same sample.* ***f)*** *3D representation of the magnetic force microscopic image.*

3.3.2.2 Semiconducting properties

In order to investigate the semiconducting nature of these nickel sulfide nanosheets, cyclic voltammetry was performed on both Ni_3S_2 and Ni_3S_2-Ni samples, in an inert atmosphere with dry acetonitrile as the solvent and glassy carbon as the working electrode (Figure 3.15). 0.2 M *tert*-butyl ammonium perchlorate (TBAP) was used as electrolyte. Internal standard used was 0.01 M ferrocene which showed oxidation and reduction peaks centered around -1 V. Equations (1) & (2) were employed to calculate the valence and conduction band edges.

$$E_{HOMO} = -(E_{ox}^{onset} + 4.8eV) \quad (1)$$

$$E_{LUMO} = -(E_{red}^{onset} + 4.8eV) \quad (2)$$

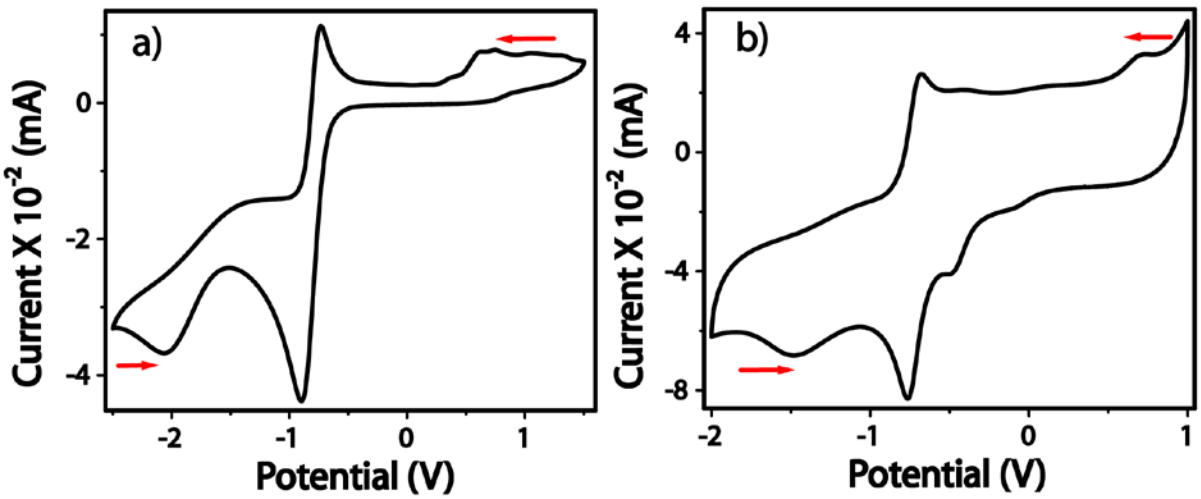

Figure 3.15: *Cyclic voltammograms of* ***a)*** *Ni_3S_2 and that of* ***b)*** *Ni_3S_2-Ni sample.*

Using the cyclic voltammogram obtained (Figure 3.15a), the energy band gap of Ni_3S_2 sample was calculated to be 2.81 eV from the onset oxidation and reduction potential values 0.75 V and -2.06 V respectively. Similarly for the Ni_3S_2-Ni, band gap energy was found out to be 2.18 eV from the onset oxidation and reduction potential values 0.70 V

and -1.48 V respectively obtained from its cyclic voltammogram (Figure 3.15b). Thus based on magnetization and CV studies, we conclude that the samples being investigated possess both room temperature ferromagnetic and semiconducting characteristics.

3.3.3 Conclusions

Thin metal/metal sulfide were prepared using simple heating techniques. Thermogravimetric analyses predicted that two different products resulted from each molecular precursor, i.e. PdS and palladium metal sheets from palladium octanethiolate and Ni_3S_2 and Ni_3S_2-Ni from the nickel octanethiolate.

Ni_3S_2/Ni_3S_2-Ni nanosheets displayed good room temperature ferromagnetic characteristics as is evident from the SQUID and MFM characterization. These two samples also exhibited semiconductor properties proven through cyclic voltammetric measurements for determining their band gaps.

3.3.4 Applications of nickel sulfide nanosheets-Electrocatalytic H_2 generation

Owing to the abundant and low cost character nickel [26, 27] based electrocatalysts assume prominence in energy related research as compared to the precious metals such as platinum [28-31] and palladium based ones [32, 33]. Though cobalt and other metal based materials also are presumably cheaper for the energy related photo/electrocatalytic applications [34], their toxic nature compared to the nickel based materials make them less attractive [35-43]. Thus there exists a great need for the development of nickel based electro/photo catalytically active materials [44-53]. Since we had readily available large amounts of nickel/nickel sulfides, we proceeded further to test them for any hydrogen generation property. Our results indicated that these nickel/nickel sulfide nanosheets showed reasonable current densities at low overpotentials. Electrochemical hydrogen generation was achieved in the nickel sulfide-nickel nanosheets (Ni_3S_2-Ni) and also in the nickel sulfide (Ni_3S_2) nanosheets at low overpotentials in acidic pH under 1 M H_2SO_4 solution. The details of the results are presented in the rest of the chapter.

The electrochemical experimental conditions utilized for the Hydrogen Evolution Reaction (HER) are as follow:

- Electrolyte: 1M H_2SO_4 solution
- Reference electrode: Ag/AgCl in KCl solution
- Counter electrode: Platinum wire
- Working electrode: Sample material on Glassy carbon rotating disk (RD) electrode
- Rotating Speed of Electrode: 1500 RPM (rotations per minute)

Figure 3.16 shows the linear sweep voltammetry (LSV) curves for both the samples. After resistance correction and deduction of the contribution from Ag/AgCl electrode, the overpotential value calculated at 1 mA/cm^2 for Ni_3S_2-Ni nanosheets was found to be -320 mV. This value is among the lowest overpotential values reported for nickel based electro-catalysts as far as we are aware. Similarly for the Ni_3S_2 nanosheets, the overpotential value was found to be -832 mV. The table in the Figure 3.17 summarizes the overpotential values of both the nickel sulfide nanosheets. Presence of metallic nickel in combination with nickel sulfide in the Ni_3S_2-Ni sample could be the plausible reason for the lower overpotential value exhibited by this sample.

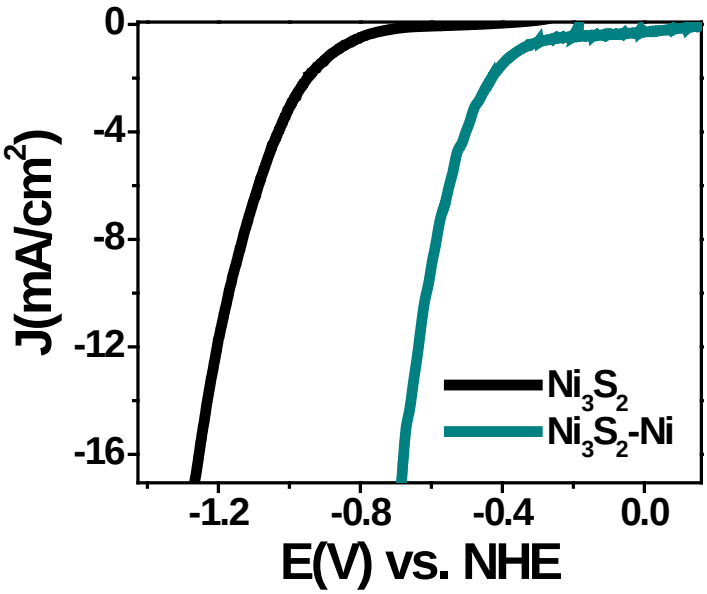

***Figure 3.16**: Electrochemical overpotential comparison for the two samples Ni_3S_2-Ni and Ni_3S_2 after the 50th cycle for both the samples.*

Sample	Overpotential at 1 mA/cm^2
Ni_3S_2-Ni at 50th cycle	**-320 mV**
Ni_3S_2 at 50th cycle	**-832 mV**

***Table 3.17:** Electrochemical hydrogen evolution reaction. Table summarizes the electrochemical hydrogen generation properties of the Ni_3S_2-Ni and Ni_3S_2 nanosheets at the initial LSV cycle.*

Tafel plots for these nickel sulfide nanosheets derived from the linear sweep voltammetry (LSV) displayed values about 36.3 mA/dec for the Ni_3S_2-Ni nanosheets and 50.6 mA/dec for the Ni_3S_2 nanosheets (Figure 3.18).

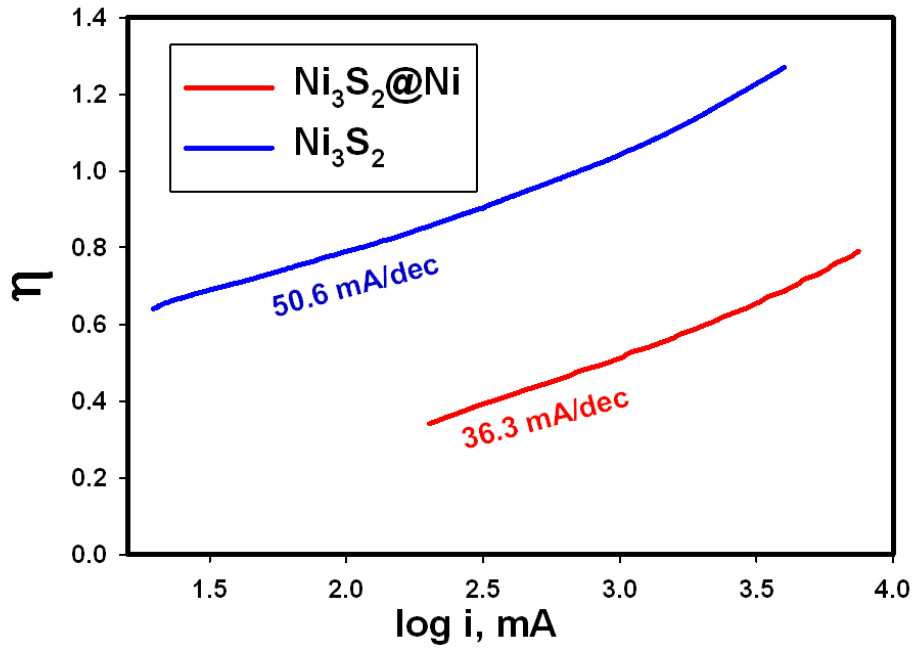

Figure 3.18: *Tafel plots for both the samples.*

The huge difference in overpotential values between the two samples was further investigated by performing electrochemical cycling on both the samples for at least up to 500 linear sweep voltammetric cycles. Interestingly, the overpotential shifted to higher values gradually in both the samples. However, after a few cycles, the overpotential values started to decrease but again gradually. The reduction in the overpotential values occurred till the values reached the initial value (Figure 3.19). This was unseen previously in any nickel sulfide electrocatalytic materials. This indicates some plausible changes in the morphology or structure of the nickel sulfides. To further probe into the possible structural changes, electron microscopic imaging was employed to look at the samples both at the start of the electrochemical hydrogen evolution reaction and at the end of the electrochemical cycling.

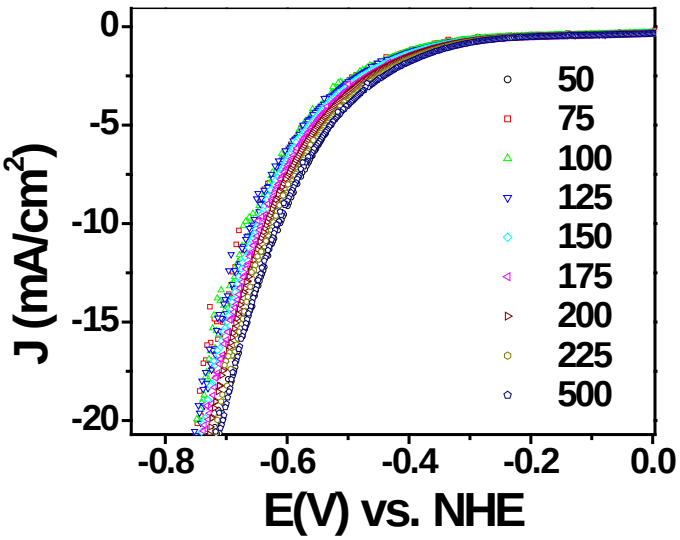

Figure 3.19: *LSV plots for the Ni_3S_2-Ni sample during the electrochemical cycling .*

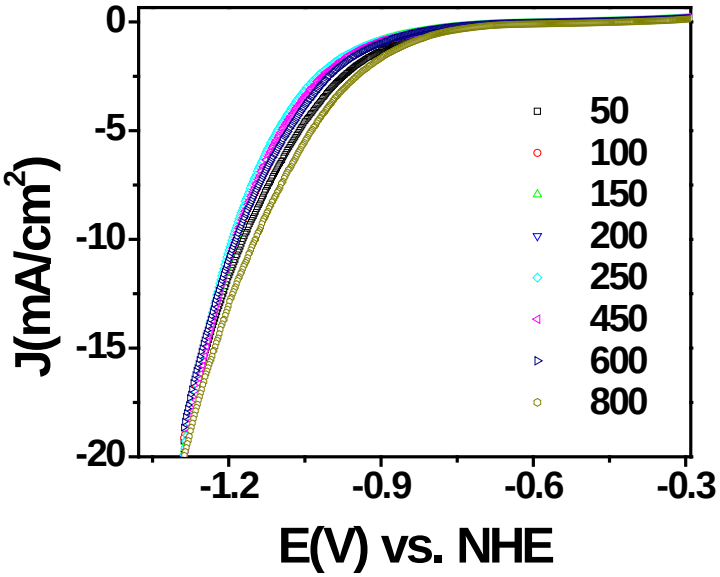

Figure 3.20: *LSV plot for the Ni_3S_2 sample during the electrochemical cycling.*

From the HRTEM images (Figure 3.20), it could be concluded that a structural transformation occurred in both the samples after the electrochemical cycling. The images clearly show transformation of nanosheets to nanodisks in both the samples (Figure 3.21a to b and d to e). Please recollect the discussion in the previous section on the magnetic properties of the samples wherein when the samples were treated with an acid such as H_2SO_4 that again revealed a structural transformation of the nanosheets to nanodisks.

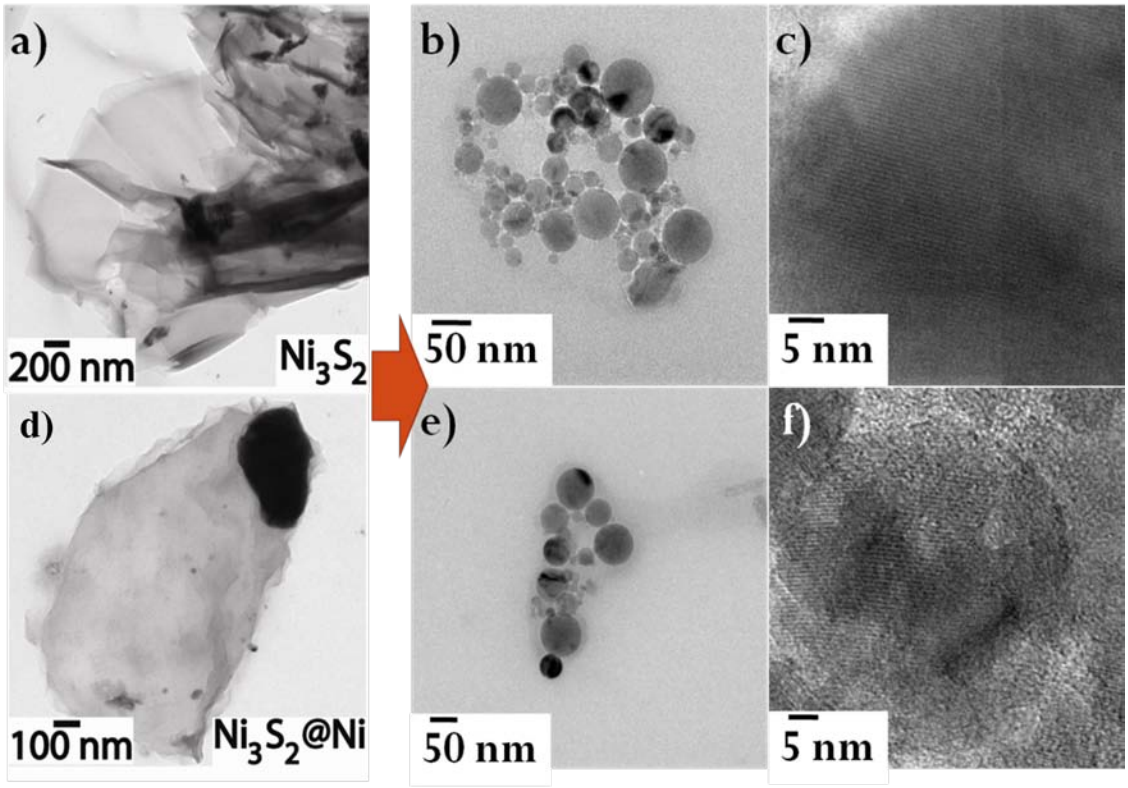

Figure 3.21: *HRTEM images for both the samples before (a, d) and after (b, c, e and f) electrochemical cycling* .

Imaging with force microscopy also revealed the structural transformation for the nickel sulfide nanosheets and nanodisks before the cycling and after the cycling respectively. The AFM images for both the samples Ni_3S_2-Ni and Ni_3S_2 before electrochemical cycling reveal thick layers having height profiles about 300 nm (Figure 3.22) and after

electrochemical cycling reveal thin nanodisks having height profiles about 50 nm (Figure 3.23).

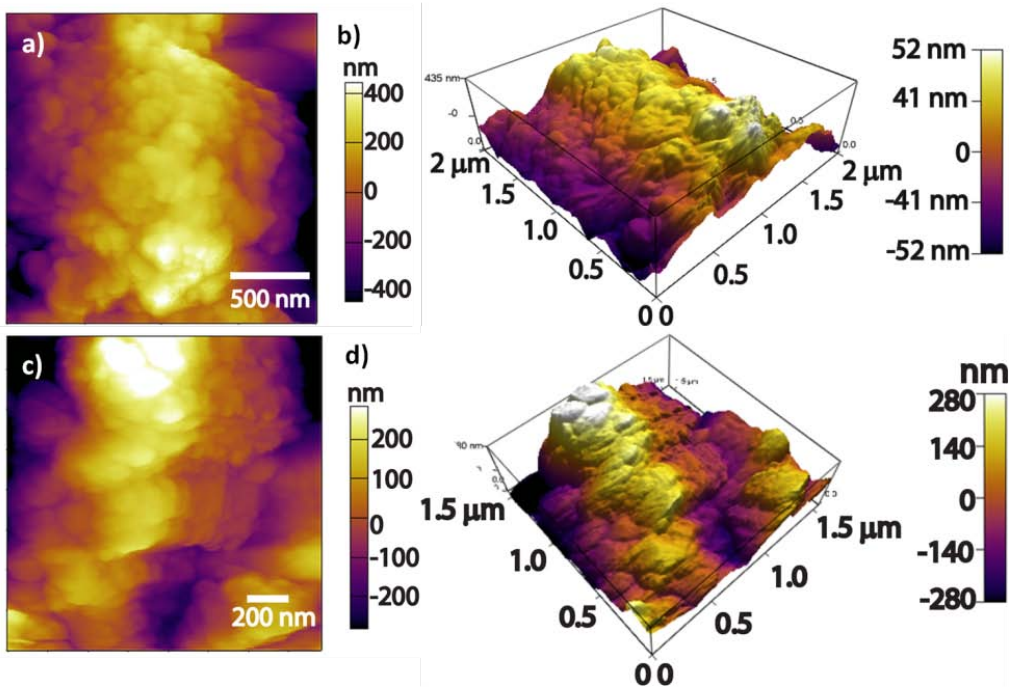

Figure 3.22: *Atomic force microscopy of the Ni_3S_2-Ni (a, b) and Ni_3S_2 (c, d) nanosheets before electrochemical cycling.*

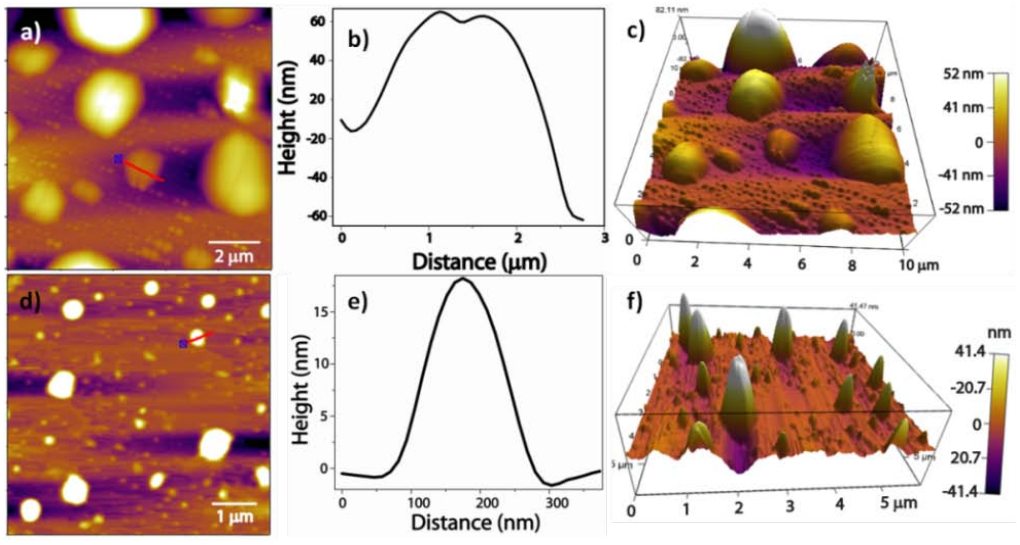

Figure 3.23: *Atomic force microscopy of the Ni_3S_2-Ni (a, b and c) and Ni_3S_2 (d, e and f) nanodisks after electrochemical cycling.*

However, the mechanism by which this structural transformation from nanosheets to nanodisks is occurring is still not clear as such. One reason for such structural transformation could be the hydrogen evolving from the samples. Another causative could be the electrochemical potential. To check this, the samples were subjected to linear sweep voltammetry under a non-aqueous environment. As hydrogen evolution would be absent in non-aqueous environment, we opined that this would clearly establish whether hydrogen evolution is playing any role in the structural evolution. This non-aqueous electrochemistry on both the samples was performed in dry acetonitrile. The conditions were as under:

- Electrolyte: Dry acetonitrile
- Reference electrode: Ag/AgCl in KCl solution
- Counter electrode: Platinum wire
- Working electrode: Sample material on Glassy carbon RD electrode
- Rotating Speed of Electrode: 1500 RPM

The samples are dispersed in dry acetonitrile and then coated onto the RD electrode. TBAP (tetrabutylammonium perchlorate) was used as supporting electrolyte which is dissolved in the dry acetonitrile. These experiments were performed on the Ni_3S_2-Ni sample.

It can be clearly noticed that the linear sweep voltammetric curves in non-aqueous environment (Figure 3.24) are very similar to those obtained in the aqueous electrochemistry experiments. Here again the Ni_3S_2-Ni sample depict that same trend as seen in the aqueous conditions. More specifically the linear sweep voltammetric curves followed the same path of first increase in the electrochemical potential values but after attaining certain number of cycles these curves again reverted back to the original first potential value. These experiments thus confirmed that the nanodisks are being formed due to the electrochemical potential but not the evolving hydrogen.

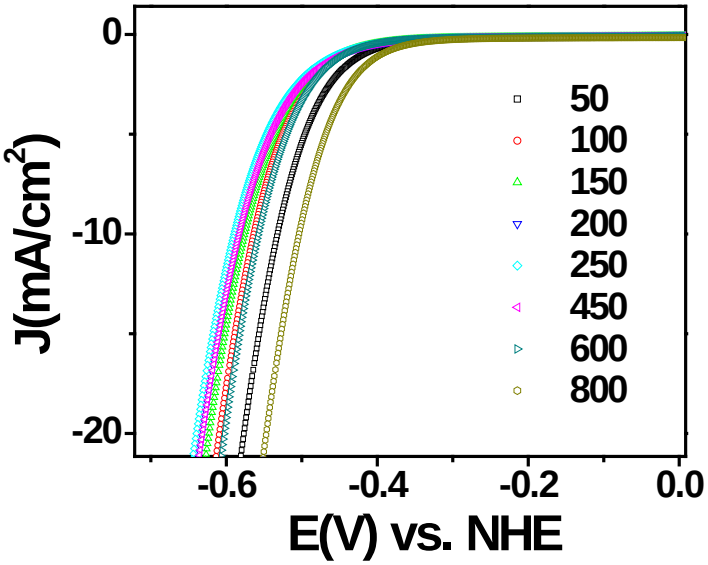

***Figure 3.24**: Linear sweep voltammetry data for the Ni_3S_2-Ni sample through electrochemical cycling.*

This was further confirmed from the TEM imaging performed on Ni_3S_2-Ni sample after electrochemical cycling in non-aqueous environment (Figure 3.25).

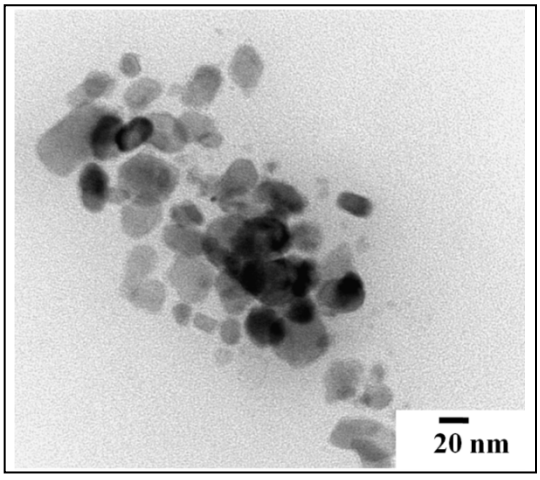

***Figure 3.25:** TEM image of the Ni_3S_2-Ni sample after non-aqueous electrochemical cycling for 800 cycles.*

3.4 Conclusions

In this chapter, preparation of metal nanosheets and metal sulfide nanosheets from their precursor metal thiolate molecular nanosheets was demonstrated. The procedure employed for preparing these end products which were again nanosheets is more convenient compared to the existing prominent sophisticated instrumental techniques for preparing similar quality nanosheets. Palladium metallic nanosheets and palladium sulfide nanosheets were prepared from the precursor palladium thiolate molecular sheets and similarly nickel sulfide nanosheets were accessed from the nickel thiolate molecular nanosheets. The nickel/nickel sulfide nanosheets displayed interesting properties such as room temperature ferromagnetism and a combination of magnetic and semiconducting characteristics. We also demonstrated that these could be utilized as catalysts for energy related applications. An interesting morphological variation was seen to be associated with the electrochemical treatment where nanosheets were found transformed to nanodisks.

3.5 References

[1]. Novoselov, K. S.; Geim, A. K.; Morozov, S. V.; Jiang, D.; Zhang, Y.; Dubonos, S. V.; Grigorieva, I. V.; Firsov , A. A., Electric field effect in atomically thin carbon films. *Science* **2004,** 306, 666.

[2]. Novoselov, K. S.; Jiang, D.; Schedin, F.; Booth, T. J.; Khotkevich, V. V.; Morozov, S. V.; Geim, A. K., Two-dimensional atomic crystals. *Proc. Natl. Acad. Sci. U. S. A.* **2005,** 102, 10451.

[3]. Nicolosi, V.; Chowalla, M.; Kanatzidis, M., G.; Strano, M., S.; Coleman, J., N., Liquid exfoliation of layered materials. *Science* **2013,** 340, 1420.

[4]. Nam, K. T.; Shelby, S. A.; Choi, P. H.; Marciel, A. B.; Chen, R.; Tan, L.; Chu, T. K.; Mesch, R. A.; Lee, B. C.; Connolly, M. D.; Kisielowski, C.; Zuckermann, R. N., Free-floating ultrathin two-dimensional crystals from sequence-specific peptoid polymers. *Nat Mater.* **2010,** 9, 454.

[5]. Matte, H. S. S. R.; Gomathi, A.; Manna, A. K.; Late, D. J.; Datta, R.; Pati, S. K.; Rao, C. N. R., MoS_2 and WS_2 analogues of graphene. *Angew. Chem. Intl. Ed.* **2010,** 122, 4153.

[6]. Shinde, D. V.; Patil, S. A.; Cho, K.; Ahn, D. Y.; Shrestha, N. K.; Mane, R. S.; Lee, J. K.; Han, S.-H., Revisiting metal sulfide semiconductors: a solution-based general protocol for thin film formation, hall effect measurement, and application prospects. *Adv. Funct. Mater.* **2015**, 25, 5739.

[7]. Tukhtaev, R. K.; Boldyrev, V. V.; Gavrilov, A. I.; Larionov, S. V.; Myachina, L. I.; Savel'eva, Z. A., Metal sulfide synthesis by self-propagating combustion of sulfur-containing complexes. *Inorganic Materials* **2002,** 38, 985.

[8]. Aksit, M.; Toledo, D. P.; Robinson, R. D., Scalable nanomanufacturing of millimetre-length 2D $NaxCoO_2$ nanosheets. *J. Mater.Chem.* **2012,** 22, 5936.

[9]. Hassan, M.; Hussian, H.; Dawood, M., Synthesis of semiconductor oxide nanosheets, nanotetrapods and nanoplane-suite like grown on metal foil using different method. *International Nano Letters* **2015,** 5, 147.

[10]. Du, Y.; Yin, Z.; Zhu, J.; Huang, X.; Wu, X.-J.; Zeng, Z.; Yan, Q.; Zhang, H., A general method for the large-scale synthesis of uniform ultrathin metal sulphide nanocrystals. *Nat. Commun.* **2012,** 3, 1177.

[11]. Duan, H.; Yan, N.; Yu, R.; Chang, C.-R.; Zhou, G.; Hu, H.-S.; Rong, H.; Niu, Z.; Mao, J.; Asakura, H.; Tanaka, T.; Dyson, P. J.; Li, J.; Li, Y., Ultrathin rhodium nanosheets. *Nat. Commun.* **2014,** 5, 3093.

[12]. Fan, Z.; Huang, X.; Tan, C.; Zhang, H., Thin metal nanostructures: synthesis, properties and applications. *Chemical Science* **2015,** 6, 95.

[13]. Fan, Z.; Zhang, X.; Yang, J.; Wu, X.-J.; Liu, Z.; Huang, W.; Zhang, H., Synthesis of 4H/fcc-Au@metal sulfide core-shell nanoribbons. *J. Am. Chem. Soc.* **2015,** 137, 10910.

[14]. Al-Hada, N. M.; Saion, E. B.; Shaari, A. H.; Kamarudin, M. A.; Flaifel, M. H.; Ahmad, S. H.; Gene, S. A., A Facile Thermal-treatment route to synthesize ZnO nanosheets and effect of calcination temperature. *PLoS ONE* **2014,** 9, e103134.

[15]. Matte, H. S. S. R.; Subrahmanyam, K. S.; Rao, C. N. R., Novel magnetic properties of graphene: presence of both ferromagnetic and antiferromagnetic features and other aspects. **2009,** 113, 9982.

[16]. Li, H.; Dai, J.; Li, J.; Zhang, S.; Zhou, J.; Zhang, L.; Chu, W.; Chen, D.; Zhao, H.; Yang, J.; Wu, Z., Electronic structures and magnetic properties of GaN sheets and nanoribbons. *J. Phys. Chem. C.* **2010,** 114, 11390.

[17]. Shi, H.; Pan, H.; Zhang, Y.-W.; Yakobson, B. I., Strong ferromagnetism in hydrogenated monolayer MoS_2 tuned by strain. *Phy. Rev. B.* **2013,** 88, 205305, 1.

[18]. Zhang, X.; Zhao, M.; Wang, A.; Wanga, X.; Du, A., Spin-polarization and ferromagnetism of graphitic carbon nitride materials. *J. Mat. Chem. C.* **2013,** 1, 6265.

[19]. Zhang, Z.; Zou, X.; Crespi, V. H.; Yakobson, B. I., Intrinsic magnetism of grain boundaries in two-dimensional metal dichalcogenides. *ACS Nano* **2013,** 7, 10475.

[20]. Cheng, W.; He, Z.; Yao, T.; Sun, Z.; Jiang, Y.; Liu, L.; Jiang, S.; Hu, F.; Xie, Z.; He, B.; Yan, W.; Wei, S., Half-unit-cell • -Fe_2O_3 semiconductor nanosheets with intrinsic and robust ferromagnetism. *J. Am. Chem. Soc.* **2014,** 136, 10393.

[21]. Han, Y.; Hu, T.; Li, R.; Zhou, J.; Dong, J., Stabilities and electronic properties of monolayer MoS_2 with one or two sulfur line vacancy defects. *Phys. Chem. Chem.Phys.* **2014**, 17, 3813.

[22]. Song, L. X.; Yang, Z. K.; Teng, Y.; Xia, J.; Du, P., Nickel oxide nanoflowers: formation, structure, magnetic property and adsorptive performance towards organic dyes and heavy metal ions. *J. Mat. Chem. A.* **2014,** 1, 8731.

[23]. Wang, J. K.; Marcinkova, A.; Chen, C.-W.; He, H.; Aronson, M.; Morosan, E., Magnetic and transport properties of the layered transition-metal pnictides $R_3T_4As_4O_{2-}$ (R = La, Ce, Pr, Nd, and Sm, T = Ni, Cu). *Phy. Rev. B.* **2014,** 89, 094405, 1.

[24]. Xia, B.; An, L.; Gao, D.; Shi, S.; Xi, P.; Xue, D., Hierarchical ultrathin $Mo(SxSe_{1-x})_2$ nanosheets with tunable ferromagnetism and efficient hydrogen evolution reaction activity: towards defect site effect. *Cryst. Eng. Chem.* **2015,** 17, 6420.

[25]. Ma, W.; Ma, R.; Wang, C.; Liang, J.; Liu, X.; Zhou, K.; Sasaki, T., A superlattice of alternately stacked Ni-Fe hydroxide nanosheets and graphene for efficient splitting of water. *ACS Nano* **2015,** 9, 1977.

[26]. Popczun, E. J.; McKone, J. R.; Read, C. G.; Biacchi, A. J.; Wiltrout, A. M.; Lewis, N. S.; Schaak, R. E., Nanostructured nickel phosphide as an electrocatalyst for the hydrogen evolution reaction. *J. Am. Chem. Soc.* **2013**, 135, 9267.

[27]. Chhetri, M.; Rana, M.; Loukya, B.; Patil, P. K.; Datta, R.; Gautam, U. K., Mechanochemical synthesis of free-standing platinum nanosheets and their electrocatalytic properties. *Adv. Mater.* **2015,** 27, 4430.

[28]. Kuang, Y.; Cai, Z.; Zhang, Y.; He, D.; Yan, X.; Bi, Y.; Li, Y.; Li, Z.; Sun, X., Ultrathin dendritic Pt_3Cu triangular pyramid caps with enhanced electrocatalytic activity. *ACS Appl. Mater. & Interfaces* **2014,** 6, 17748.

[29]. Cai, Z.; Kuang, Y.; Qi, X.; Wang, P.; Zhang, Y.; Zhang, Z.; Sun, X., Ultrathin branched PtFe and PtRuFe nanodendrites with enhanced electrocatalytic activity. *J. Mater. Chem. A.* **2015,** 3, 1182.

[30]. Durst, J.; Simon, C.; Hasché, F.; Gasteiger, H. A., Hydrogen oxidation and evolution reaction kinetics on carbon supported Pt, Ir, Rh, and Pd electrocatalysts in acidic media. *J. Electrochem. Soc.* **2015,** 162, 190.

[31]. Pan, Y.-T.; Yin, X.; Kwok, K. S.; Yang, H., Higher-order nanostructures of two-dimensional palladium nanosheets for fast hydrogen sensing. *Nano Lett.* **2014,** 14, 5953.

[32]. Huang, X.; Tang, S.; Mu, X.; Dai, Y.; Chen, G.; Zhou, Z.; Ruan, F.; Yang, Z.; Zheng, N., Freestanding palladium nanosheets with plasmonic and catalytic properties. *Nat Nano* **2011,** 6, 28.

[33]. Yang, L.; Zhou, W.; Hou, D.; Zhou, K.; Li, G.; Tang, Z.; Li, L.; Chen, S., Porous metallic MoO_2-supported MoS_2 nanosheets for enhanced electrocatalytic activity in the hydrogen evolution reaction. *Nanoscale* **2015,** 7, 5203.

[34]. Callejas, J. F.; Read, C. G.; Popczun, E. J.; McEnaney, J. M.; Schaak, R. E., Nanostructured Co2P Electrocatalyst for the hydrogen evolution reaction and direct comparison with morphologically equivalent CoP. *Chem. Mater.* **2015,** 27, 3769.

[35]. Harvey, A.; Backes, C.; Gholamvand, Z.; Hanlon, D.; McAteer, D.; Nerl, H. C.; McGuire, E.; Seral-Ascaso, A. s.; Ramasse, Q. M.; McEvoy, N.; Winters, S. a.; Berner, N. C.; McCloskey, D.; Donegan, J. F.; Duesberg, G. S.; Nicolosi, V.; Coleman, J. N., Preparation of gallium sulfide nanosheets by liquid exfoliation and their application as hydrogen evolution catalysts. *Chem. Mater.* **2015,** 27, 3483.

[36]. McEnaney, J. M.; Chance Crompton, J.; Callejas, J. F.; Popczun, E. J.; Read, C. G.; Lewis, N. S.; Schaak, R. E., Electrocatalytic hydrogen evolution using amorphous tungsten phosphide nanoparticles. *Chem. Commun.* **2014,** 50, 11026.

[37]. McEnaney, J. M.; Crompton, J. C.; Callejas, J. F.; Popczun, E. J.; Biacchi, A. J.; Lewis, N. S.; Schaak, R. E., Amorphous molybdenum phosphide nanoparticles for electrocatalytic hydrogen evolution. *Chem. Mater.* **2014,** 26, 4826.

[38]. Popczun, E. J.; Read, C. G.; Roske, C. W.; Lewis, N. S.; Schaak, R. E., Highly active electrocatalysis of the hydrogen evolution reaction by cobalt phosphide nanoparticles. *Angew. Chemie Intl. Ed.* **2014,** 53, 5427.

[39]. Shi, J.; Hu, J., Molybdenum sulfide nanosheet arrays supported on Ti plate: an efficient hydrogen-evolving cathode over the whole pH range. *Electrochim. Acta* **2015**, 168, 256.

[40]. Wu, R.; Xu, Y.; Xu, R.; Huang, Y.; Zhang, B., Ultrathin-nanosheet-based 3D hierarchical porous In_2S_3 microspheres: chemical transformation synthesis, characterization, and enhanced photocatalytic and photoelectrochemical property. *J. Mater. Chem. A* **2015**, 3, 1930.

[41]. Yuan, J.; Wu, J.; Hardy, W. J.; Loya, P.; Lou, M.; Yang, Y.; Najmaei, S.; Jiang, M.; Qin, F.; Keyshar, K.; Ji, H.; Gao, W.; Bao, J.; Kono, J.; Natelson, D.; Ajayan, P. M.; Lou, J., Facile synthesis of single crystal vanadium disulfide nanosheets by chemical vapor deposition for efficient hydrogen evolution reaction. *Adv. Mater.* **2015**, 27, 5605.

[42]. Li, M.; Liu, X.; Xiong, Y.; Bo, X.; Zhang, Y.; Han, C.; Guo, L., Facile synthesis of various highly dispersive CoP nanocrystal embedded carbon matrices as efficient electrocatalysts for the hydrogen evolution reaction. *J. Mat. Chem. A.* **2015,** 3, 4255.

[43]. Tang, M. H.; Hahn, C.; Klobuchar, A. J.; Ng, J. W. D.; Wellendorff, J.; Bligaard, T.; Jaramillo, T. F., Nickel-silver alloy electrocatalysts for hydrogen evolution and oxidation in an alkaline electrolyte. *Phys. Chem. Chem. Phys.* **2014,** 16, 19250.

[44]. Tian, T.; Ai, L.; Jiang, J., Metal-organic framework-derived nickel phosphides as efficient electrocatalysts toward sustainable hydrogen generation from water splitting. *RSC Adv.* 5, **2015,** 10290.

[45]. Vesborg, P. C. K.; Seger, B.; Chorkendorff, I., Recent development in hydrogen evolution reaction catalysts and their practical implementation. *J. Phys. Chem. Lett.* 6, **2015,** 951.

[46]. Jaramillo, T. F.; Ivanovskaya, A.; McFarland, E. W., High-throughput screening system for catalytic hydrogen-producing materials. *J. Combinator. Chem.* **2002,** 4, 17.

[47]. Greeley, J.; Jaramillo, T. F.; Bonde, J.; Chorkendorff, I.; Norskov, J. K., Computational high-throughput screening of electrocatalytic materials for hydrogen evolution. *Nature Mater.* **2006,** 5, 909.

[48]. Bonde, J.; Moses, P. G.; Jaramillo, T. F.; Norskov, J. K.; Chorkendorff, I., Hydrogen evolution on nano-particulate transition metal sulfides. *Farad. Discuss.* **2009,** 140, 219.

[49]. Benck, J. D.; Chen, Z.; Kuritzky, L. Y.; Forman, A. J.; Jaramillo, T. F., Amorphous molybdenum sulfide catalysts for electrochemical hydrogen production: insights into the origin of their catalytic activity. *ACS Catal.* 2, **2012,** 1916.

[50]. Callejas, J. F.; McEnaney, J. M.; Read, C. G.; Crompton, J. C.; Biacchi, A. J.; Popczun, E. J.; Gordon, T. R.; Lewis, N. S.; Schaak, R. E., Electrocatalytic and photocatalytic hydrogen production from acidic and neutral-pH aqueous solutions using iron phosphide nanoparticles. *ACS Nano* 8, **2014,** 11101.

[51]. Deng, J.; Ren, P.; Deng, D.; Yu, L.; Yang, F.; Bao, X., Highly active and durable non-precious-metal catalysts encapsulated in carbon nanotubes for hydrogen evolution reaction. *Energy & Environ. Sci.* **2014,** 7, 1919.

[52]. Lv, H.; Xi, Z.; Chen, Z.; Guo, S.; Yu, Y.; Zhu, W.; Li, Q.; Zhang, X.; Pan, M.; Lu, G.; Mu, S.; Sun, S., A new core/shell NiAu/Au nanoparticle catalyst with Pt-like activity for hydrogen evolution reaction. *J. Am. Chem. Soc.* **2015,** 137, 5859.

Chapter 4

Metal/metal sulfide nanoparticles from metal thiolate precursors and their heterostructures

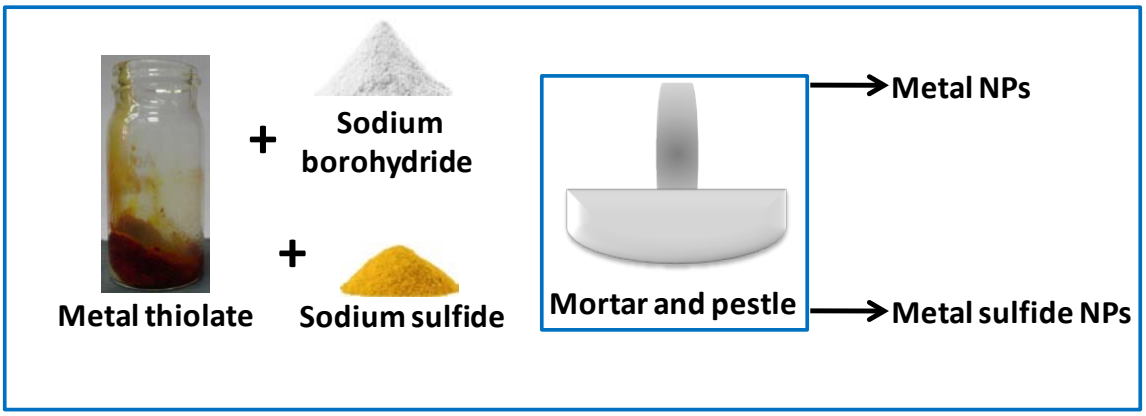

Monolayer protected nanoparticles have mainly two constituents; the inorganic metal/metal compound core and organic molecular shell. Noticing that the metal thiolates have these ingredients inbuilt in their structure, we envisaged them as good precursors to monolayer protected nanoparticles. This chapter describes the methods we developed to prepare metal, metal sulfide nanoparticles using the metal thiolates as precursors. Interestingly, the preparation of metal particles could be accomplished by a simple and convenient solid state route wherein grinding the metal thiolate and a reducing agent yielded monolayer protected metal nanoparticles that could be dispersed in a desired organic solvent. Similarly metal sulfide nanoparticles could also be prepared by this simple solid state route by crushing the metal thiolate with a sulfur source such as sodium sulfide in place of a reducing agent.

4.1 Introduction

Synthesis and characterization of metal/metal containing binary/ternary compound nanoparticles had been central to the nanoscience and nanotechnology field. A major proportion of the research was vastly devoted to the nanoparticle synthesis and characterization and their employment in diverse applications such as catalysis, fluorescent imaging, magnetism, energy generation and sensing [1-11]. Nanoparticles are even utilized in varied research fields to study fundamental phenomena such as microgravity [12] and superhydrophobic [13] nature of materials. This was all possible due to their existence as colloidal solutions or dispersions. The amount of knowledge on the nanoparticle synthesis and characterization accumulated over all these years is bewildering and even mystifying. Even today one of the most hot research topics of general interest among researchers including chemists, physicists, biologists and many other interdisciplinary scientists is the nanoparticles' synthesis, characterization, assembly, their properties and applications. Several established nanoparticle synthesis procedures exist in the literature, which are being practiced on a daily basis all over the research world [14-25].

Interestingly, though a plethora of reports appeared and keep on appearing on synthesizing the wide range of nanoparticles [26-29], the thirst and thrust for finding newer methods of nanoparticle preparations, especially those that can lead to large amounts of materials are the need of the hour. One particular mode of synthesis of metallic or metal based nanoparticles that interested us was the preparation of the metal or metal sulfide nanoparticles from their precursor materials in which all the ingredients of the final products are already included. The precursor materials could consist of several easily accessible chemicals like metal complexes constituted with varied ligands like thiols, amine, lipids, etc., among others [30-33]. Advantages of precursor based nanoparticles' syntheses were already harnessed to a great extent as is evident from the literature pertaining to the same that exists from several decades of nanoparticulate research.

Though reports on the precursor based nanoparticles' preparation are widely present in the literature [34-38], condensing the number of steps in the process of the synthesis and obtaining large quantities of the final product still remain elusive. The metal thiolates that we obtained in gram scale quantities looked very promising candidates and hence were tested for their utility as precursors for the synthesis of metal /metal sulfide nanoparticles. Again to further simplify the procedure these syntheses were accomplished through a simple single step solid state route devoid of any solvent usage. These results are presented and discussed in this chapter.

This chapter is divided into two parts. First part (Part A) introduces the synthetic procedures for the metal thiolates and then the preparation of metal/metal sulfide nanoparticles from these precursor compounds is described. The next part (part B) deals with the formation of heterostructures where the nanoparticles are decorated on nanosheets.

Part A

Part A deals with the metal/metal sulfide nanoparticles synthesis using sodium borohydride as the reducing agent and sodium sulfide as the sulfur source in case of metal sulfide NPs. Several metal thiolate precursors were employed to prepare metal/metal sulfide nanoparticles capped by precursor supplied *in situ* by the thiol ligands. This is dealt thoroughly in the following sections.

4.2 Synthesis of metal thiolates

As syntheses of palladium and lead thiolates were already discussed in the chapter 2 of this thesis, syntheses of the other metal thiolates utilized i.e., gold thiolates, silver thiolates, cadmium thiolates are only discussed here.

4.2.1 Synthesis of gold (I) thiolates

Gold (I) thiolates were synthesized in an easy manner to furnish gram scale quantities. Approximately 200 mg gold (I) iodide was taken in a glass vial. To this, 2 mL of n-

alkanethiol (n = 8, 10, 12, 16 and 18) was added and the reaction mixture was shaken vigorously. After sometime the color of this mixture changed to red. The resulting product was washed thoroughly with ethanol and dried to form powder. These powders are insoluble. The as obtained powders were characterized via techniques like TEM, powder XRD.

4.2.2 Synthesis of silver (I) thiolates

To 200 mg silver nitrate, 2 mL of n-alkanethiol (n = 8, 10, 12, 16 and 18) was added and the reaction mixture was shaken vigorously. The reaction mixture turned white. The mixture was then washed thoroughly with ethanol (5-6 times). The resulting product was washed thoroughly several times with ethanol and dried. The as obtained powders are insoluble and were characterized by techniques like TEM, powder XRD.

4.2.5 Synthesis of cadmium (II) thiolate

To 200 mg cadmium acetate, 2 mL of octanethiol was added and the reaction mixture was shaken vigorously. After sometime the color of this mixture changed to pale yellow. The resulting product was washed thoroughly several times with ethanol and dried and the resulting powders are slightly soluble in organic solvents such as toluene and were characterized using several characterization techniques like TEM, powder XRD.

4.3 Synthesis of metal nanoparticles from the metal thiolate precursors

Metal/metal sulfide nanoparticles from these metal thiolate nanosheets were synthesized through solid state grinding of the as obtained powdered metal thiolates with a reducing agent such as sodium borohydride or with a sulfur source such as sodium sulfide.

4.3.1 AuNPs from gold thiolate nanosheets

Au (I) octanethiolate was used as the precursor for the gold nanoparticles synthesis. 5 mg of the as prepared gold (I) octanethiolate + 45 mg of sodium borohydride were ground vigorously in a mortar with a pestle. Black color precipitate was obtained. The black precipitate was washed thoroughly with ethanol for 5-6 times and it was dried at ambient

conditions. The resulting powder was seen to disperse easily in non-polar organic solvent forming a red/purple colored clear dispersion. This same procedure was employed for preparing the gold nanoparticles from the other gold thiolates like gold (I) decanethiolate etc.

4.3.2 AgNPs from silver thiolate nanosheets

5 mg of Ag (I) octanethiolate, the precursor for the silver nanoparticles synthesis, was weighed out and was subjected to vigorous grinding in a mortar with a pestle with 45mg of sodium borohydride. Brown color precipitate was obtained. The precipitate was washed thoroughly with ethanol (5-6 times). It was dried at ambient conditions. Here too, the resulting powder was seen to form a brown colored clear dispersion. This same procedure was employed for preparing the silver nanoparticles from the other silver thiolates like silver (I) decanethiolate etc.

4.3.3 PdNPs from palladium thiolate nanosheets

5 mg of Pd (II) octanethiolate, the precursor for the palladium nanoparticles synthesis, was weighed out and was subjected to vigorous grinding in a mortar with a pestle with 45mg of sodium borohydride. Yellow color precipitate was obtained. The precipitate was washed thoroughly with ethanol (5-6 times). It was dried at ambient conditions. In this case the resulting powder formed a black dispersion in non-polar organic solvents. This same procedure was employed for preparing the palladium nanoparticles from the other palladium thiolates like palladium (I) decanethiolate etc.

4.3.4 PbS NPs from lead thiolate nanosheets

5 mg of Pb (II) octanethiolate was weighed out and was subjected to vigorous grinding in a mortar with a pestle with 45mg of sodium sulfide. Yellow color precipitate was obtained. The precipitate was washed thoroughly with ethanol (5-6 times). It was dried at ambient conditions. The resulting powder was dispersed in non-polar organic solvents and subjected to further analysis.

4.3.5 CdS NPs from cadmium thiolate nanosheets

5 mg of Cd (II) octanethiolate was weighed out and subjected to vigorous grinding in a mortar with a pestle with 45mg of sodium sulfide. Yellow color precipitate was obtained. The precipitate was washed thoroughly with ethanol (5-6 times). It was dried at ambient conditions. The resulting powder was seen to form clear dispersions in non-polar organic solvents.

4.3.6 Ag_2S NPs from silver thiolate nanosheets

5 mg of Ag (I) octanethiolate was weighed out and subjected to vigorous grinding in a mortar with a pestle with 45mg of sodium sulfide. Yellow color precipitate was obtained. The precipitate was washed thoroughly with ethanol (5-6 times). It was dried at ambient conditions. The resulting powder was dispersed in non-polar organic solvents and subjected to further analysis.

4.4 Results and Discussion

4.4.1 Gold nanosheets and gold nanoparticles

Powder XRD

The PXRD patterns of the gold (I) thiolates show periodically spaced *(00l)* reflections, revealing their lamellar structure (Figure 4.1). From PXRD patterns it can be noticed that as the chain length of these thiolate increases the (*001*) peak and all the other peaks following *(001)* such as *(002)* and *(003)* etc., shift to lower angle 2• value indicating increase in the 'd' value. Powder XRD of gold nanoparticles prepared by the solid state grinding method has also been recorded, that show peaks at 2• values, 38 and 43, corresponding to (111) and (200) gold planes respectively (Figure 4.2). Broad reflections confirm formation of gold in nanocrystalline form.

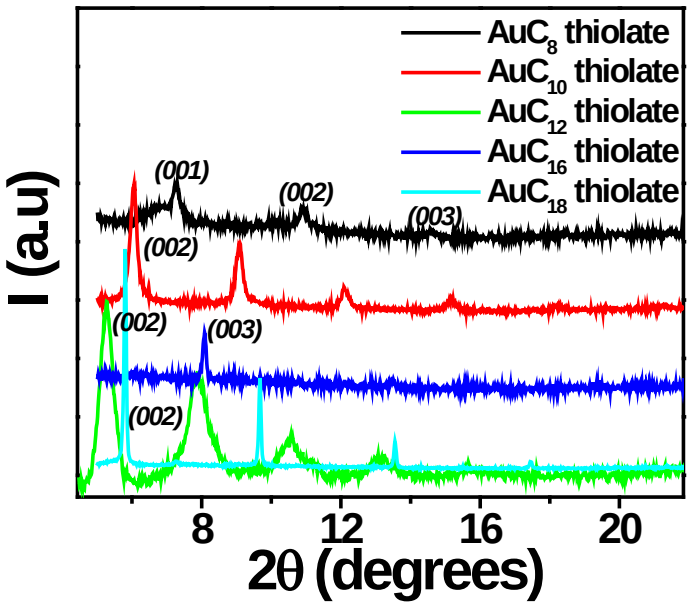

Figure 4.1: *Powder XRD spectra of gold (I) thiolates show (00l) reflections indicating layered structure in these thiolates.*

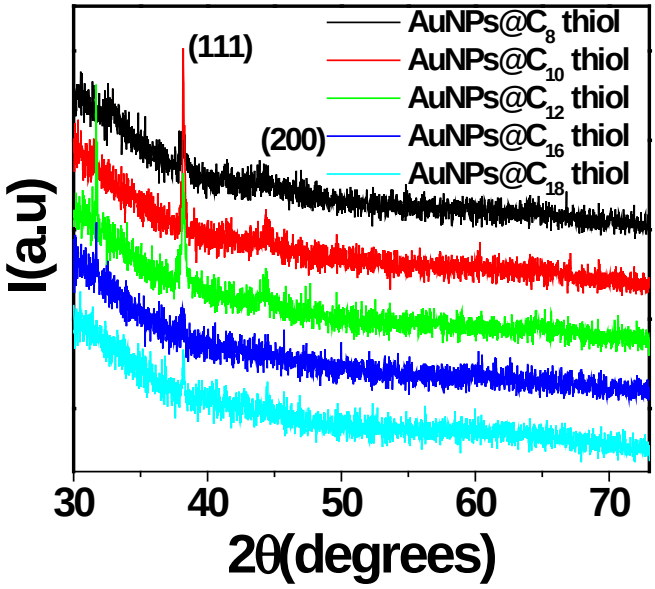

Figure 4.2: *PXRD spectra of gold nanoparticles formed from different gold (I) thiolates.*

UV-visible spectroscopy

The powder obtained by the solid state grinding of Au (I) thiolates with a reducing agent were dispersible in toluene. The UV-visible spectra obtained for gold nanoparticles dispersed in toluene display a peak at 530 nm (Figure 4.3). From this the formation of nanoparticles can be confirmed. Figure 4.4a shows the TEM images of the gold octanethiolate. As expected, the image shows sheet like structure on a TEM grid that is spread over micrometer length scales.

TEM analysis

The dispersions in toluene were drop cast on a TEM grid and TEM images of the same were recorded. Figure 4.4b shows TEM image for the gold nanoparticles from gold octanethiolate precursor obtained by the solid state synthetic route. It can be noticed that the particles are not well separated and have chain like connecting structures.

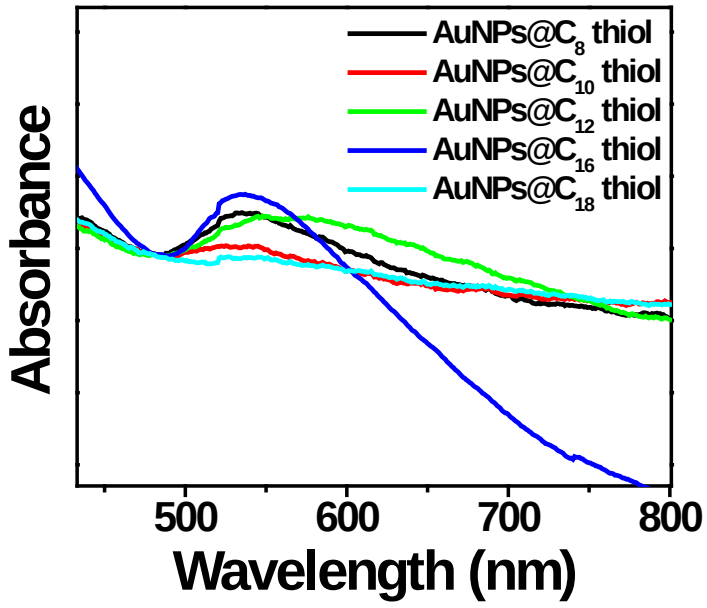

Figure 4.3: *UV-visible spectra of Au nanoparticles dispersed in toluene, which were prepared from different Au (I) thiolates.*

This was also true for the gold nanoparticles prepared from the other gold thiolates.

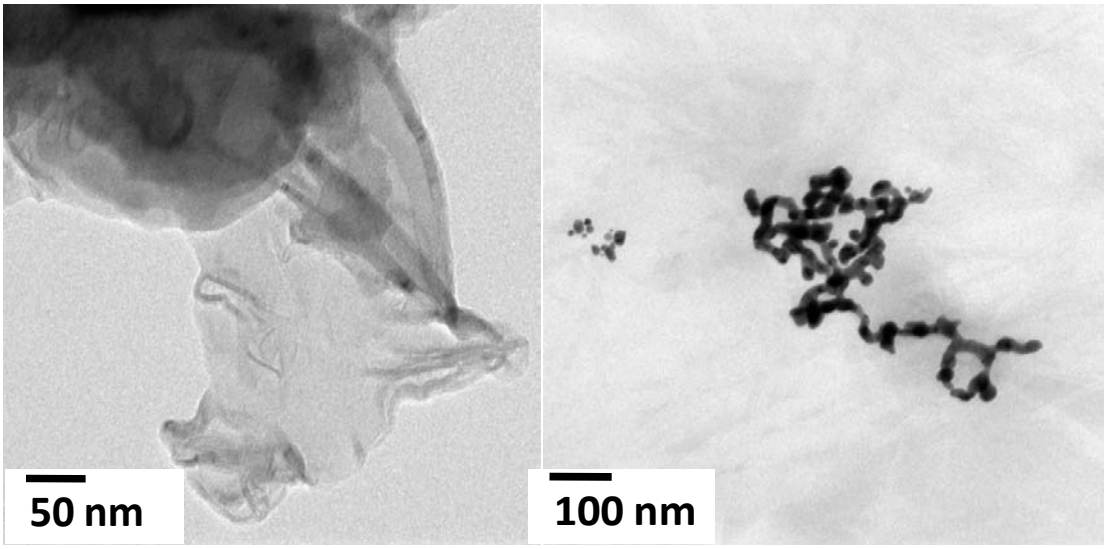

Figure 4.4: a) *TEM image of gold octanethiolate nanosheet.* ***b)*** *TEM image of gold nanoparticles prepared from gold octanethiolate.*

4.4.2 Silver nanosheets and silver nanoparticles

Silver thiolates were formed by mixing $AgNO_3$ and n-alkanethiols. All the silver thiolates resulted were white in color irrespective of number of carbon atoms in the alkyl chains. Utilizing these thiolates as precursors, silver nanoparticles were synthesized. All the as synthesized AgNPs were brown in color.

Powder XRD

PXRD patterns of silver thiolates show that they form sheet like structures, which can be clearly understood from the *(00l)* reflections that they display (Figure 4.5). Here again, as the chain length in the silver thiolates is increasing from octane to octadecane, the distance between the two sheets increases as is evident from the XRD 2• values. Powder XRD for the as prepared silver nanoparticles displayed in Figure 4.6 show metallic peaks for the silver nanoparticles at 2• = 38, 44, 64, 77 indicating that silver nanoparticles were prepared from their precursor silver thiolates. Here, it can be observed that the peak intensities are reduced in the case of the nanoparticles from AgC_{12} thiol and above.

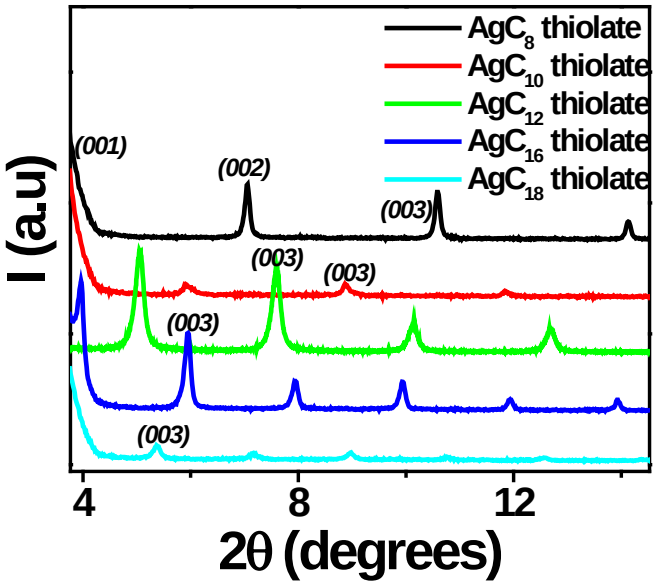

Figure 4.5: *Powder XRD spectra of silver (I) thiolates show lamellar reflections (00l).*

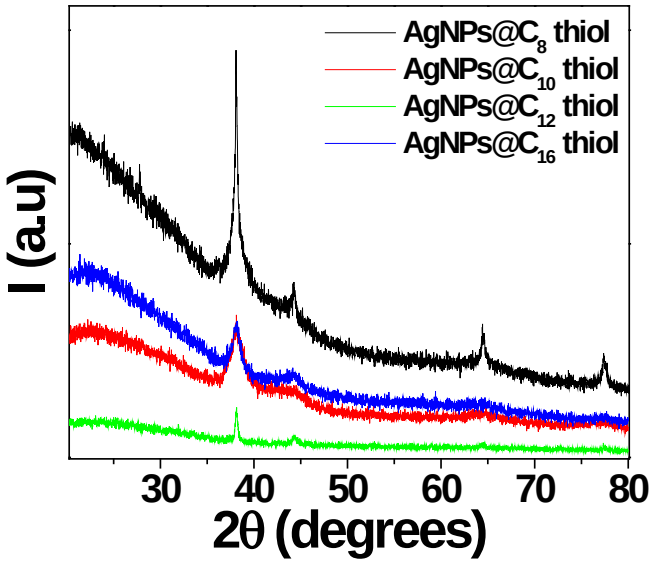

Figure 4.6: *Powder XRD spectra of silver nanoparticles prepared from silver thiolate precursors.*

UV-visible spectroscopy

The powders obtained from the solid state synthetic route formed dispersions with toluene. The UV-visible spectra recorded from these dispersions are shown in Figure 4.7. All these dispersions display a peak at 420 nm, which is characteristic of silver nanoparticles. As can be seen from UV-visible spectra nanoparticles prepared from AgC_{12} thiol and above (longer chain lengths) displayed an extra peak at 340 nm (Figure 4.7). In order to account for this special behavior, we checked for the XRD spectra and TEM images of the materials obtained from AgC_{12}, AgC_{16} and AgC_{18} thiolates after grinding them with $NaBH_4$. As discussed previously, the nanoparticles prepared from AgC_{12} thiol and onwards displayed reduced peak intensities and there was seen absence of a few peaks other than the first peak. It was noticed that in AgC_{12} to AgC_{18} thiolate cases even after they were ground with $NaBH_4$ periodically spaced lamellar peaks were present. At the same time they show good UV-visible peaks indicating nanoparticles formation. This could be attributed to the existence of unreacted thiolates in the reaction mixture. In the next attempt, we increased the amount of sodium borohydride; following which UV-visible and XRD spectra were recorded.

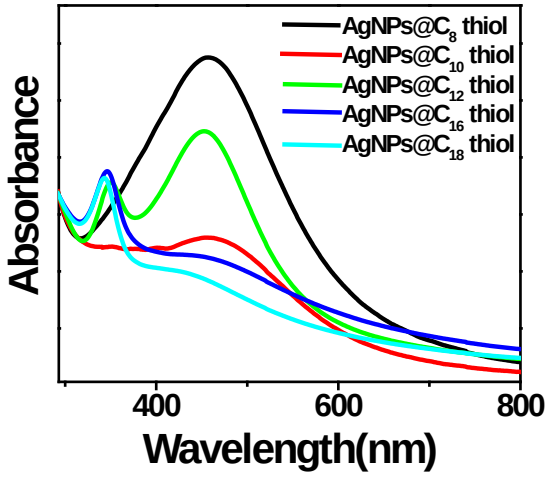

Figure 4.7: *UV-visible spectra of silver nanoparticles dispersed in toluene, which were obtained from different Ag (I) thiolates.*

The extra peaks in UV-visible and XRD were still observed from AgNPs@C_{12} thiol onwards even when they are ground with excess $NaBH_4$. So, we here propose the existence of a mixture of silver nanosheets and silver nanoparticles during the nanoparticle synthesis for the AgC_{12} thiolate precursor based silver nanoparticle formation and afterwards in the series. This is supported by the TEM images shown in Figure 4.10.

TEM analysis

The TEM images for silver thiolates are shown in Figure 4.8. Sheet like structure of silver (I) thiolate is clear from the image. The TEM images for silver nanoparticles are shown in Figure 4.9. In the case of AgNPs@C_8 thiol and AgNPs@C_{10} thiol where complete reduction of thiolates occurred as evidenced by the disappearance of the thiolate peaks in PXRD, the TEM images revealed presence of well separated particles that are spherical in shape. The particles are also nearly monodisperse in size. But in case of AgNPs@C_{12} thiol we can see the presence of a mixture of sheets and particles in the TEM images (Figure 4.10). This is expected because only partial reduction of the precursor seems to have occurred even when the amount of the reducing agent was increased to higher ratios, for example, AgC_{12} thiolate : $NaBH_4$ to 1 : 25.

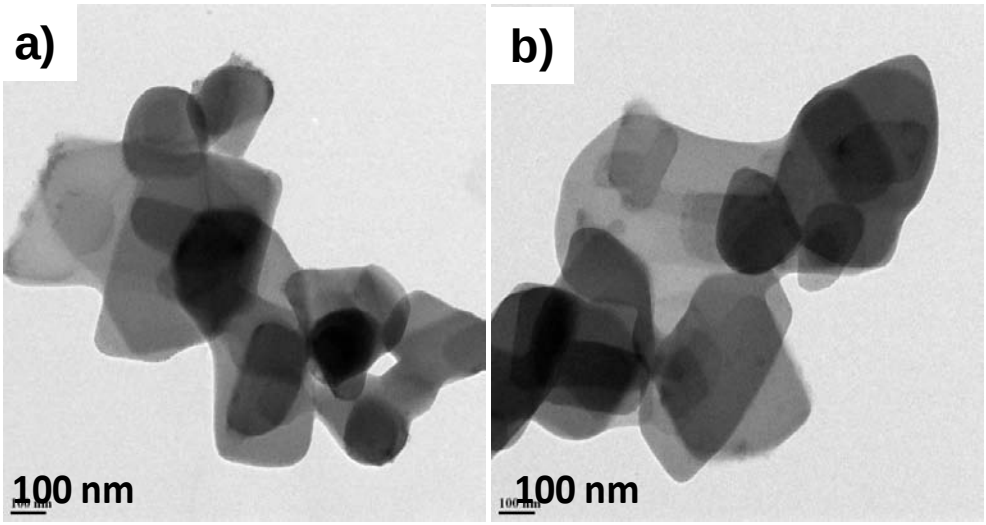

Figure 4.8: *TEM images of a) AgC_8 and b) AgC_{12} thiolates showing sheet like structure.*

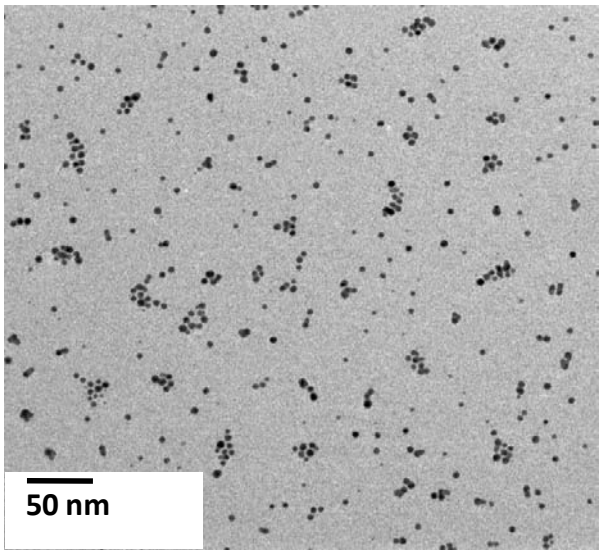

Figure 4.9: *TEM image of silver nanoparticles obtained by solid state reduction of Ag (I) octanethiolate.*

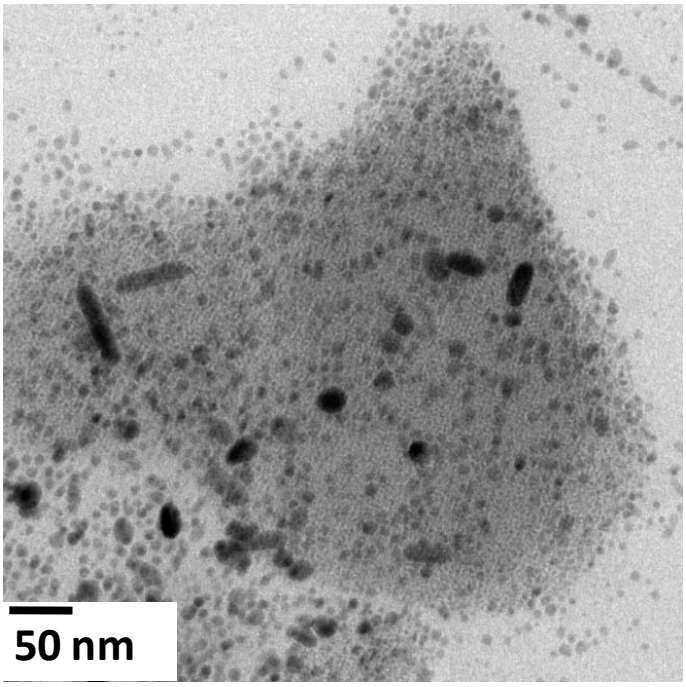

Figure 4.10: *TEM image of the product obtained after the solid state reduction of Ag (I) dodecanethiolate. Mixture of sheets and nanoparticles indicates partial reduction of silver dodecanethiolate.*

4.4.3 Palladium thiolates and palladium nanoparticles

Powder XRD

Powder XRD patterns for the palladium thiolates starting from palladium octanethiolate to palladium hexadecanethiolate are shown in Figure 4.11. Lamellar *(00l)* reflections from the powder XRD confirm the layered nature of these materials. Powder XRD pattern of palladium nanoparticles prepared from solid state grinding of the palladium octanethiolate precursor was collected and is represented in Figure 4.12, which shows no lamellar reflections but peaks representing palladium nanoparticles are also not significant.

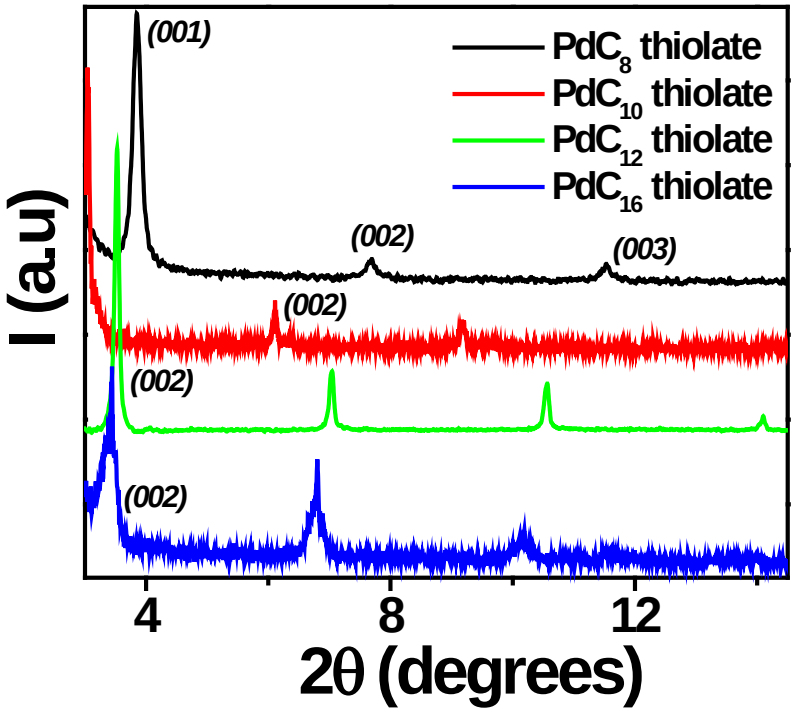

Figure 4.11: *Powder XRD of palladium thiolates.*

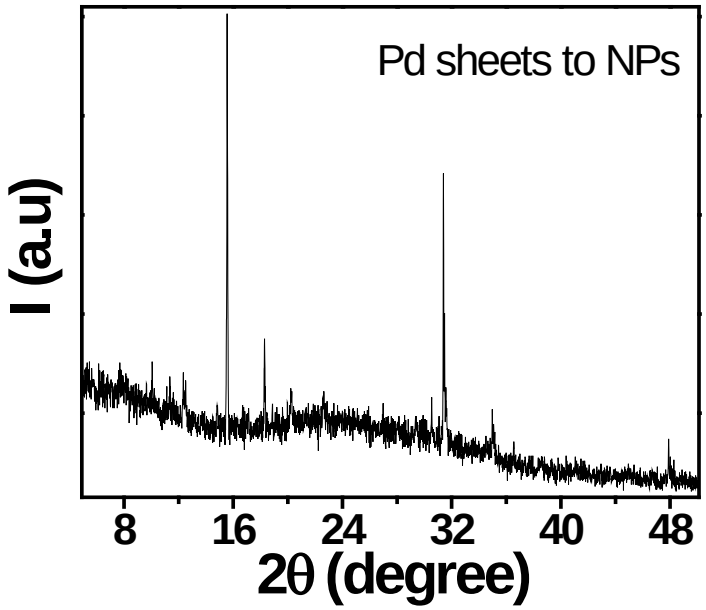

Figure 4.12: *Powder XRD of palladium nanoparticles prepared from PdC_8 thiolate.*

UV-visible spectroscopy

These palladium nanoparticles formed dispersions with toluene. The UV-visible spectra recorded for palladium nanoparticles dispersed in toluene are shown in Figure 4.13, and as expected there is no peak in the visible region of the spectra. Palladium nanoparticles prepared from palladium dodecanethiolate and palladium hexadecanethiolate precursors showed step like feature in the visible region around 400 nm in the UV-visible spectra. This could be an indication of the un-reacted palladium dodecane and hexadecane thiolates while grinding with sodium borohydride.

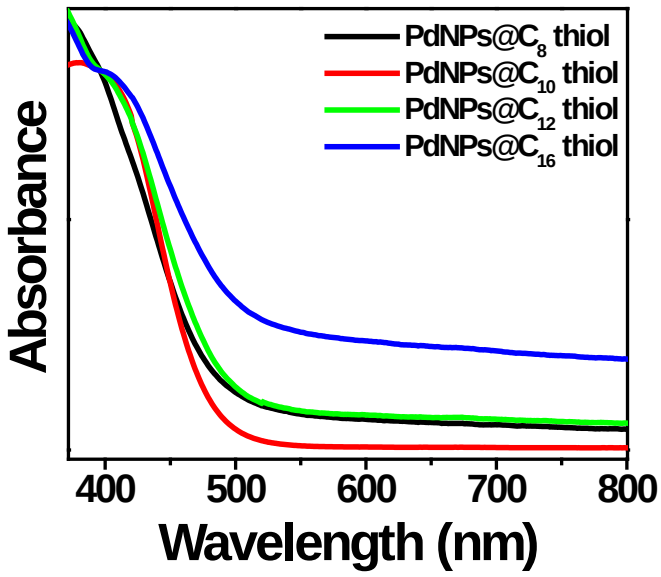

Figure 4.13: *UV-visible spectra of palladium nanparticles dispersed in toluene.*

These palladium nanoparticles were obtained by the solid state reduction of different Pd (II) thiolates.

TEM imaging

TEM images of palladium thiolates showed sheet like structures (Figure 4.14). These layered structures spread up to micrometer length scales laterally on the TEM grid. TEM images for the palladium nanoparticles resulting from the precursor palladium octanethiolate only were recorded. These palladium nanoparticle TEM images are depicted in Figure 4.15. These palladium nanoparticles displayed dendrite like architecture. Reports on such dendrite like nanoparticles prepared through chemical synthesis are seen in literature [39]. Similarly, these palladium nanoparticles existed as dendrite like structures at some places.

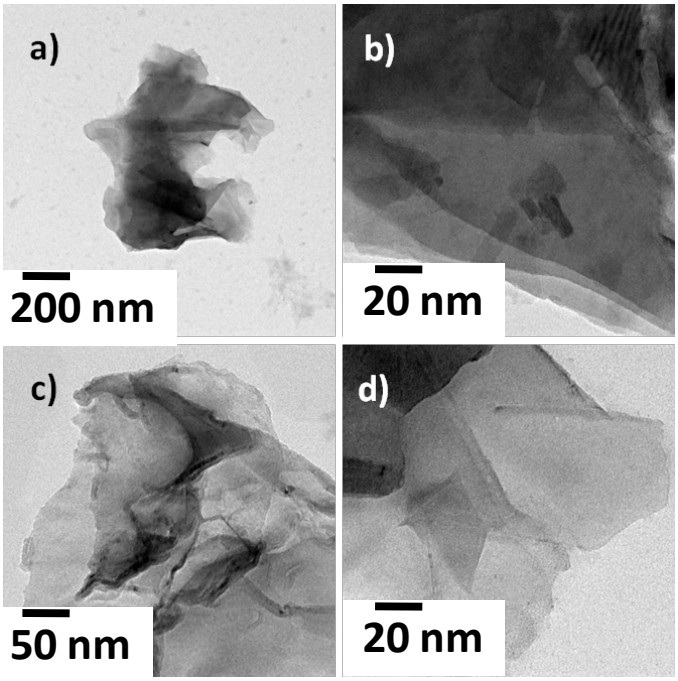

Figure 4.14: *TEM of palladium thiolates. a) palladium octanethiolate, b) palladium decanethiolate, c) palladium dodecanethiolate and d) palladium hexadecanethiolate.*

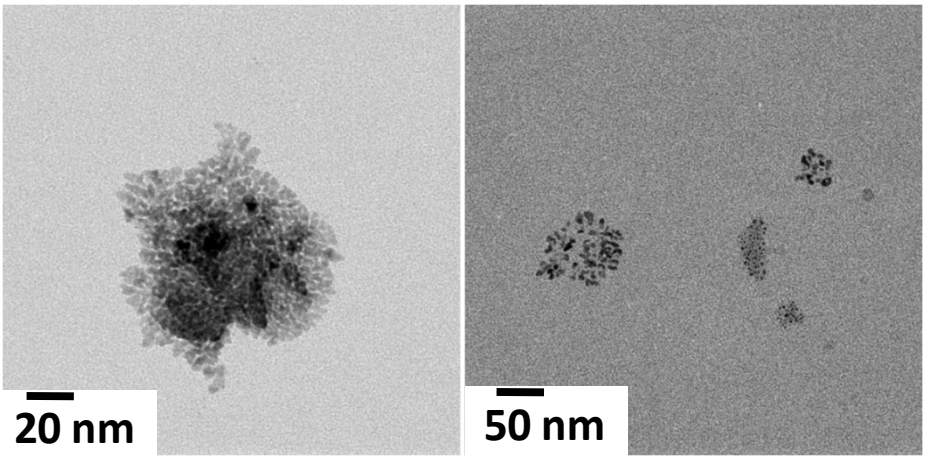

Figure 4.15: *TEM of palladium nanoparticles prepared from palladium octanethiolate precursor by the solid state reduction route.*

4.5 Synthesis of metal sulfide NPs from the metal thiolate precursors

Similar to the metal nanoparticle preparations described above, metal sulfide nanoparticles were synthesized from metal thiolate precursors. The metal thiolate precursors selected for these syntheses were silver octanethiolate, lead octanethiolate and cadmium octanethiolate. The synthetic procedures are described clearly in the synthesis section above. Here results will be discussed.

4.5.1 Silver sulfide nanoparticles from silver octanethiolate precursor

Silver sulfide nanoparticles from silver octanethiolate precursor were prepared by employing solid state route via crushing the silver (I) octanethiolate with sodium sulfide using a mortar and pestle.

Powder XRD

Powder XRD patterns for the silver octanethiolate and silver sulfide nanoparticles are depicted in Figure 4.16. Silver octanethiolate showed the expected lamellar *(00l)* reflections. Silver sulfide nanoparticles showed typical powder XRD pattern which when compared with the standards (JCPDS: 14-72) indicated the formation of • -phase of Ag_2S nanoparticles.

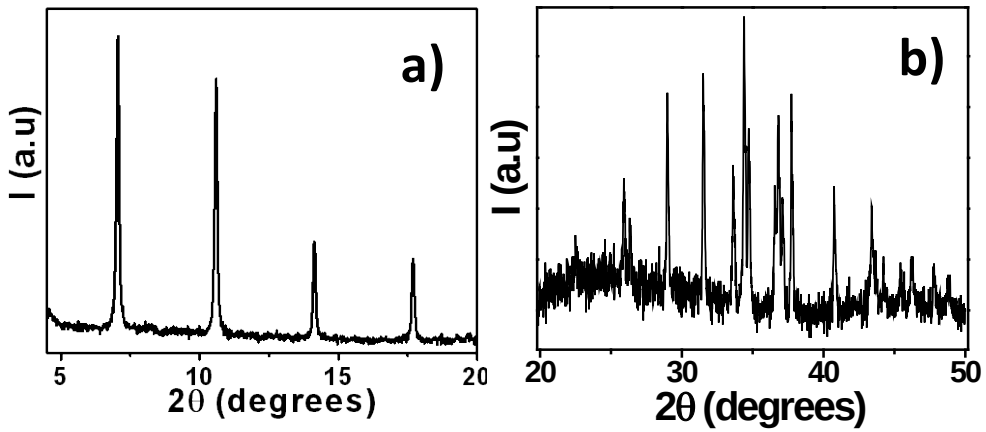

Figure 4.16: *PXRD of a) silver octanethiolate precursor and b) silver sulfide nanoparticles.*

TEM imaging

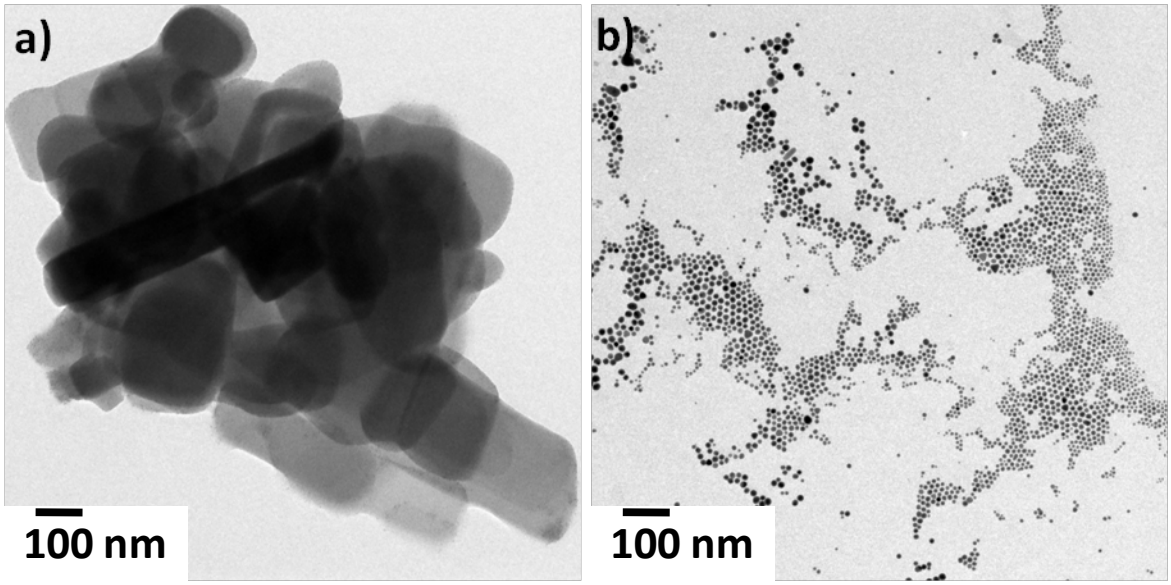

Figure 4.17: *TEM of a) silver octanethiolate precursor and b) silver sulfide nanoparticles.*

TEM for the silver octanethiolate and silver sulfide nanoparticles are depicted in Figure 4.17. As can be seen from the Figure 4.17b, silver sulfide nanoparticles are well separated and nearly monodisperse.

4.5.2 Lead sulfide nanoparticles from lead octanethiolate precursor

Figure 4.18a shows powder XRD pattern for the lead octanethiolate precursor and Figure 4.18b shows the lead sulfide nanoparticles. By comparing this PXRD pattern with the standard JCPDS (JCPDS: 05-0592) we could conclude the formation of galena phase lead sulfide.

TEM imaging for both the lead octanethiolate precursor and lead sulfide nanoparticles were depicted in Figure 4.19. As is evident from the Figure 4.19, lead octanethiolate displayed layered structure in the TEM image while the lead sulfide nanoparticles displayed nanoparticles with well separated spherical nearly monodisperse morphology.

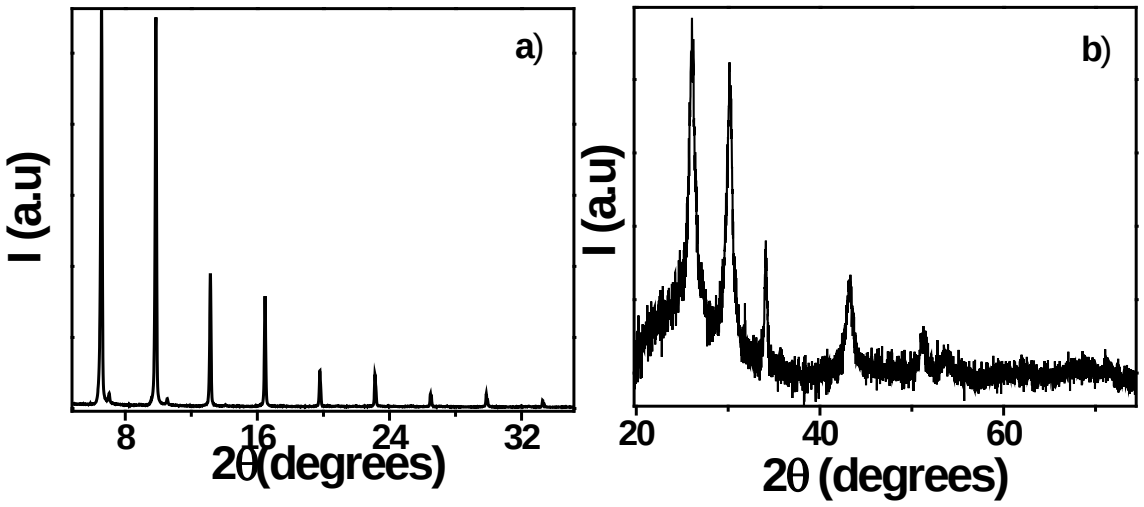

Figure 4.18: *PXRD of a) lead octanethiolate precursor and b) lead sulfide nanoparticles.*

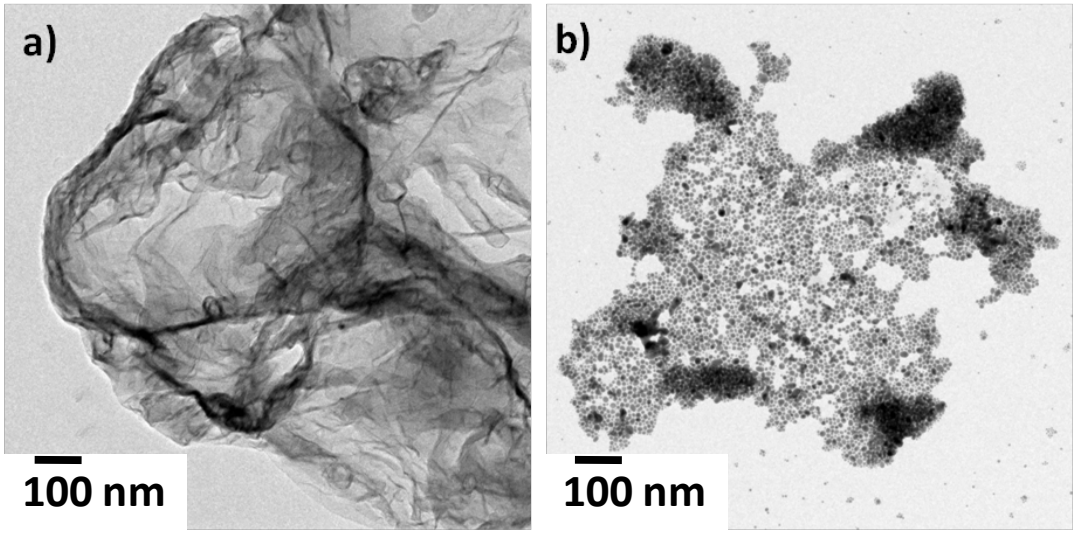

Figure 4.19: *TEM of a) lead octanethiolate precursor and b) lead sulfide nanoparticles.*

4.5.3 Cadmium sulfide nanoparticles from cadmium octanethiolate precursor

Cadmium sulfide nanoparticles were also prepared by following the same solid state grinding of the cadmium octanethiolate precursor in a mortar with a pestle with sodium sulfide. Depicted down are the powder XRD and TEM characterization for both the cadmium octanethiolate precursor and cadmium sulfide nanoparticles.

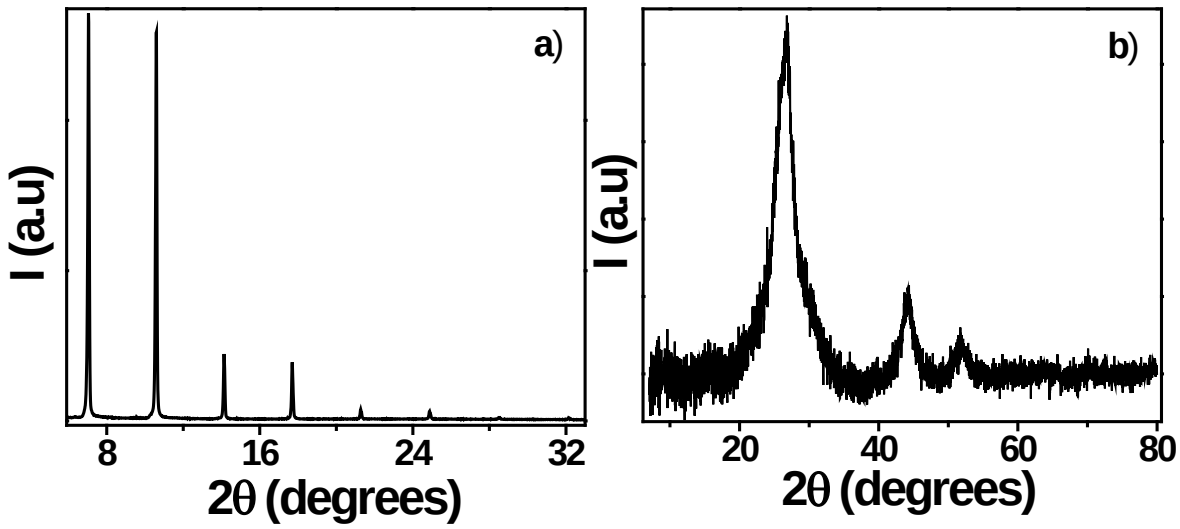

Figure 4.20: *PXRD of a) cadmium octanethiolate precursor and b) cadmium sulfide nanoparticles.*

Figure 4.20 above represents the powder XRD patterns for both the cadmium octanethiolate and the cadmium sulfide nanoparticles prepared from cadmium octanethiolate. PXRD for cadmium octanethiolate shows lamellar (00l) reflections indicating layered nature of the compound. PXRD of cadmium sulfide nanoparticles showed broad peaks indicating nanoparticle formation which is also comparable to that of the standard (JCPDS: 42-1411) cubic structure for CdS nanoparticles.

TEM image for cadmium octanethiolate showed sheet like structures as is evident from Figure 4.21a, in accordance with the powder XRD. For the cadmium sulfide nanoparticles, TEM image showed well ordered and separated monodisperse spherical nanoparticles as is evident from Figure 4.21b.

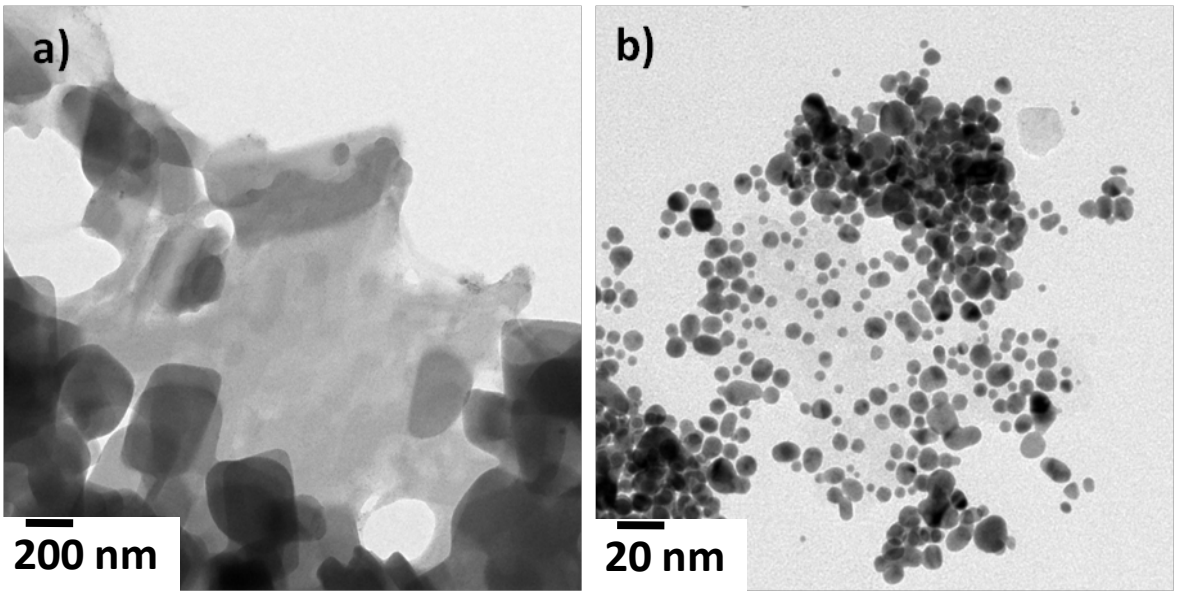

Figure 4.21: *TEM of a) cadmium octanethiolate precursor and b) cadmium sulfide nanoparticles.*

Part A conclusions:

In summary, the results presented in part A disclose the ease with which metal and metal sulfide nanoparticles could be prepared from the precursor metal thiolate nanosheets. Metal nanoparticles such as gold, silver and palladium nanoparticles were prepared from their precursor compounds such as gold thiolates, silver thiolates and palladium thiolates. This was performed through solid state crushing route employing mortar and pestle. Only one more reagent, the reducing agent or sodium sulfide (sulfur source) was utilized in this synthetic protocol. Thus preparation of metal/metal sulfide nanoparticles capped by *in vivo* precursor supplied thiol ligands was developed as a new methodology.

Part B

Part B deals with the formation of heterostructures from the as prepared nanoparticles on the as prepared nanosheets. Some examples are discussed below using just TEM imaging to show the heterostructure formation.

4.6 Metal nanoparticles on Palladium octanethiolate nanosheets

There is a recent surge in developing methods for the formation and characterization of heterostructures [40-42]. These heterostructures could be formed with two or more different nanosheets such as graphene, MoS_2, WS_2 etc. Another heterostructure system that is gaining popularity is the 'nanoparticles on nanosheets' binary heterostructure system [43-48]. Such heterostructures have important applications in several technologies [49-54]. Semiconductor heterostructures were widely studied once in the name of heterojunctions [55, 56]. But preparing these heterostructures through elegant ways such as simple solvent mixing of different species was not prevalent in the past. After the discovery/rediscovery of graphene and other two dimensional materials, research is being done again at a rapid phase on these heterostructures.

Motivation of carrying out the experiments described in this part was to develop solution based routes to the preparation of heterostructures utilizing soluble metal thiolate layers. Towards achieving this target, we first employed nanoparticles prepared in conventional methods such as citrate reduction method and mixed their dispersions in water with the metal thiolate nanosheet dispersions in toluene to form an aqueous-organic interface [57-59]. At this interface, by simple magnetic stirring, reaction occurred leading to anchoring of nanoparticles on to the nanosheets. We provide a brief description of this method by taking the example of silver nanoparticles on palladium octanethiolate nanosheets. Silver nanoparticles prepared from citrate reduction method dispersed in water were gently drop casted from a pipette into the reaction vessel containing the palladium octanethiolate nanosheets dissolved in toluene. Then, as soon as the stirring of the reaction mixture starts, interfacial mixing of the constituents of the two solvents occurred.

Then the stirring is allowed for about one hour with the hope that uniform mixing of the nanoparticle and nanosheets mixture occurs. The reaction when stopped and kept as it is without any disturbance for some time looked clear in the bottom water phase, indicating transfer of all the nanoparticles to the toluene phase where the palladium octanethiolate nanosheets were present. Figure 4.22 below gives a glimpse of the interfacial reaction. Figure 4.22a represents the reaction mixture before the start of the reaction. Although water is denser than toluene, here since palladium nanosheets in toluene were taken first into the reaction vessel and then to it the silver nanoparticles dispersed in water are added gently, the toluene phase appears at bottom and water phase on top. But after the reaction is done, clear water is seen at the bottom in accordance to the density laws.

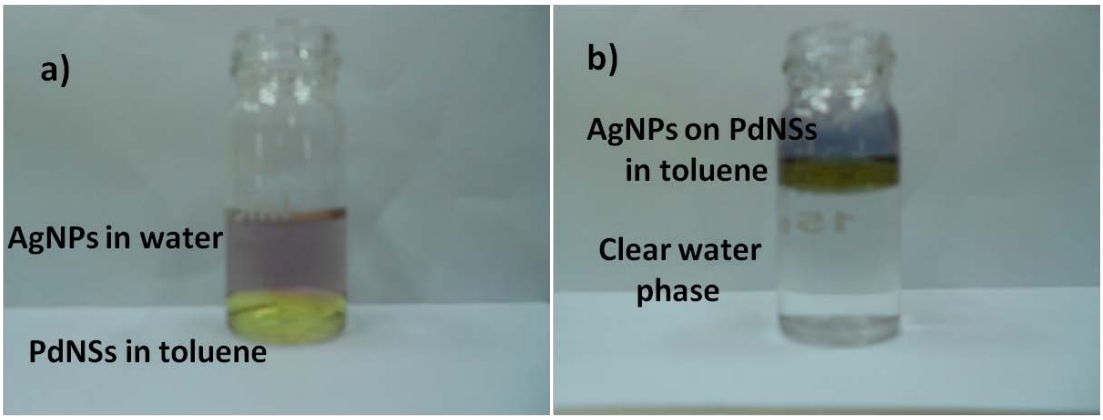

Figure 4.22: *Interfacial reaction leading to nanoparticles on nanosheets heterostructures. a) Ag nanoparticles dispersed in water just after gently mixing with palladium octanethiolate dissolved in toluene. b) After the interfacial mixing, phase-transfer of the silver nanoparticles to the toluene phase was seen where the silver nanoparticles decorate the nanosheets.*

One can see that the silver nanoparticles are mostly residing only on the palladium octanethiolate nanosheets and less present outside the nanosheets (Figure 4.23). In some cases, these nanoparticles are even embedded in between two nanosheets. Such embedded systems might have much stronger implications for both fundamental and application related research on such heterostructures.

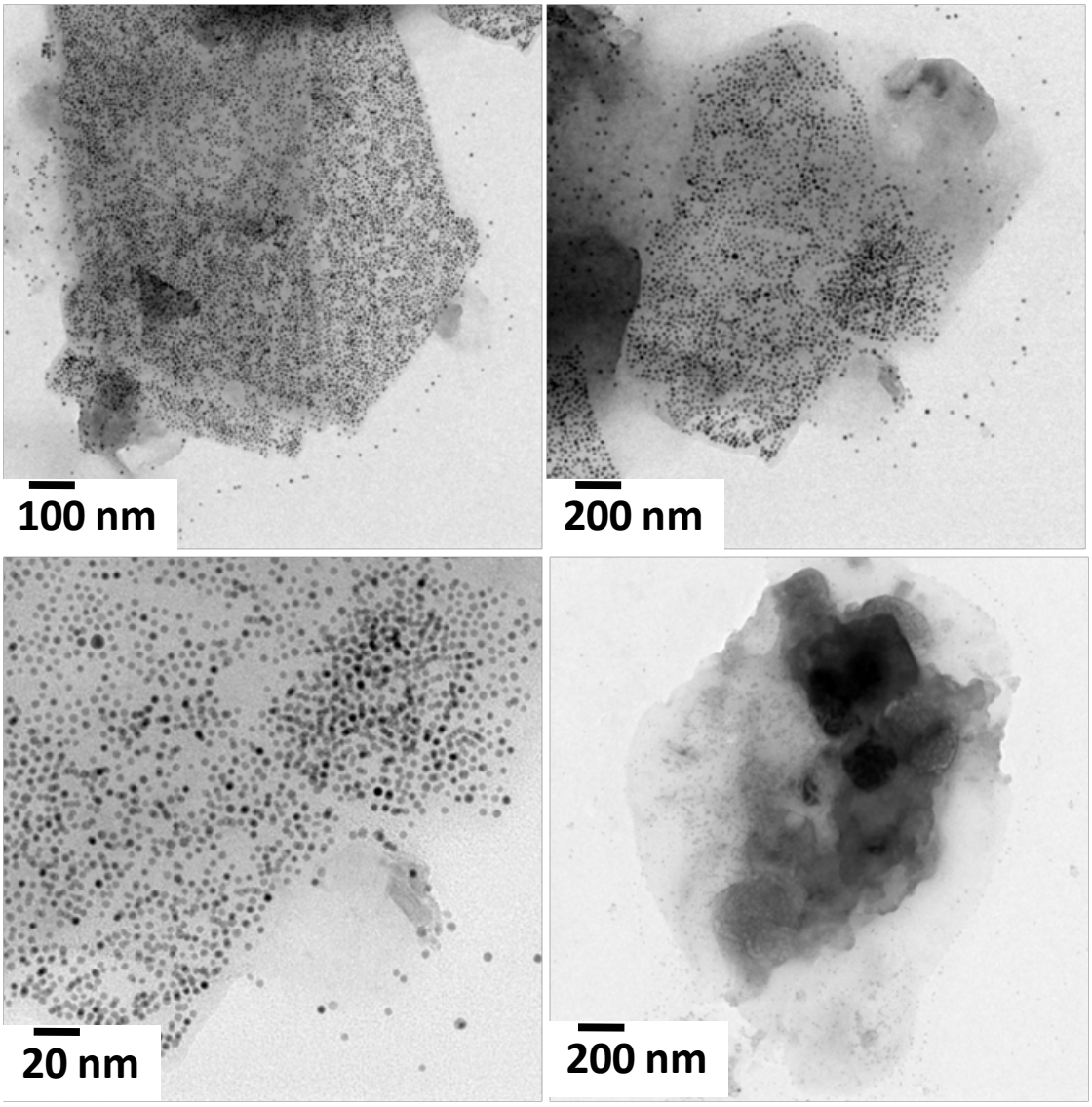

Figure 4.23: *TEM of silver nanoparticles, synthesized via citrate reduction of silver nitrate, on palladium octanethiolate nanosheets.*

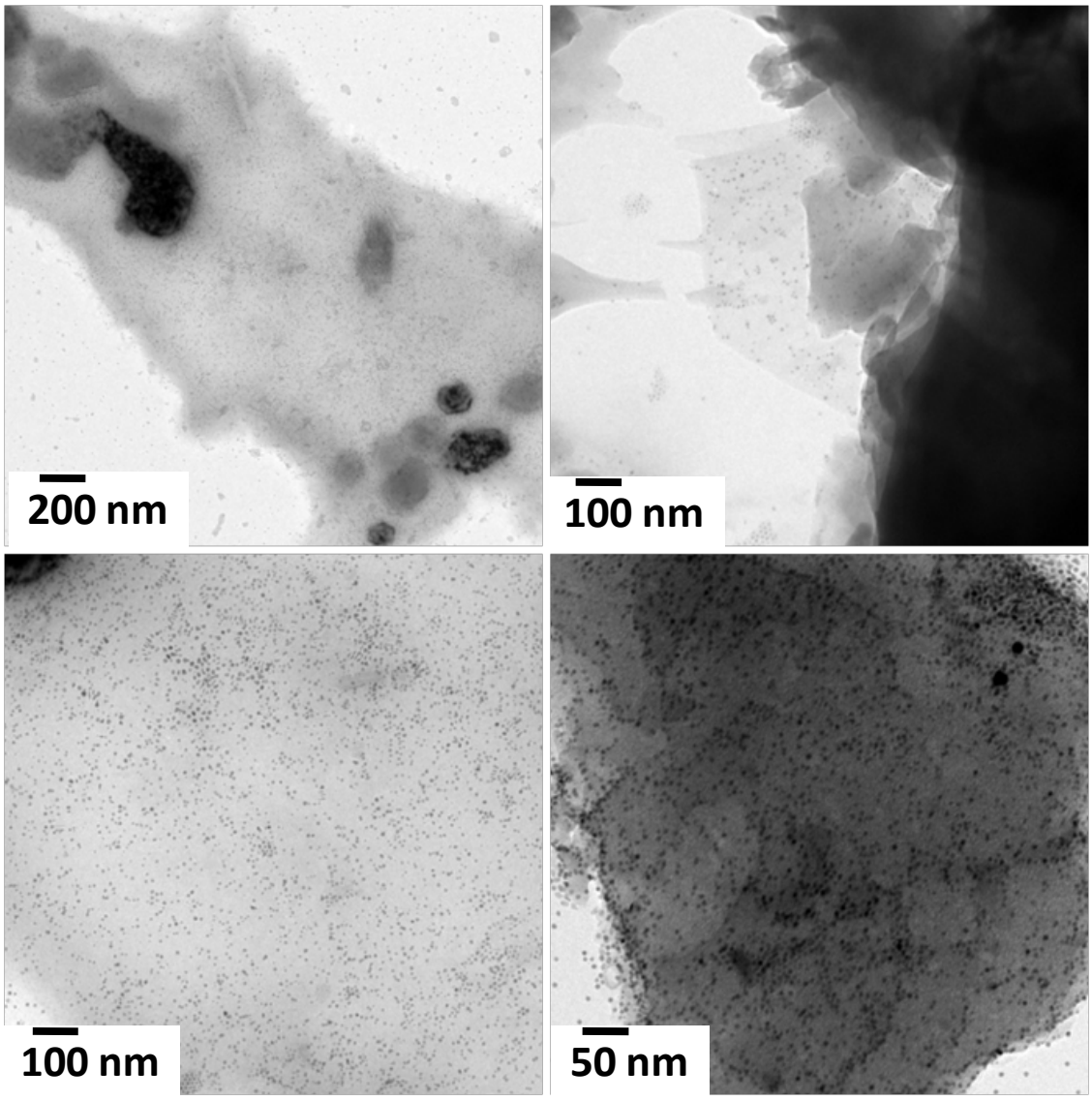

Figure 4.24: *TEM of silver nanoparticles, synthesized from silver octanethiolate precursor, on palladium octanethiolate nanosheets.*

Not surprisingly, silver/palladium/gold nanoparticles prepared from silver octanethiolate/palladium octanethiolate/gold octanethiolate through the solid state grinding when mixed with palladium octanethiolate nanosheets (both these were dispersed in toluene) also arranged themselves on the nanosheet in an orderly manner as is evident from the above Figures 4.24 & 4.25 & 4.26 & 4.27. Nanoparticles formed arrays along the borders of the nanosheets and also are present as agglomerations above the nanosheets.

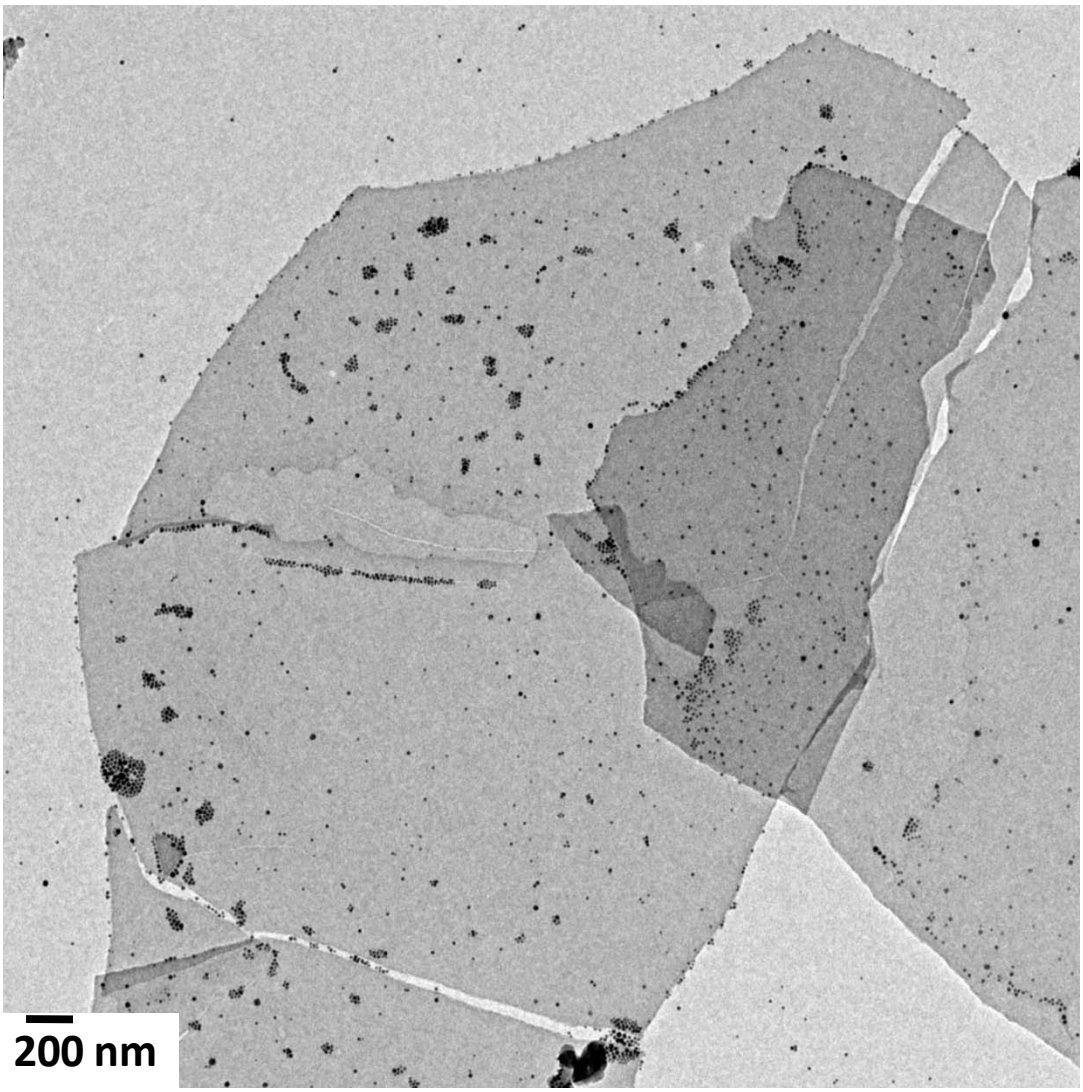

Figure 4.25: *TEM of palladium nanoparticles, synthesized from palladium octanethiolate precursor, on palladium octanethiolate nanosheets.*

Possible interactions between the nanoparticles and the nanosheets could be deduced from the van der Waals attractive-repulsive interactions between the alkyl chains of the interacting thiols moieties that are present both in the nanoparticles and in the nanosheets as surfactants.

At some parts on the nanoparticles decorated nanosheets, the nanoparticles get themselves arranged in specific morphologies as is evident from Figure 4.26 below. In the Figure 4.26, gold nanoparticles arrange themselves in specific orientation on the palladium octanethiolate nanosheet in hexagonal packed array. These nanoparticles hinge on the edge of the nanosheet.

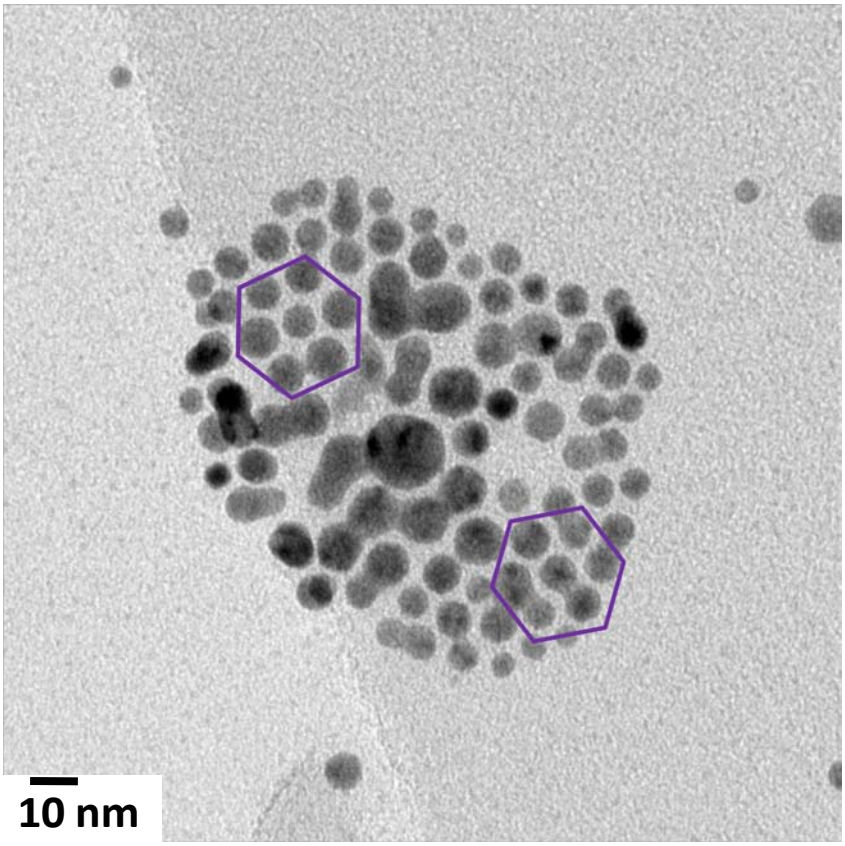

Figure 4.26: *TEM of gold nanoparticles, synthesized from gold octanethiolate precursor, on palladium octanethiolate nanosheets. Here, the nanoparticles hinge on the edge of the palladium octanethiolate nanosheet. Also these nanoparticles arrange themselves into ordered hexagonal arrays.*

Figure 4.27 represents some more TEM images of the nanoparticle-nanosheet heterostructures where on some nanosheets linear arrays of nanoparticles are observed. These observations give motivation and scope for further investigations on such heterostructures.

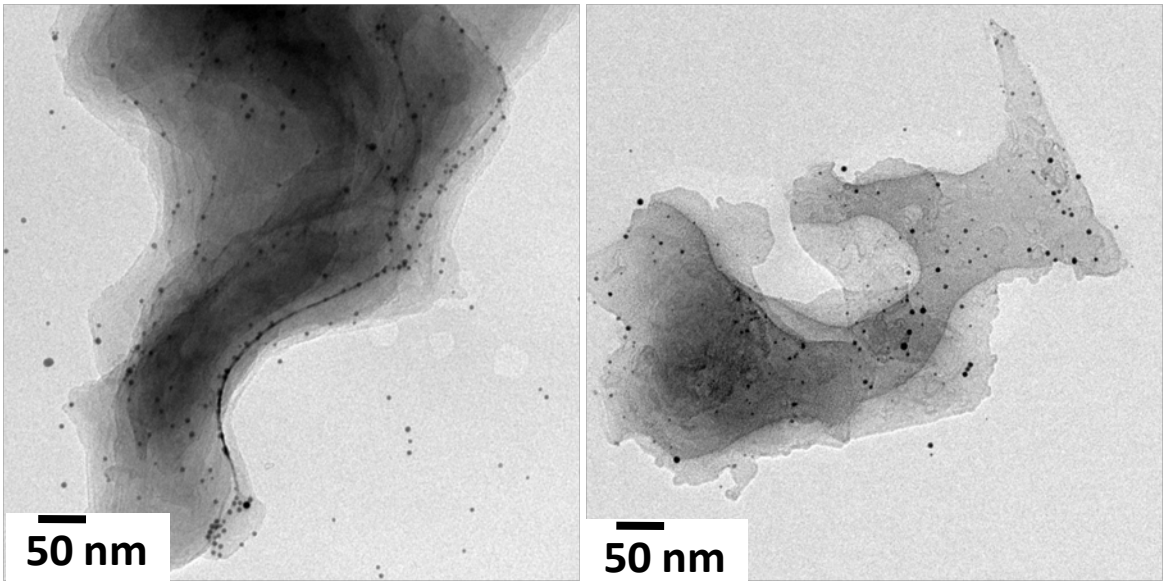

Figure 4.27: *TEM of gold nanoparticles on palladium octanethiolate nanosheets.*

Part B conclusions

Heterostructures from metal nanoparticles anchored to flat metal thiolate nanosheets have been realized just by mixing the nanoparticle dispersions either in water or toluene with nanosheets solution in toluene. Several interesting arrangements of the nanoparticles on the nanosheets were observed. Though this part just showed TEM imaging to confirm the heterostructures, several combinatorial arrangements of nanoparticles on nanosheets could pave a newer path to study these arrays further with much vigor.

4.7 Conclusions

A series of metal thiolates have been prepared in gram scale quantities. These metal (I) thiolates have shown sheet like morphology. However, except palladium thiolates the other thiolates were not readily soluble in any of polar and non-polar solvents. The metal thiolate nanosheets were then utilized as precursors for the metal/metal sulfide nanoparticle synthesis. We showed that this nanoparticle synthesis could be carried out using just another reagent such as a reducing agent like sodium borohydride or with a sulfur source like sodium sulfide because the other reagents such as a metal/metal ion precursor and a surfactant to be used as a capping agent to stabilize the as formed nanoparticles are all present in the precursor metal thiolate complex itself. Cashing on this advantage we could prepare a series of metal/metal sulfide nanoparticles such as gold, silver and palladium nanoparticles and also silver sulfide, lead sulfide and cadmium sulfide nanoparticles.

The as prepared nanoparticles are extensively characterized using powder XRD, UV-visible spectroscopy and TEM imaging. The as formed nanoparticles could form dispersions with certain solvents.

In the second part of this chapter, the as formed metal nanoparticles dispersed in water were simply mixed with the palladium octanethiolate nanosheets solution in toluene and the interfacial reaction resulted in nanoparticle-nanosheet heterostructures, which was confirmed from the TEM imaging. Thus this chapter dealt with the metal/metal sulfide nanoparticles synthesis from their precursor metal thiolates and then presented on the nanoparticle-nanosheet heterostructures.

4.8 References

[1]. Nirmal, M.; Dabbousi, B. O.; Bawendi, M. G.; Macklin, J. J.; Trautman, J. K.; Harris, T. D.; Brus, L. E., Fluorescence intermittency in single cadmium selenide nanocrystals. *Nature* **1996,** 383, 802.

[2]. Kodama, R. H., Magnetic nanoparticles. *J. Magn. Magn. Mater.* **1999,** 200, 359.

[3]. Shen, S.; Wang, Q., Rational Tuning the optical properties of metal sulfide nanocrystals and their applications. *Chem. Mater.* **2013,** 25, 1166.

[4]. Ito, A.; Shinkai, M.; Honda, H.; Kobayashi, T., Medical application of functionalized magnetic nanoparticles. *J. Biosci. Bioeng.* **2005,** 100, 1.

[5]. Gangopadhyay, P.; Gallet, S.; Franz, E.; Persoons, A.; Verbiest, T., Novel superparamagnetic core(shell) nanoparticles for magnetic targeted drug delivery and hyperthermia treatment. *IEEE Trans. Magn.* **2005,** 41, 4194.

[6]. Haruta, M., Catalysis: Gold rush. *Nature* **2005,** 437, 1098.

[7]. Gobin, A. M.; Lee, M. H.; Halas, N. J.; James, W. D.; Drezek, R. A.; West, J. L., Near-infrared resonant nanoshells for combined optical imaging and photothermal cancer therapy. *Nano Lett.* **2007,** 7, 1929.

[8]. Verma, A.; Uzun, O.; Hu, Y.; Hu, Y.; Han, H.-S.; Watson, N.; Chen, S.; Irvine, D. J.; Stellacci, F., Surface-structure-regulated cell-membrane penetration by monolayer-protected nanoparticles. *Nature Mater.* **2008,** 7, 588.

[9]. Benck, J. D.; Hellstern, T. R.; Kibsgaard, J.; Chakthranont, P.; Jaramillo, T. F., Catalyzing the hydrogen evolution reaction (HER) with molybdenum sulfide nanomaterials. *ACS Catal.* **2014,** 4, 3957.

[10]. Bonde, J.; Moses, P. G.; Jaramillo, T. F.; Norskov, J. K.; Chorkendorff, I., Hydrogen evolution on nano-particulate transition metal sulfides. *Faraday Discussions* **2009,** 140, 219.

[11]. Boal, A. K.; Ilhan, F.; DeRouchey, J. E.; Thurn-Albrecht, T.; Russell, T. P.; Rotello, V. M., Self-assembly of nanoparticles into structured spherical and network aggregates. *Nature* **2000,** 404, 746.

[12]. Reed, J. A.; Cook, A.; Halaas, D. J.; Parazzoli, P.; Robinson, A.; Matula, T. J.; Grieser, F., The effects of microgravity on nanoparticle size distributions generated by the ultrasonic reduction of an aqueous gold-chloride solution. *Ultrasonics Sonochemistry* **2003,** 10, 285.

[13]. Ogihara, H.; Xie, J.; Okagaki, J.; Saji, T., Simple method for preparing superhydrophobic paper: spray-deposited hydrophobic silica nanoparticle coatings exhibit high water-repellency and transparency. *Langmuir* **2012,** 28, 4605.

[14]. Kasture, M.; Singh, S.; Patel, P.; Joy, P. A.; Prabhune, A. A.; Ramana, C. V.; Prasad, B. L. V., Multiutility sophorolipids as nanoparticle capping agents: synthesis of stable and water dispersible Co nanoparticles. *Langmuir* **2007,** 23, 11409.

[15]. Rogach, A. L.; Kornowski, A.; Gao, M. Y.; Eychmuller, A.; Weller, H., Synthesis and characterization of a size series of extremely small thiol-stabilized CdSe nanocrystals. *J. Phys. Chem. B* **1999,** 103, 3065.

[16]. Sarathy, K. V.; Kulkarni, G. U.; Rao, C. N. R., A novel method of preparing thiol-derivatised nanoparticles of gold, platinum and silver forming superstructures. *Chem. Commun.* **1997,** 6, 537.

[17]. Zhang, C.; Zhang, S.; Yu, L.; Zhang, Z.; Zhang, P.; Wu, Z., Size-controlled synthesis of monodisperse Ag_2S nanoparticles by a solventless thermolytic method. *Materials Letters* **2012,** 85, 77.

[18]. Zhuang, Z.; Lu, X.; Peng, Q.; Li, Y., A facile "dispersion–decomposition" route to metal sulfide nanocrystals. *Chem. Euro. J.* **2011,** 17, 10445.

[19]. Zhuang, Z.; Peng, Q.; Wang, X.; Li, Y., Tetrahedral colloidal crystals of Ag_2S nanocrystals. *Angewandte Chemie* **2007,** 119, 8322.

[20]. Park, J.; An, K. J.; Hwang, Y. S.; Park, J. G.; Noh, H. J.; Kim, J. Y.; Park, J. H.; Hwang, N. M.; Hyeon, T., Ultra-large-scale syntheses of monodisperse nanocrystals. *Nature Mater.* **2004,** 3, 891.

[21]. Du, X.-S.; Mo, M.; Zheng, R.; Lim, S.-H.; Meng, Y.; Mai, Y.-W., Shape-controlled synthesis and assembly of copper sulfide nanoparticles. *Cryst. Growth & Des.* **2008,** 8, (6), 2032.

[22]. Cushing, B. L.; Kolesnichenko, V. L.; O'Connor, C. J., Recent advances in the liquid-phase syntheses of inorganic nanoparticles. *Chem. Rev.* **2004,** 104, 3893.

[23]. Du, Y.; Yin, Z.; Zhu, J.; Huang, X.; Wu, X.-J.; Zeng, Z.; Yan, Q.; Zhang, H., A general method for the large-scale synthesis of uniform ultrathin metal sulphide nanocrystals. *Nat. Commun.* **2012,** 3, 1177.

[24]. Nakamoto, M.; Yamamoto, M.; Fukusumi, M., Thermolysis of gold(I) thiolate complexes producing novel gold nanoparticles passivated by alkyl groups. *Chem. Comm.* **2002**, 1622.

[25]. Pileni, M. P., The role of soft colloidal templates in controlling the size and shape of inorganic nanocrystals. *Nature Mater.* **2003,** 2, 145.

[26]. Hyeon, T., Chemical synthesis of magnetic nanoparticles. *Chem. Commun.* **2003**, (8), 927.

[27]. Yu, H.; Gibbons, P. C.; Kelton, K. F.; Buhro, W. E., Heterogeneous seeded growth: a potentially general synthesis of monodisperse metallic nanoparticles. *J. Am. Chem. Soc.* **2001,** 123, 9198.

[28]. Whetten, R. L.; Shafigullin, M. N.; Khoury, J. T.; Schaaff, T. G.; Vezmar, I.; Alvarez, M. M.; Wilkinson, A., Crystal structures of molecular gold nanocrystal arrays. *Acc. Chem. Res.* **1999,** 32, 397.

[29]. Korgel, B. A.; Fullam, S.; Connolly, S.; Fitzmaurice, D., Assembly and self-organization of silver nanocrystal superlattices: ordered "soft spheres". *J. Phys. Chem. B* **1998,** 102, 8379.

[30]. Ghezelbash, A.; Sigman, J., M. B.; Korgel, B. A., Solventless synthesis of nickel sulfide nanorods and triangular nanoprisms. *Nano. Lett.* **2004,** 4, 537.

[31]. Larsen, T. H.; Sigman, M.; Ghezelbash, A.; Doty, R. C.; Korgel, B. A., Solventless synthesis of copper sulfide nanorods by thermolysis of a single source thiolate-derived precursor. *J. Am. Chem. Soc.* **2003,** 125, 5638.

[32]. Avazpour, L.; Zandi khajeh, M. A.; Toroghinejad, M. R.; Shokrollahi, H., Synthesis of single-phase cobalt ferrite nanoparticles via a novel EDTA/EG precursor-based route and their magnetic properties. *Journal of Alloys and Compounds* **2015,** 637, 497.

[33]. Baco-Carles, V.; rie; Datas, L.; Tailhades, P., Copper nanoparticles prepared from oxalic precursors. *ISRN Nanotechnology* **2011,** 2011, 7.

[34]. Lewis, E.; Haigh, S.; O'Brien, P., The synthesis of metallic and semiconducting nanoparticles from reactive melts of precursors. *J. Mater. Chem. A* **2013,** 2, 570.

[35]. Park, J.; Lee, W.; Choi, T.; Hwang, S.-H.; Myoung, J. M.; Jung, J.-H.; Kim, S.-H.; Kim, H., Layer-modulated synthesis of uniform tungsten disulfide nanosheet using gas-phase precursors. *Nanoscale* **2015,** 7, 1308.

[36]. Shen, S.; Zhang, Y.; Peng, L.; Xu, B.; Du, Y.; Deng, M.; Xu, H.; Wang, Q., Generalized synthesis of metal sulfide nanocrystals from single-source precursors: size, shape and chemical composition control and their properties. *CrystEngComm* **2011,** 13, 4572.

[37]. Wu, R.; Xu, Y.; Xu, R.; Huang, Y.; Zhang, B., Ultrathin-nanosheet-based 3D hierarchical porous In_2S_3 microspheres: chemical transformation synthesis, characterization, and enhanced photocatalytic and photoelectrochemical property. *Journal of Materials Chemistry A* **2014,** 3, 1930.

[38]. Lewis, E. A.; McNaughter, P. D.; Yin, Z.; Chen, Y.; Brent, J. R.; Saah, S. A.; Raftery, J.; Awudza, J. A. M.; Malik, M. A.; O'Brien, P.; Haigh, S. J., In situ synthesis of PbS nanocrystals in polymer thin films from lead(II) xanthate and dithiocarbamate complexes: evidence for size and morphology control. *Chem. Mater.* **2015,** 27, 2127.

[39]. Mandal, S.; Phadtare, S.; Selvakannan, P. R.; Pasricha, R.; Sastry, M., Fractal gold nanostructures produced by the spontaneous reduction of chloroaurate ions in thermally evaporated hexadecylaniline thin films. *Nanotechnology* **2003,** 14, 878.

[40]. Georgiou, T.; Jalil, R.; Belle, B. D.; Britnell, L.; Gorbachev, R. V.; Morozov, S. V.; Kim, Y. J.; Gholinia, A.; Haigh, S. J.; Makarovsky, O.; Eaves, L.; Ponomarenko, L. A.; Geim, A. K.; Novoselov, K. S.; Mishchenko, A., Vertical field-effect transistor based on graphene–WS_2 heterostructures for flexible and transparent electronics. *Nat. Nanotechnol.* **2013,** 8, 100.

[41]. Ponomarenko, L. A.; Geim, A. K.; Zhukov, A. A.; Jalil, R.; Morozov, S. V.; Novoselov, K. S.; Grigorieva, I. V.; Hill, E. H.; Cheianov, V. V.; Fal'ko, V. I.; Watanabe, K.; Taniguchi, T.; Gorbachev, R. V., Tunable metal-insulator transition in double-layer graphene heterostructures. *Nat. Phys.* **2011,** 7, 958.

[42]. Geim, A. K.; Grigorieva, I. V., Van der Waals heterostructures. *Nature* **2013,** 499, 419.

[43]. Liu, J.; Fu, S.; Yuan, B.; Li, Y.; Deng, Z., Toward a universal "Adhesive Nanosheet" for the assembly of multiple nanoparticles based on a protein-induced reduction/decoration of graphene oxide. *J. Am. Chem. Soc.* **2010,** 132, 7279.

[44]. Muszynski, R.; Seger, B.; Kamat, P. V., Decorating graphene sheets with gold nanoparticles. *J. Phys. Chem. C* **2008,** 112, 5263.

[45]. Koo, H. Y.; Lee, H.-J.; Noh, Y.-Y.; Lee, E.-S.; Kim, Y.-H.; Choi, W. S., Gold nanoparticle-doped graphene nanosheets: sub-nanosized gold clusters nucleate and grow at the nitrogen-induced defects on graphene surfaces. *J. Mater. Chem.* **2012,** 22, 7130.

[46]. Goncalves, G.; Marques, P. A. A. P.; Granadeiro, C. M.; Nogueira, H. I. S.; Singh, M. K.; Grácio, J., Surface modification of graphene nanosheets with gold nanoparticles: the role of oxygen moieties at graphene surface on gold nucleation and growth. *Chem. Mater.* **2009,** 21, 4796.

[47]. Koo, H. Y.; Lee, H.-J.; Go, H.-A.; Lee, Y. B.; Bae, T. S.; Kim, J. K.; Choi, W. S., Graphene-based multifunctional iron oxide nanosheets with tunable properties. *Chem. Euro. J.* **2011,** 17, 1214.

[48]. Lu, G.; Mao, S.; Park, S.; Ruoff, R. S.; Chen, J., Facile, noncovalent decoration of graphene oxide sheets with nanocrystals. *Nano Research* **2009,** 2, 192.

[49]. Yang, X. J.; Wang, Y. H.; Bai, J.; He, X. Y.; Jiang, X. E., Large mesoporous carbons decorated with silver and gold nanoparticles by a self-assembly method: enhanced electrocatalytic activity for H_2O_2 electroreduction and sodium nitrite electrooxidation. *RSC Advances* **2015,** 5, 2956.

[50]. Pan, L.; Zhu, X.-D.; Xie, X.-M.; Liu, Y.-T., Delicate ternary heterostructures achieved by hierarchical co-assembly of Ag and Fe_3O_4 nanoparticles on MoS_2 nanosheets: morphological and compositional synergy in reversible lithium storage. *J. Mater. Chem. A* **2015,** 3, 2726.

[51]. Fang, Y.; Guo, S.; Zhu, C.; Zhai, Y.; Wang, E., Self-assembly of cationic polyelectrolyte-functionalized graphene nanosheets and gold nanoparticles: a two-dimensional heterostructure for hydrogen peroxide sensing. *Langmuir* **2010,** 26, 11277.

[52]. Ren, W.; Fang, Y.; Wang, E., A binary functional substrate for enrichment and ultrasensitive SERS spectroscopic detection of folic acid using graphene oxide/Ag nanoparticle hybrids. *ACS Nano* **2011,** 5, 6425.

[53]. Wang, T.; Liu, J.; Ren, J.; Wang, J.; Wang, E., Mimetic biomembrane-AuNPs-graphene hybrid as matrix for enzyme immobilization and bioelectrocatalysis study. *Talanta* **2015,** 143, 438.

[54]. Wang, L.; Qi, W.; Su, R.; He, Z., Noncovalent functionalization of graphene by CdS nanohybrids for electrochemical applications. *Thin Solid Films* **2014,** 568, 58.

[55]. Smith, C. G., Low-dimensional quantum devices. *Rep. Prog. Phys.* **1996,** 59, 244.

[56]. Kroemer, H., A proposed class of hetero-junction injection lasers. *Proceedings of the IEEE* **1963,** 51, 1782.

[57]. Yang, J.; Lee, J. Y.; Ying, J. Y., Phase transfer and its applications in nanotechnology. *Chem. Soc. Rev.* **2011,** 40, 1672.

[58]. Fendler, J. H., Nanoparticles at air/water interfaces. *Curr. Opin. Coll. Inter. Sci.* **1996,** 1, 202.

[59]. Duan, H. W.; Wang, D. A.; Kurth, D. G.; Mohwald, H., Directing self-assembly of nanoparticles at water/oil interfaces. *Angew. Chem. Int. Ed. Engl.* **2004,** 43, 5639.

Chapter 5

Conclusions

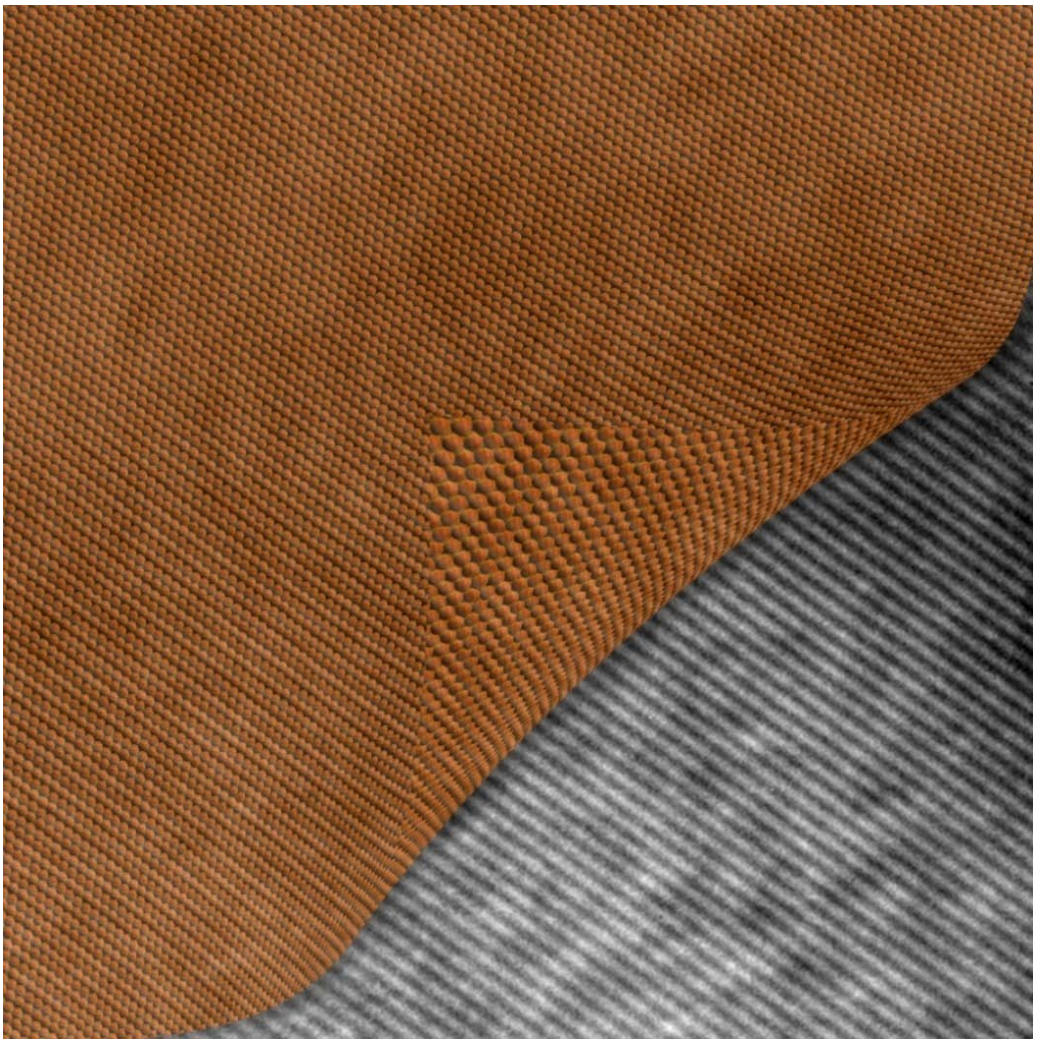

This chapter summarizes the work described in this thesis. Futuristic aspects of this work and possible avenues of applications are also mentioned.

5.1 Summary of the thesis

The work described in this thesis can be summarized as follows.

A class of molecular materials called metal thiolates were the main focus. These metal thiolates were prepared in gram scale quantities via simple solvent less technique. Some of these metal thiolates such as palladium thiolates were found to be readily soluble in certain non-polar organic solvents such as toluene/chloroform. Solution state structural characteristics of these soluble palladium thiolates were evaluated through advanced solution state techniques such as light scattering and X-ray diffraction, electron/force microscopy. It could be concluded that these metal thiolates provide an excellent platform for understanding the exfoliation pathway of two dimensional materials.

The solubility characteristic of these metal thiolates (ex: palladium thiolates/nickel thiolates) was harnessed to prepare metal/metal sulfide nanosheets via thermal treatment of solution state precursors coated onto certain substrates. Some of these metal/metal sulfide nanosheet composites such as nickel/nickel sulfide exhibited exotic room temperature ferromagnetic properties. Similarly, nickel/nickel sulfide composites were found to be good candidates for electrochemical water splitting for hydrogen generation.

Since these metal thiolates constitute both the metal precursor and the stabilizing thiol ligand in them, these were explored for preparing metal and semiconducting nanoparticles. Metal thiolates such as gold thiolates, silver thiolates and palladium thiolates were ground with a reducing agent in a simple single step solid state reaction which yielded metal nanoparticles. Also metal thiolates such as lead thiolates and cadmium thiolates could yield the respective semiconducting metal sulfide nanoparticles upon grinding with an appropriate sulfur source such as sodium sulfide.

Even nanosheet – nanoparticle heterostructures were realized with simple addition of pre-prepared nanoparticle colloidal solutions to the soluble metal thiolates such as palladium octanethiolate that resulted in the decoration of nanoparticles on the metal thiolate nanosheets. Thus the thesis work described here encompasses synthesis of metal

thiolates, solution structural study of soluble palladium thiolates, utilization of these thiolates as precursors to prepare metal/ metal sulfide nanosheets that displayed exotic magnetism and hydrogen evolution and also to prepare metal/metal sulfide nanoparticles and their heterostructures with metal thiolate nanosheets.

5.2 Scope for future work

In literature it has been postulated that completely new and exotic materials could be prepared by making heterostructures from 2D materials. The existence of metal thiolates as 2D materials offers an easy and convenient route to realize such materials. Such composite heterostructures are expected to display unprecedented properties leading to novel applications. Now that these metal thiolates render metal/semiconducting nanosheets and nanoparticles in large quantities with simple coating/grinding methods, these could be explored for any ensuing applications such as in energy generation and catalysis. Also this could be extended to other metals such as bismuth etc. Since some of these metal thiolates are soluble in organic solvents, these should be investigated for their usage in solar cell applications similar to perovskites. One important and quick utilization of the soluble metal thiolates could be in trying to obtain nanosheet- nanosheet heterostructures such as palladium thiolate-nickel thiolate heterostructures. Figure 5.1 below shows the various applications attainable from mixing such 2D layered materials in different possibilities.

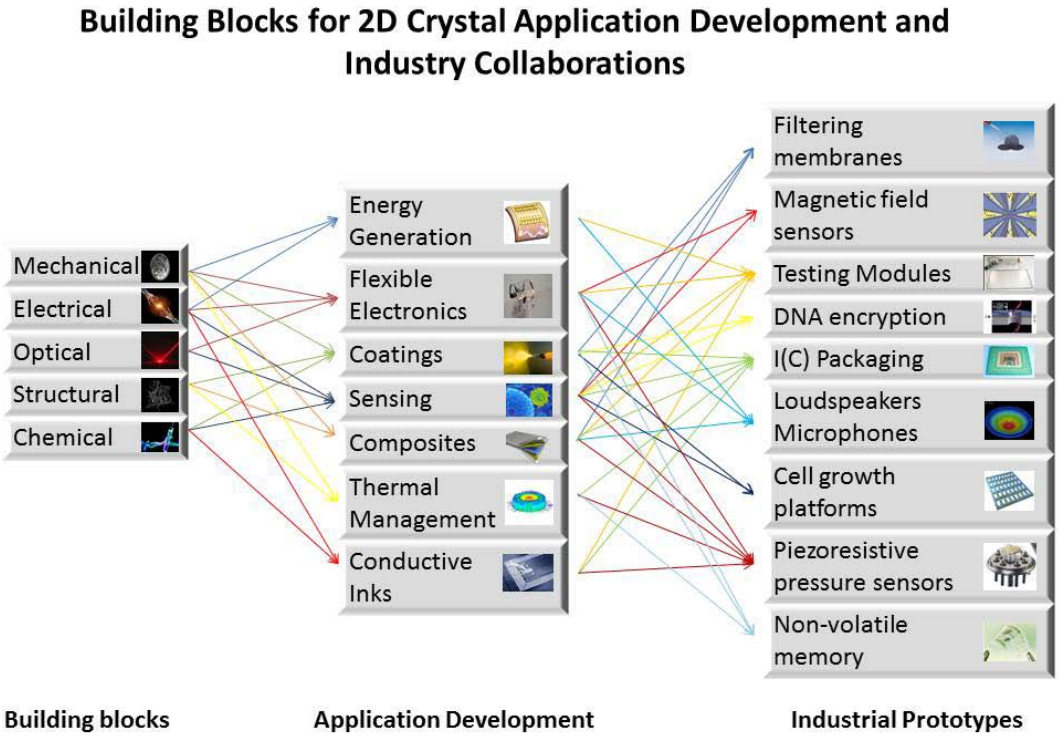

Figure 5.1: *Representative picture showing realizable applications from the various 2D materials through cross-linking these layered two dimensional materials [adapted from: http://graphene.nus.edu.sg/content/old-office-industry-and-innovation].*

In the backdrop of renewed interests in 'Origin of Life' research worldwide which include testing and establishing primary characteristics of life such as self-replication, metabolism, information transfer and evolution through studying different chemical systems and sub-systems such as in self-assembling chemical systems and self-organizing materials, these soluble metal thiolates might be model candidates to test for such self-replication.

APPENDIX-I

(Instruments utilized)

UV-visible absorption spectrophotometry: UV-visible spectroscopic measurements were recorded on JASCO V-570 UV/Vis/NIR spectrophotometer operated at a resolution of 2 nm.

Powder X-ray diffraction: Powder X-ray diffraction was recorded on X'pert Pro model PANalytical diffractometer from Philips PANalytical instruments operated at a voltage of 40 kV and a current of 30 mA with CuK• (1.5418Å) radiation and at different scan rates depending upon the sample.

Solution state Fourier Transform Infrared (FTIR) spectroscopy: Solution state FTIR spectra were recorded on a Bruker Optics ALPHA-E spectrometer operated at a resolution of 4 cm^{-1} with a universal Zn-Se ATR accessory in the 600-4000 cm^{-1} region. The base was thoroughly cleaned with the respective solvent after recording the spectra.

Transmission Electron Microscope/High Resolution Transmission Electron Microscope (TEM/HRTEM): Samples dissolved/dispersed in respective solvents were drop casted onto the 200 mesh carbon coated copper grids (ICON Analytical) and studied employing the Transmission Electron Microscope (TEM) FEI model TECNAI G2 F20 instrument operating at an accelerating voltage of 200 kV. High Resolution Transmission Electron Microscope (HRTEM) FEI model TECNAI G2 F30 instrument operating at an accelerating voltage of 300 kV was employed to clearly visualize the sheet like samples.

Electron Dispersive X-ray Analysis (EDAX): Energy Dispersive X-ray Analysis (EDAX) measurements on the samples were obtained from either a Scanning Electron Microscope (SEM) FEI model Quanta 200 3D equipped with EDAX attachment at an operating voltage of 30 kV or on a HRTEM-FEI model TECNAI G2 F30 instrument operating at an accelerating voltage of 300 kV.

Field Emission Scanning Electron Microscopy (FESEM): Microstructural morphological features of the samples were obtained from a field emission scanning electron microscopy (FE-SEM) with FEI Nova nano SEM 450.

Magnetic Force Microscopy (MFM): The morphological features and magnetic phase shift features of the samples were imaged through contact tapping mode force microscopy from the 'Asylum Research MFP3D Instrument' by employing a magnetic Cr/Co coated tip from Budget Sensors that has a force constant 'k' of 3 N/m and a resonant frequency of 78 KHz with placing the tip at a tip lift height or delta height of 50 nm.

Light Scattering

Dynamic Light Scattering (DLS): Dynamic light scattering measurements were performed on the sample at different concentrations using a 3D-DLS equipment (LS instruments) employing a He-Ne laser (Uniphase) of wavelength 632.8 nm with an inbuilt auto-correlator. Multi angle DLS experimental data were collected at angles 45-60-75-90-105-120 degrees.

Static light scattering: Static light scattering experiments were performed on needed samples and the intensity versus q was plotted in log-linear scale modality.

Wide Angle X-ray Diffraction (WAXD): Wide angle X-ray diffraction (WAXD) experiments on needed samples was done at varying concentrations of the respective sample in solution on an R-axis IV image plate with a Rigaku rotating anode diffractometer having CuK• (• = 1.54 Å) source.

Superconducting Quantum Interference Device (SQUID): Field dependent and temperature dependent magnetization measurements were performed on a Quantum Design MPMS 7T SQUID VSM. Field was set in the 3T to -3T range and room temperature was maintained during the field dependent magnetization measurements. Temperature dependent magnetization values were extracted from 5K to 300K while the applied magnetic field was set at 500 Oe.

Thermogravimetric Analysis (TGA): Samples were subjected to thermogravimetric analysis utilizing a TG50 analyzer (Mettler-Toledo) or a SDT Q600 TG-DTA analyzer under nitrogen atmosphere at 10 °C min^{-1} heating rate within a temperature range of 20–900 °C.

Cyclic Voltammetry (CV): Cyclic voltammetric experiments were performed on the Ni_3S_2-Ni and Ni_3S_2 samples employing Metrohm potentiostat/galvanostat (model Autolab PGSTAT 100) workstation. Glassy carbon commercial disk electrode was utilized as the working electrode to coat the samples under study. Lab constructed Ag/AgCl was employed as the reference electrode and Pt-wire loop was used as the counter electrode. 0.5 µm alumina powder was utilized to polish the working electrode thoroughly prior to usage.

APPENDIX-II

(List of Abbreviations)

2D: Two dimensional

MoS_2: Molybdenum disulfide

$Pd(SR)_2$: Palladium thiolate monomer

PdC_8 thiolate: Palladium octanethiolate

PdC_{10} thiolate: Palladium decanethiolate

PdC_{12} thiolate: Palladium dodecanethiolate

PdC_{16} thiolate: Palladium hexadecanethiolate

PdC_{18} thiolate: Palladium octadecanethiolate

Other metal thiolates follow same (ex: AuC_8 thiolate is gold octanethiolate)

TEM/HRTEM: Transmission Electron Microscope/High resolution transmission Electron Microscope

AFM/MFM: Atomic/Magnetic Force microscope

STM: Scanning Tunneling Microscope

PXRD: Powder X-Ray Diffraction

SQUID: Superconducting Quantum Interference Device

MPMS: Magnetic Property Measurement System

VSM: Vibrating Sample Magnetometer

UV-vis: Ultraviolet-visible

FTIR: Fourier Transform Infrared Spectroscopy

NMR: Nuclear Magnetic Resonance

CCl_4: Carbon tetrachloride

$CHCl_3$: Chloroform

DMF: Dimethyl Formamide

Na_2PdCl_4: Sodium tetrachloropalladate

EDAX: Energy dispersive analysis of X-rays

WAXD: Wide Angle X-ray Diffraction

CuK•: Copper 'K' alpha radiation

HDPE: High Density Polyethylene Film

FWHM: Full Width at Half Maximum

2•: Two Theta

w/v: Weigh per Volume

3D-DLS: Three Dimensional Dynamic Light Scattering

He-Ne laser: Helium-Neon laser

g+, g-: Gauche conformers

t+, t-: Trans conformers

I: Internsity

Wt%: Weight percentage

DMS: Dilute Magnetic Semiconductors

FMS: Ferromagnetic Semiconductors

TGA: Thermogravimetric Analysis

SAED: Selected Area Electron Diffraction

ZFC-FC: Zero Field Cooled-Field Cooled

H_C: Magnetic Coercivity

TBAP: *Tert*-Butyl Ammonium Perchlorate

CV: Cyclic Voltammetry

HER: Hydrogen Evolution reaction

RD electrode: Rotating Disk electrode

RPM: Rotations Per Minute

APPENDIX-III

(Publications)

1) **Busupalli, B.**; Kummara, S.; Kumaraswamy, G.; Prasad, B. L. V., Ultrathin sheets of metal or metal sulfide from molecularly thin sheets of metal thiolates in solution. *Chem. Mater.*, **2014,** 26, 3436.

2) **Busupalli, B.**; Date, K. S.; Datar, S.; Prasad, B. L. V., Preparation of Ni_3S_2 and Ni_3S_2-Ni nanosheets via solution based processes. *Cryst. Growth Des.*, **2015**, 15, 2584.

3) **Busupalli, B.**; Synthetic biological circuits: digital or analog? Curr. Sci., **2015**, 1386, 109(8).

4) **Busupalli, B.**; Devarapalli, R. R.; Battu, S.; Shelke, M. V.; Haram, S. K.; Prasad, B. L. V. Electrochemical structural transformation of nickel sulfide nanosheets and their electrocatalytic hydrogen generation properties. ***To be communicated***.

5) **Busupalli, B.** and Prasad, B. L. V., Patent filed-Solution process for the synthesis of single layer metal nanosheets, (Ref. No. 0024NF2014: 0612DEL2014) **PCT** final filing date 5th March **2015 (patent)**.